UTS UNIVERSITY OF TECHNOLOGY SYDNEY

Advanced Multi-band and Ultrawideband Antenna Arrays

by Yi He

Thesis submitted in fulfilment of the requirements for the degree of

Doctor of Philosophy

under the supervision of Prof Jay Guo

University of Technology Sydney
Faculty of Engineering and Information Technology

June 2025

CERTIFICATE OF ORIGINAL AUTHORSHIP

I, Yi He, declare that this thesis is submitted in fulfilment of the requirements for the award of Doctor of Philosophy, in the Faculty of Engineering and Information Technology at the University of Technology Sydney.

This thesis is wholly my own work unless otherwise referenced or acknowledged. In addition, I certify that all information sources and literature used are indicated in the thesis.

I certify that the work in this thesis has not previously been submitted for a degree nor has it been submitted as part of the requirements for a degree at any other academic institution except as fully acknowledged within the text.

This research is supported by the Australian Government Research Training Program.

Signature: Production Note:
Signature removed prior to publication.

Date: 9 June 2025

ABSTRACT

The exponential growth of information exchange necessitates communication systems to cover broader frequency coverage for higher data capacity, deliver ultra-high-speed connections, and ensure uninterrupted, reliable service. To address these challenges, antenna arrays in wireless communication systems must be advanced to support broad frequency coverage while maintaining stable radiation performance. This thesis systematically explores key innovations in multi-band/ultrawideband (UWB) antenna arrays, presenting three major works.

In **Work 1**, a smaller antenna operating in the high band (HB) within 1.36–2.72 GHz is embedded within the cavity of a larger antenna working in the low band (LB) within 0.8–0.96 GHz, employing an "embedded scheme" to achieve a compact size and multi-band operation. Innovative techniques make the LB antenna electromagnetically transparent at the HB, effectively suppressing cross-band interference. Consequently, both antennas operate independently while sharing a single compact aperture.

In **Work 2**, a new compact buffering scheme is proposed, incorporating a specialized "buffering layer" between the LB and HB antennas. The buffering layer reduced the height of the larger LB antenna from $0.20\lambda_L$ to $0.087\lambda_L$ (λ_L is the wavelength at the lowest LB frequency) without compromising its performance. It also enhances the bandwidth of the HB antenna from 45.5% to 60.2%. The unwanted interference between the two-band antennas remains minimal, as the buffering layer traps energy within itself, preventing it from entering the port of the other antenna when one is excited. This

design supports two broad frequency bands of 0.69–0.96 GHz in the LB and 1.47–2.7 GHz in the HB, with an impressively low profile of $0.087\lambda_L$.

In contrast to the previous works aimed at minimizing coupling between antennas, **Work 3** leverages mutual coupling to enable UWB operation, resulting in a frequency-reconfigurable tightly coupled dipole array (FR-TCDA). This work addresses critical challenges faced by other TCDAs: significant efficiency reduction when attempting to achieve over a decade of bandwidth and wide-angle beam scanning. A combined bandwidth of 15.8:1 (0.37–5.85 GHz) is achieved through two frequency-reconfigurable states, delivering high radiation efficiency exceeding 95% and wide beam-scan angles of up to $\pm 70^\circ$.

Together, these contributions deliver compact, interference-resilient antenna arrays with broad multi-band/UWB coverage, extended beam scanning, and high radiation efficiency, advancing the vision of ubiquitous 6G networks to bridge the digital divide and bolster global communication infrastructure.

ACKNOWLEDGEMENT

I am thankful for the opportunity to conduct my research at Global Big Data Technologies Centre **GBDTC**; the environment here has been both motivating and enriching.

Firstly, I would like to express my sincere gratitude to my supervisor, **Prof. Yingjie Jay Guo**, for his invaluable support throughout my Ph.D. journey. Prof. Guo provided not only an excellent research environment but also profound advice and innovative ideas that shaped the direction of my research project. His extensive expertise in antennas and wireless communications has been a constant source of inspiration, encouraging me to push the boundaries of my understanding and explore novel solutions.

I sincerely thank my co-supervisor, **Assoc. Prof. Can Ding**, for his pivotal role in conceptualizing and supervising my multi-band antenna design. His keen insight into academic frontiers and rigorous academic approach have given me constructive suggestions and sharpened my research skills. His diligence serves as a model for my both research and personal growth.

I am also deeply indebted to **Prof. Richard W. Ziolkowski** at the University of Arizona for his insightful suggestions on ultra-wideband antenna design, along with his constructive feedback on my research writing. He offered profound advice and innovative ideas for my project, and his higher-level perspective has significantly enriched my work. He is a warm and admirable mentor.

I am grateful to my partner, **Dr. Gengming Wei**, whose thought-provoking discussions often inspired me to delve deeper into theoretical analyses. His profound expertise

in antenna measurements provided indispensable support for both the experimental setup and the data analysis aspects of my research. He is someone I deeply admire and wish to learn from.

I would also like to extend my thanks to **Prof. Peiyuan Qin** and **Dr. Shulin Chen** for their valuable feedback and suggestions during my Ph.D. candidature assessments.

To the incredible members of **GBDTC**, including **Dr. Haihan Sun, Dr. He Zhu, Dr. Lizhao Song, Dr. Yubo Wen, Dr. Ming Li, Dr. Yuenian Chen, David Thomas, Shangyi Sun, Fanchao Zeng, Xingyu Cheng, Yang Xu, Zhaoqi Cui, Feng Tao, Chao Wang, Jingping Wang, Leyuan Liang, Yingli Liu, Yunze Diao, Shan Huang, Maria Pubill Font, Doruk Baran,** and **Mina Feizi**, thank you for the camaraderie and unwavering support that have made this journey so rewarding. I am truly fortunate to be part of such a smart and supportive group.

I am profoundly grateful to my parents for their unfailing support,Äîboth in my education and in life. They have always been my bedrock of strength, offering me a loving growing environment. Their unwavering encouragement enabled me to focus wholeheartedly on my personal development.

Finally, I thank myself for persistently striving for growth, both in my abilities and spirit. I am grateful for every experience that has shaped me along this journey.

Thank you all for your unwavering support and belief in this work. Without you, this thesis would not have been possible.

List of Publications

Peer-reviewed Journal Articles :

1. **Yi He**, Can Ding, Chengxiang Chang, Gengming Wei and Y. Jay Guo, "A Bowl-Shaped Filtering Antenna With Wideband Cross-Band Scattering Mitigation for Dual-Band Base Stations," *IEEE Transactions on Antennas and Propagation*, vol. 72, no. 8, pp. 6723-6728, August 2024.

2. **Yi He**, Gengming Wei, Richard W. Ziolkowski and Y. Jay Guo, "An Ultrawideband Frequency-Reconfigurable Tightly Coupled Dipole Array With Wide Beam-Scanning Capability," *IEEE Transactions on Antennas and Propagation*, vol. 72, no. 11, pp. 8488-8500, November 2024.

3. **Yi He**, Shaodong Wang, Gengming Wei, Can Ding and Y. Jay Guo, "Low Profile Base Station," *IEEE Transactions on Antennas and Propagation*, vol. 73, no. 6, pp. 3492-3502, June 2025.

4. Gengming Wei, Yilei Wang, **Yi He**, Richard W. Ziolkowski and Y. Jay Guo, "Ultra-Wideband Vertically Polarized Long-Slot Circular Phased Array," *IEEE Transactions on Antennas and Propagation*, vol. 72, no. 5, pp. 4161-4172, May 2024.

Peer-reviewed Conference Articles :

5. **Yi He**, Can Ding, Gengming Wei and Y. Jay Guo, "An Embedded Dual-Band Base Station Antenna Array Employing Choked Bowl-Shaped Antenna for Cross-

Band Scattering Mitigation," *2022 16th European Conference on Antennas and Propagation (EuCAP)*, Madrid, Spain, 2022.

6. **Yi He**, Can Ding, Gengming Wei and Y. Jay Guo, "A Bowl-Shaped Base Station Antenna with Wideband Cross-Band De-Scattering Capability," *2024 IEEE International Symposium on Antennas and Propagation and INC/USNC-URSI Radio Science Meeting (AP-S/INC-USNC-URSI)*, Firenze, Italy, 2024.

7. **Yi He**, Can Ding, Gengming Wei and Y. Jay Guo, "An Embedded Scheme-Based Dual-band Shared Aperture Base Station Antenna Array," *2024 IEEE International Symposium On Antennas And Propagation (ISAP)*, Incheon, 2024, Korea.

8. **Yi He**, Gengming Wei, Richard W. Ziolkowski and Y. Jay Guo, " Frequency-Reconfigurable Ultrawideband Phased Array with Enhanced Beam-scanning Performance," *6th Australian Microwave Symposium*, Gold Coast, Australia, 2025.

9. **Yi He**, Gengming Wei, Can Ding and Y. Jay Guo, "A New Aperture-Sharing Method for Dual-Band Antenna Arrays," *2025 IEEE International Symposium on Antennas and Propagation and INC/USNC-URSI Radio Science Meeting (AP-S/INC-USNC-URSI)*, Ottawa, Canada, 2025.

10. Gengming Wei, **Yi He**, Richard W. Ziolkowski and Y. Jay Guo, "Ultra-Wideband Vertically Polarized Circular Array for Passive Sensing Applications," *2025 19th European Conference on Antennas and Propagation (EuCAP)*, Stockholm, Sweden, 2025.

11. Gengming Wei, **Yi He**, Richard W. Ziolkowski and Y. Jay Guo, "Ultra-Wideband (UWB) Frequency-Reconfigurable Phased Array," *2025 IEEE International Symposium on Antennas and Propagation and INC/USNC-URSI Radio Science Meeting (AP-S/INC-USNC-URSI)*, Ottawa, Canada, 2025.

Table of Contents

List of Figures

Figure **Page**

List of Tables

ABBREVIATIONS

BSA – base station antenna

CLL – capacitively loaded loop

CSA – current sheet array

DLDS-CLLs – dual-level, double-sided capacitively loaded loops

eMBB – enhanced mobile broadband

FR-TCDA – frequency-reconfigurable tightly-coupled dipole array

FOPEN – foliage penetration

FSS – frequency-selective surface

GLONASS – Global Navigation Satellite System

GPS – Global Positioning System

HB – high band

HPBW – half-power beamwidth

IoT – Internet of Things

LB – low band

LC – inductor-capacitor

MIMO – multiple-input and multiple-output

mMTC – massive machine-type communication

PMI – polymethacrylimide

PRSs – partially reflecting surfaces

S-parameters – scattering parameters

SRR – split-ring resonator

TCBL – tightly coupled buffering layer

TCDA – tightly coupled dipole array

UEAEP – unit-excitation active element pattern

UWB – ultra-wideband

URLLC – ultra-reliable low-latency communication

WAIM – wide-angle impedance matching

LIST OF SYMBOLS

λ_0 - free-space wavelength at a chosen reference frequency

λ_L - free-space wavelength at the lowest operating frequency of the LB band

λ_{L_0} - free-space wavelength at the center frequency of the LB band

λ_H - free-space wavelength at the highest operating frequency of interest

k - free-space wavenumber, $k = \frac{2\pi}{\lambda}$

d_x, d_y - array element spacing along the x- and y-directions

M, N - total number of array elements along the x- and y-axes, respectively

S_{ij} - scattering (S-)parameter from port i to port j

$S_{mn,pq}$ - scattering (S-)parameter between the (m,n)-th port and the (p,q)-th port in an array

$\Gamma_{mn}(\theta_0, \phi_0)$ - reflection coefficient of the (m,n)-th array element when scanned at angles θ_0, ϕ_0

ε_r - relative permittivity of a dielectric material

$\tan\delta$ - loss tangent of a dielectric material

Ω - unit of impedance (ohms)

θ, ϕ - spherical coordinate angles used for defining beam or pattern directions

CHAPTER 1

INTRODUCTION

Over the past decade, wireless communication networks have transformed dramatically, driven by escalating demands for higher data rates, broader spectral resources, and more efficient architectures. As the industry progresses beyond current 5G standards, emerging applications-ranging from holographic communications to large-scale, low-latency Internet of Things (IoT) deployments-place unprecedented constraints on network performance. These evolving requirements highlight the need to fundamentally re-envision the building blocks of future wireless infrastructure, especially antenna arrays. By pushing the boundaries of bandwidth utilization, interference mitigation, beam-steering capability, and manufacturing scalability, advanced antenna designs are poised to shape the communication paradigms of 6G and beyond.

1.1 Challenges for Future Wireless Communication Systems

The surge in data traffic, fueled by data-intensive applications such as virtual and augmented reality, holographic displays, and massive IoT ecosystems, necessitates profound enhancements to wireless networks. This intensifying landscape demands not only higher data throughput and improved spectral efficiency but also robustness against interference, flexible beam control, enhanced reliability, and sustainable energy usage. Antenna arrays play a pivotal role in meeting these needs, yet their design and implementation face a host of interrelated challenges.

1.1.1 Increasing Bandwidth Requirements

To achieve ultra-high-speed data links, future systems must operate across significantly wider frequency bands. Realizing ultra-wideband (UWB) performance, however, poses substantial difficulties in ensuring stable impedance matching, consistent radiation patterns, and reliable gain across broad spectral spans. Furthermore, practical concerns-such as cost, complexity, and the seamless integration of multi-band functionalities-add to the complexity of meeting these bandwidth expansion targets.

1.1.2 Cross-Band Interference in Multi-Band Systems

Incorporating multiple frequency bands within a single antenna aperture introduces the risk of cross-band interference. Antennas operating in adjacent bands can mutually degrade radiation performance, efficiency, and overall signal quality. Addressing such interference is crucial for modern base station antenna arrays, which must ensure stable operation, robust isolation, and minimal inter-element coupling to support the increasingly diverse wireless environment.

1.1.3 Beam-Scanning and Spatial Coverage Limitations

Next-generation communication scenarios mandate flexible and dynamic radiation coverage, including wide-angle beam-scanning capabilities. This requirement arises in applications like autonomous transportation, intelligent urban infrastructures, and satellite constellations. Achieving broad scanning ranges, high radiation efficiency, and low-profile arrays remains challenging, necessitating innovative design methodologies and materials to balance performance, complexity, and cost.

1.1.4 Integration of Advanced Materials and Fabrication Techniques

Novel materials-such as metamaterials and frequency-selective surfaces-and advanced fabrication techniques like 3D printing offer promising routes to improved antenna performance. However, scaling these approaches from prototypes to reliable, repeatable, and cost-effective mass production is nontrivial. Ensuring compatibility with existing manufacturing processes while maintaining uniformity, mechanical robustness, and performance consistency is critical for widespread adoption.

1.1.5 Power Efficiency and Sustainability

As global data consumption accelerates, so does the need for energy-efficient network solutions. Antenna arrays must be designed to minimize losses, enhance gain, and operate efficiently over extended bandwidths and multiple bands, all while reducing their environmental footprint. Emphasizing sustainable materials and energy-saving technologies is thus pivotal for future wireless systems, reflecting industry-wide commitments to environmental responsibility.

1.1.6 Alignment with Emerging Standards and Technologies

Forthcoming wireless standards emphasize metrics such as ultra-reliable low-latency communication (URLLC), massive machine-type communication (mMTC), and enhanced mobile broadband (eMBB). Antenna arrays must align with these evolving requirements, supporting advanced waveforms, adaptive resource allocation, and dense network topologies. Ensuring that antenna designs remain forward-compatible, adaptable, and scalable is essential for their long-term viability.

1.1.7 Compactness and Cost Constraints

The rollout of extensive infrastructure across diverse geographical areas demands antenna arrays that are compact, low-profile, and cost-effective. Achieving these attributes without sacrificing performance is challenging, as it often involves balancing trade-offs between complexity, efficiency, production costs, and scalability.

In summary, these challenges underscore the need for innovative antenna arrays capable of providing broad bandwidths, mitigating interference, offering agile beam-scanning, ensuring compatibility with advanced standards, and adhering to size and cost constraints. Addressing these intertwined issues is essential for enabling the next generation of wireless communication systems.

1.2 Motivation and Contributions

The persistent drive toward more sophisticated wireless technologies provides the underlying motivation for this work. As networks evolve to support increasingly complex and bandwidth-intensive applications, there is a clear imperative to develop antenna solutions that can efficiently integrate multiple bands, suppress interference, extend bandwidth, and adapt radiation patterns dynamically.

This thesis delivers several key contributions to these objectives:

- **Addressing cross-band interference challenges based on existing multi-band antenna array scheme:** This study focuses on mitigating strong cross-band scattering interference in embedded-scheme-based multi-band antenna arrays. An innovative filtered bowl-shaped low-band (LB) antenna is proposed, integrating innovative helical filters for wideband interference suppression, specialized baluns for improved impedance matching and radiating gain, and customized 3D-printed supports for structural stability. The resulting design achieves a remarkable cross-band interference suppression bandwidth while maintaining a compact aperture size that enables enhanced in-band isolation.

- **Achieving immunity to cross-band interference based on a new multi-band antenna array scheme:** This work proposed a new shared-aperture multi-band antenna array scheme, named "buffering scheme", to overcome unwanted cross-band interferences while ensuring optimal wideband dual-band performance. Unlike existing works that rely on complex filtering/Frequency selective surface (FSS) structures, this work incorporates a unique buffer layer to enhance overall performance, enabling naturally suppressed cross-band interference, an exceptionally low profile, and enhanced bandwidth.

- **Advancing ultra-wideband antenna array beyond cross-band interference limitations:** UWB antenna arrays inherently avoid cross-band interferences in multi-band antenna arrays by covering continuous frequency ranges. This work addresses problems specifically associated with UWB tightly-coupled dipole arrays (TCDAs), i.e., how to avoid a significant reduction of efficiency when attempting to achieve more than a decade of bandwidth and wide-angle spatial beam scanning. Enhanced performance is achieved with a custom-designed reconfigurable layer and an innovative wide-angle impedance matching (WAIM) structure.

All antenna array prototypes were fabricated and measured, with experimental results confirming the predicted enhanced performance. Through simulation and experimental validation, these contributions establish comprehensive antenna array solutions for reliable, high-performance communication systems to meet the demands of 6G and beyond.

1.3 Thesis Outline

This thesis is organized into six chapters, each building upon the last to present a cohesive framework for designing advanced multi-band and UWB antenna arrays.

- **Chapter 1: Introduction** Outlines key challenges, motivations, and contributions, setting the stage for the research presented in subsequent chapters.
- **Chapter 2: Literature Review and Research Challenges** Surveys the state-of-the-art in multi-band and UWB antenna arrays, identifies existing limitations, and defines the research gaps addressed in this work.
- **Chapter 3: Multi-Band Shared-Aperture Antenna Array Based on Embedded Scheme** Introduces a novel filtered LB antenna design for multi-band arrays, featuring helical filters and custom supports that enhance interference suppression and impedance matching.
- **Chapter 4: Multi-Band Shared-Aperture Antenna Array Based on a New Buffering Scheme** Presents the TCBL approach to mitigate cross-band interference in multi-band shared-aperture arrays, achieving a compact, cost-effective solution with robust dual-band performance.

- **Chapter 5: UWB Tightly Coupled Dipole Array (TCDA)** Proposes a frequency-reconfigurable UWB TCDA with a reconfigurable layer and WAIM structure, expanding bandwidth and beam-scanning capabilities.
- **Chapter 6: Conclusion and Future Work** Summarizes the major findings, discusses their implications for future wireless networks, and outlines potential avenues for further investigation.

CHAPTER 2

LITERATURE REVIEW AND CHALLENGES

2.1 Introduction

The transition to next-generation wireless communication demands higher data rates, lower latency, and more robust connectivity. Driven by an array of emerging applications-ranging from autonomous vehicles and telemedicine to virtual/augmented reality and massive IoT-these stringent requirements call for innovative antenna array solutions supporting multi-band or UWB operations.

Multi-band antenna arrays integrate multiple frequency bands within a single platform, ensuring compatibility with various communication standards (e.g., 3G/4G/5G/6G, GPS/GLONASS/Galileo, IoT), while offering enhanced spectrum efficiency and hardware consolidation. One prominent approach is the shared-aperture antenna array design, which enables simultaneous operation across multiple bands within a compact deployment, making it particularly advantageous in space- or cost-sensitive scenarios. However, cross-band scattering/coupling interference, and the need for stable performance over wide frequency ranges pose significant engineering challenges, driving ongoing research

into novel design strategies.

In parallel, UWB phased array antennas provide continuous UWB frequency coverage, supporting diverse applications such as high data-rate wireless links, precision sensing, and high-resolution imaging. Their broad bandwidth and beamforming capabilities facilitate precise data acquisition and agile scanning, benefiting emerging fields such as autonomous systems, environmental monitoring, and advanced sensing. Yet, implementing robust UWB arrays requires addressing obstacles like effective UWB impedance matching, extended beam scanning range, minimizing efficiency losses, and feeding-network integration. Recent innovations in array architectures, feeding schemes, and materials seek to overcome these hurdles, expanding the scope of UWB technologies in civilian applications.

Despite the shared goal of accommodating wide or multiple frequency bands, multi-band and UWB antenna arrays both present distinct technical and implementation issues. Understanding these parallel yet interconnected challenges is vital for advancing next-generation wireless systems. This chapter provides a comprehensive review of the design considerations, recent progress, and representative applications for both multi-band and UWB antenna arrays. It also highlights key research challenges and future directions to offer a well-rounded perspective on these critical technologies.

Chapter Organization:

- Section 2.2 explores the design principles of multi-band antenna arrays, covering various array schemes and techniques to mitigate cross-band interference. Representative implementations are also reviewed to highlight their advantages and challenges.

- Section 2.3 presents an in-depth analysis of UWB antenna arrays, discussing key design considerations such as impedance matching, beam scanning range, and

feeding network integration. State-of-the-art developments and practical implementations are examined.

- Section 2.4 identifies the key research challenges in both multi-band and UWB antenna arrays. This section also discusses potential unified solutions that could bridge the gap between these two types of arrays.

2.2 Multi-band antenna arrays

2.2.1 Considerations for Designing Multi-band antenna arrays

As discussed in Section 2.1, multi-band antenna arrays enable simultaneous support for diverse communication standards within a single aperture, offering benefits such as efficient space usage and hardware consolidation. While these advantages underscore their rising importance in modern applications, designing high-performance multi-band arrays requires meticulous attention to several key aspects. Key considerations include:

1. Wideband Stable Radiation Performance

Ensuring consistent performance across multiple frequency ranges involves achieving effective impedance matching, maintaining stable radiation patterns and realized gain for each band. These factors collectively ensure uniform signal quality and reliable communication across all operating bands, making it essential to optimize the antenna design for wideband operation.

2. Suppressed Cross-Band Interference

Maintaining independent operation across different frequency bands requires minimizing cross-band scattering and coupling interference. Effective mitigation techniques or innovative placement strategies to isolate multi-band antennas, ensuring independent operation across frequency bands. These measures are essential to preserving radiation pattern integrity, port-to-port isolation, and overall system performance.

3. Compactness and Structural Integration

Shared-aperture configurations enable multi-band operation within a compact form. Achieving this requires the careful integration of multiple antennas into a single structure, optimizing size, weight, and material properties. Additionally, the structural design must support robust mechanical and electromagnetic performance, ensuring that bandwidth, gain, and radiation stability are preserved across all frequency bands while meeting space constraints.

4. Manufacturability, Scalability, and Flexible Deployment

Practical implementation depends on scalable, cost-effective designs capable of adapting to diverse installation environments. Flexible deployment options, including adaptability to various installation scenarios and environments, enhance the versatility and applicability of the antenna system in real-world applications.

2.2.2 Realization Forms of Multi-band antenna arrays

Various approaches based on several typical array schemes have been proposed to tackle these issues, each presenting unique trade-offs among the proposed considerations. This discussion emphasizes dual-band array schemes, as they are foundational examples for multi-band array designs and provide practical, well-established design principles. Typical array schemes include interleaved, embedded, stacked, and back cavity schemes. These designs aim to optimize spatial efficiency, minimize cross-band interference, and maintain independent operation for antennas working in different frequency bands. This section will detail the implementation strategies and the distinctive design principles associated with each scheme.

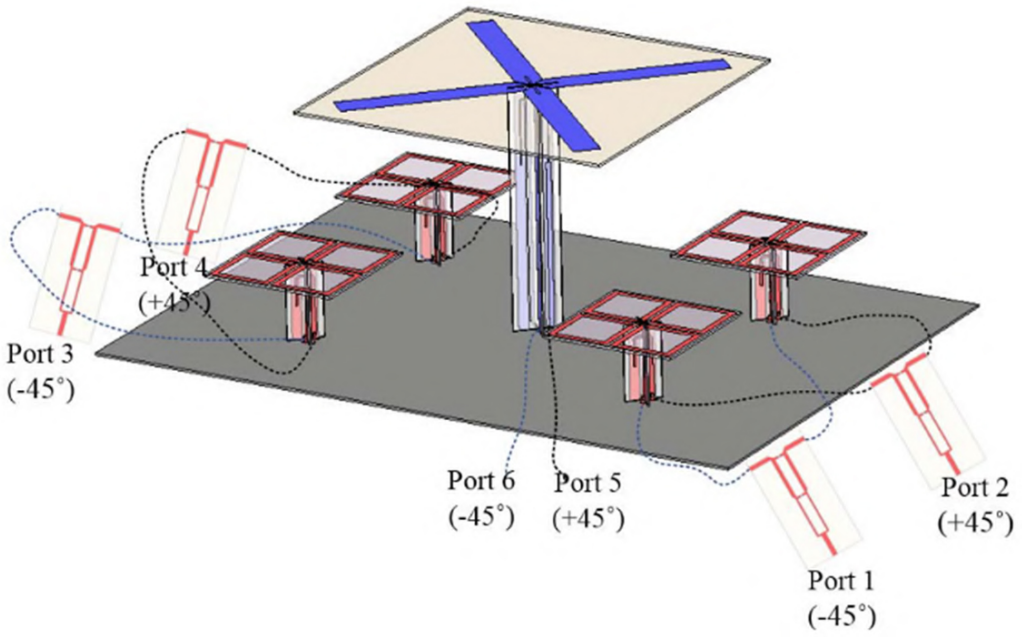

Figure 2.1: Configuration of the interleaved-scheme-based dual-band array [1].

2.2.2.1 Interleaved Scheme

The interleaved scheme, illustrated in Figure 2.1, is a widely adopted array configuration for dual-band shared-aperture antenna arrays. In this arrangement, LB and HB antennas share a common ground plane, with HB antennas positioned in the shadows of the larger-sized LB antennas. In this case, the LB antennas block the HB radiation and cause a strong scattering impact on the HB antennas, resulting in deteriorated HB radiation performance [2]. This issue is illustrated in Figure 2.2, where the presence of LB antennas noticeably distorts the HB radiation pattern. To overcome these unwanted scattering effects, various filtering techniques have been applied to LB antennas, making them “electromagnetically invisible” at HB frequencies. Most of these filtering techniques are developed specifically for the interleaved scheme and are detailed as follows.

Inserting chokes into LB antennas has proven to be an effective method for mitigating cross-band scattering issues [1, 3–6]. Figure 2.3 illustrates a choked LB antenna arranged in the interleaved dual-band array scheme. Acting as low-pass high-stop filters, chokes

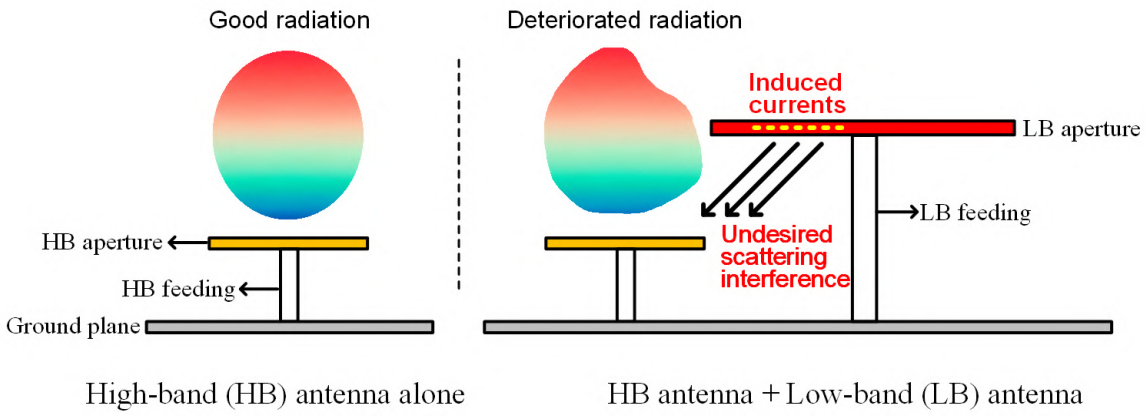

Figure 2.2: Illustration of cross-band scattering from the LB antennas on adjacent HB antennas.

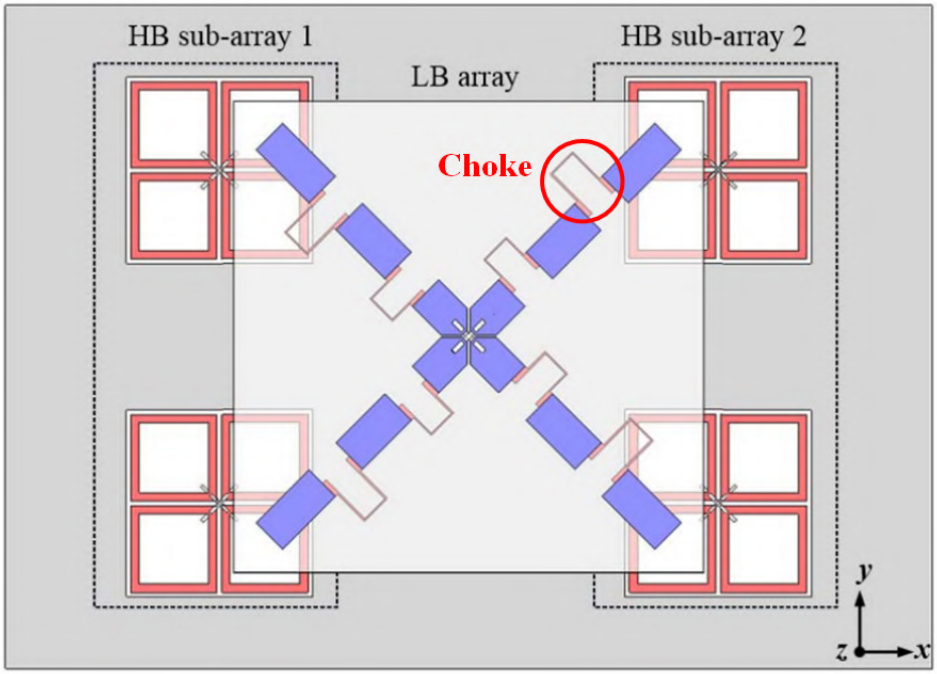

Figure 2.3: Top view of the choked LB antenna arranged in the interleaved dual-band array [1].

suppress unwanted HB currents on LB arms while maintaining LB performance. They segment LB arms into shorter sections with lengths well below half the wavelength of the highest HB frequency. At HB frequencies, chokes function as open circuits with high impedance and effectively suppress induced currents on the LB arms. On the other hand, at LB frequencies, chokes behave as short circuits and connect the segmented LB arms, ensuring unaffected LB operation [1].

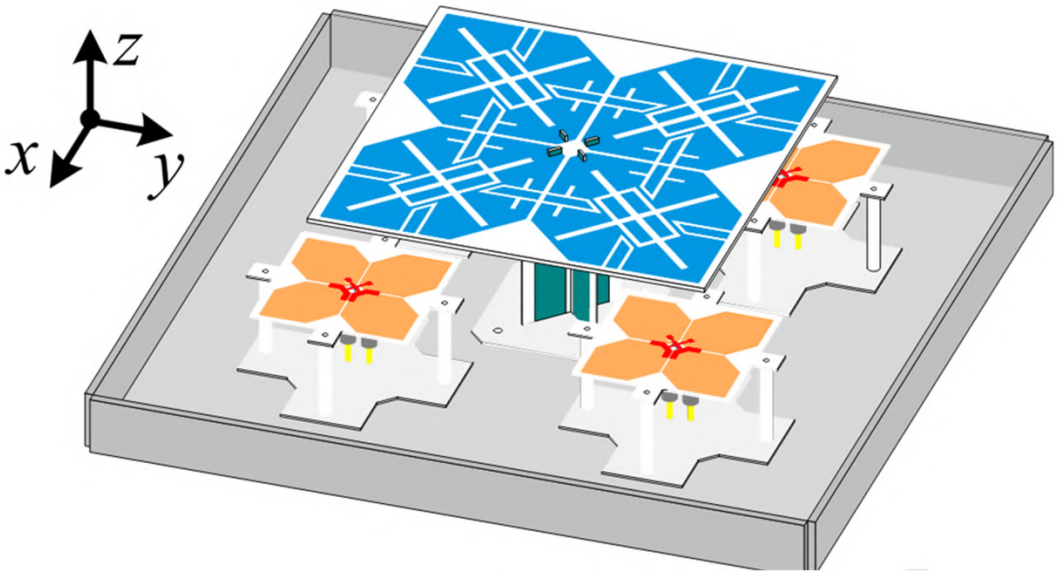

Figure 2.4: Etched-slots LB antenna arranged in the interleaved dual-band array [7].

Etching slots into LB radiators introduces high-impedance regions, effectively disrupting HB current paths and neutralizing re-radiation [6–9]. This approach is exemplified in Figure 2.4, showing an etched-slots LB antenna in an interleaved-scheme-based array. Similarly, U-/L-shaped structures achieve suppression by redirecting HB-induced currents through phase-opposed interactions that effectively cancel the detrimental impact from the induced currents [10–12]. These techniques collectively enhance the electromagnetic transparency of LB antennas, ensuring minimal interference with HB radiation and improving overall dual-band array performance.

The 2.5-D cloak offers an innovative approach to suppressing cross-band scattering.

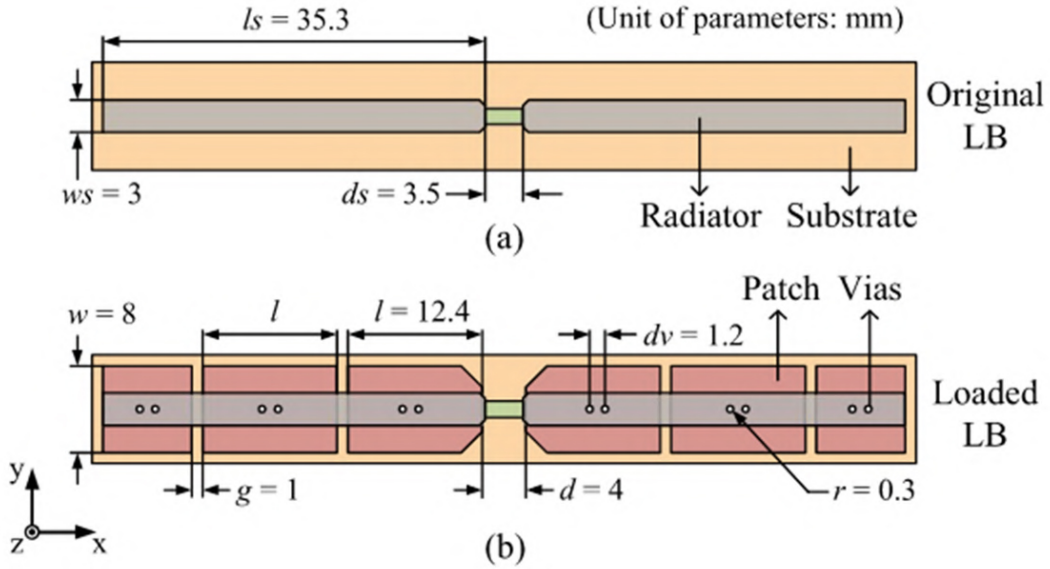

Figure 2.5: Top view of the LB dipole arm. (a) Original structure. (b) After adding the 2.5-D cloak achieved through patches and vias [13].

By introducing patches and vias into LB dipole radiators, the design generates reversed HB currents that cancel each other [13]. Figure 2.5 illustrates the top view of the LB dipole arm before and after adding the 2.5-D cloak. This method achieves simultaneous suppression of cross-band scattering, cross-band coupling, and in-band coupling while maintaining simplicity and reducing system weight [13]. Compared to techniques like etched slots and chokes, the 2.5-D cloak provides broad-spectrum suppression with a lightweight and compact structure.

Absorbing metasurfaces with bandstop characteristics in the HB provide another versatile solution for cross-band coupling interference suppression. These metasurfaces incorporate resistive square loop unit cells or transparent materials like Indium Tin Oxide to absorb HB signals while maintaining LB performance [14, 15]. For instance, designs incorporating resistive elements achieve cross-band isolation levels exceeding 28 dB [14], while transparent metasurfaces demonstrate even higher cross-band isolation, up to 30 dB [15]. Figure 2.6 illustrates the structure of the metasurface loaded with

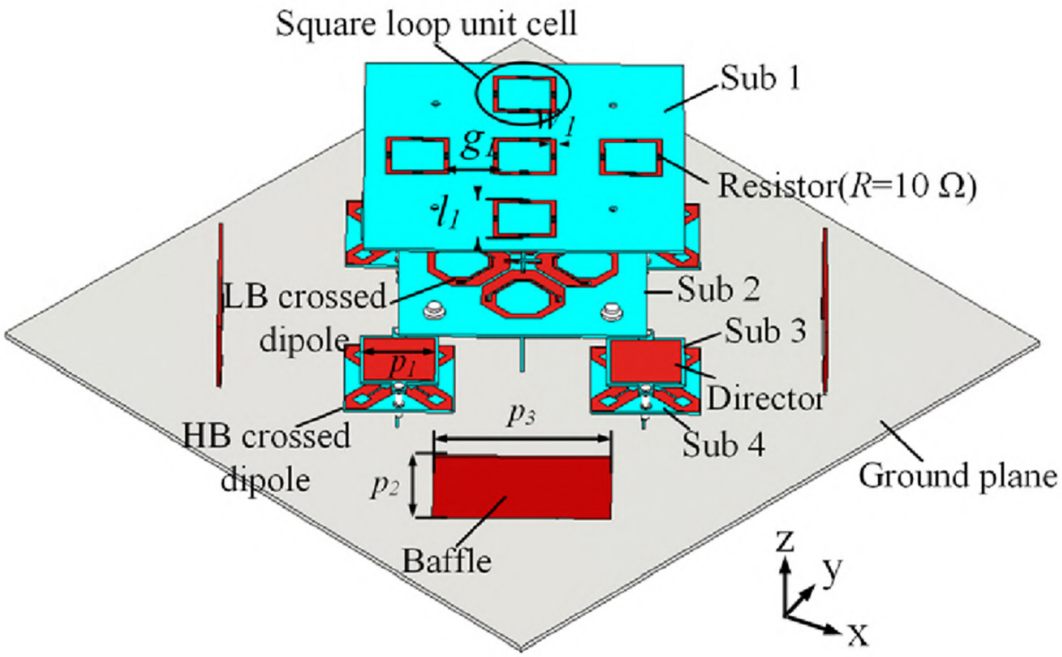

Figure 2.6: Metasurface loading resistive square loop unit cells placed above the interleaved dual-band array [14].

resistive square loop unit cells, showing its implementation in the dual-band array.

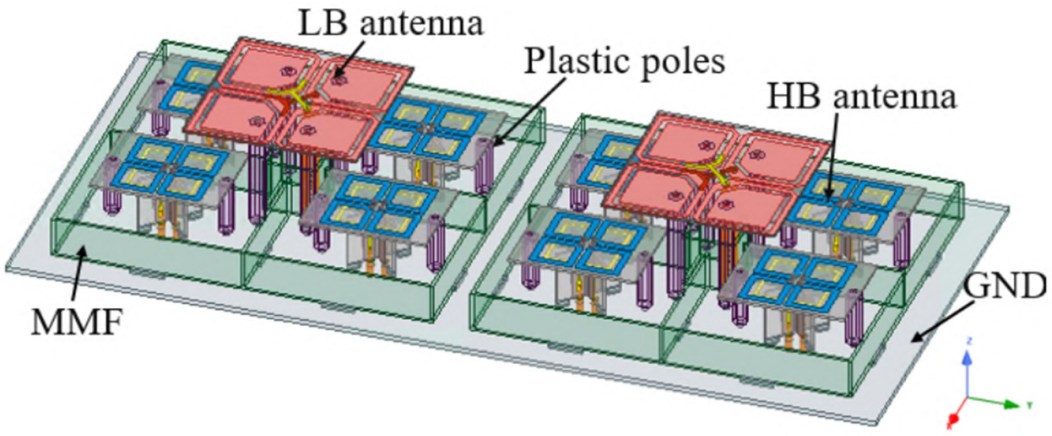

Figure 2.7: Bandpass-FSS-based transparent LB antenna in the interleaved dual-band array [16].

Filter-based solutions employing FSSs [16, 17], split-ring resonators (SRRs) [18], or metasurfaces [19] introduce precise filtering characteristics to mitigate cross-band

interference. FSS-integrated LB antennas use electromagnetic transparent LB antennas employing bandpass FSSs to ensure seamless HB radiation while maintaining LB operation [16, 17]. Figure 2.7 depicts a bandpass-FSS-based transparent LB antenna within an interleaved dual-band array in [16]. SRRs within LB elements suppress HB scattering by establishing resonant conditions that minimize re-radiation [18]. Drude metasurfaces extend this concept further, offering high-efficiency radiation and customizable transparency for LB and HB frequencies [19].

In summary, these cross-band scattering mitigation strategies highlight the innovation and versatility in addressing multi-band antenna interference through filtering or electromagnetic transparency mechanisms. Each technique presents unique trade-offs in bandwidth, isolation performance, structural complexity, and system weight, catering to the diverse operational requirements of modern communication systems. While approaches based on interleaved schemes effectively reduce cross-band interference and provide distinct advantages, they often require careful re-optimization to prevent performance trade-offs in the LB bandwidth and can introduce extra design complexity. Consequently, these solutions must be meticulously tailored to accommodate the diverse operational requirements of modern communication systems.

2.2.2.2 Embedded Scheme

A typical embedded array can be seen in Figure 2.8 [20]. The embedded scheme is also a widely adopted configuration in the industry for dual-band antenna arrays. In this setup, an HB antenna is accommodated within a bowl-shaped LB antenna. The hollow-cubed structure of the LB antenna in the embedded scheme reduces the blockage effect on HB antennas compared to the previous interleaved scheme. However, this arrangement cannot fully address cross-band interference, often requiring additional measures such as specially designed baffles or raising the height of HB antennas to ensure stable operation [20–24].

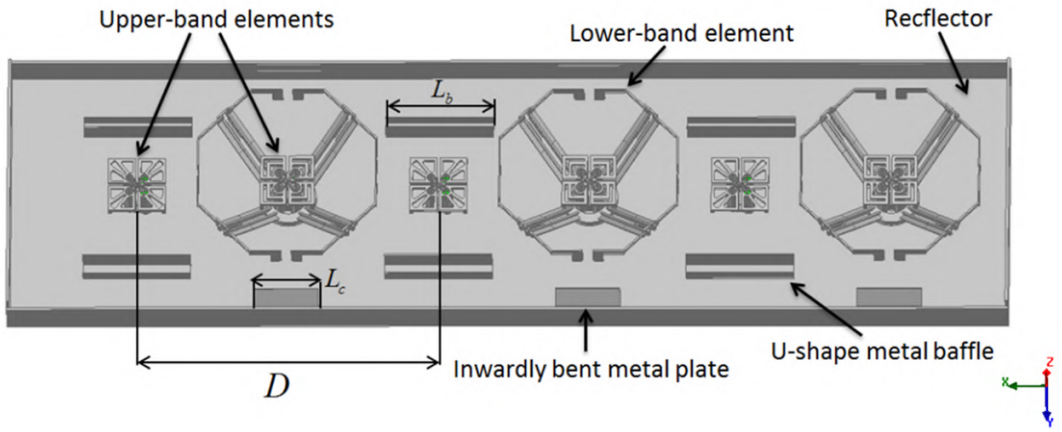

Figure 2.8: Configuration of the embedded-scheme-based dual-band array [20].

To mitigate cross-band interference from the LB antenna to the HB antenna, baffles are commonly used. U-shaped or arc-shaped baffles improve the front-to-back ratio (FBR) and reduce backlobe radiation, effectively isolating LB and HB antennas, and suppressing undesired mutual influence. Despite their effectiveness, using only baffles limits the HB bandwidth to approximately 23.7% (1.71-2.17 GHz) and can result in HB gain fluctuations of up to 3.4 dB [20–22].

Figure 2.9 shows the embedded-scheme-based dual-band array in [23], which incorporates various baffles and raises the height of the HB antenna. Raising the height of the HB antennas to the same level as the LB aperture can further alleviate the unwanted cross-band scattering influence. This method reduces gain fluctuation and ensures stable radiation patterns over a wider bandwidth up to 45.5% (1.7-2.7 GHz) [23]. Nonetheless, this operation compromises the structural stability of the HB antennas [23, 24].

In summary, each design strategy within the embedded scheme has distinct advantages and limitations. Baffles are simple and effective for enhanced LB-HB isolation but insufficient for ensuring stable HB performance over wider bandwidths and can increase complexity. Elevating HB antennas can also be effective but reduce structural stability. Both strategies require careful consideration to balance electromagnetic performance

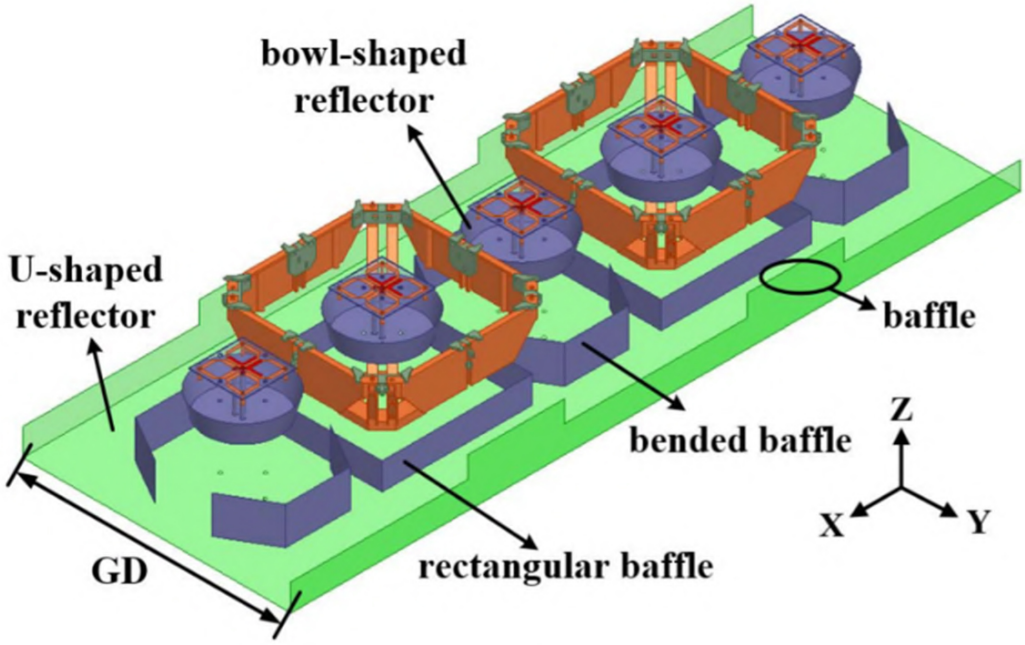

Figure 2.9: The embedded-scheme-based dual-band array from [23], incorporating various baffles and raising the height of the HB antenna.

and manage configuration complexity.

2.2.2.3 Stacked Scheme

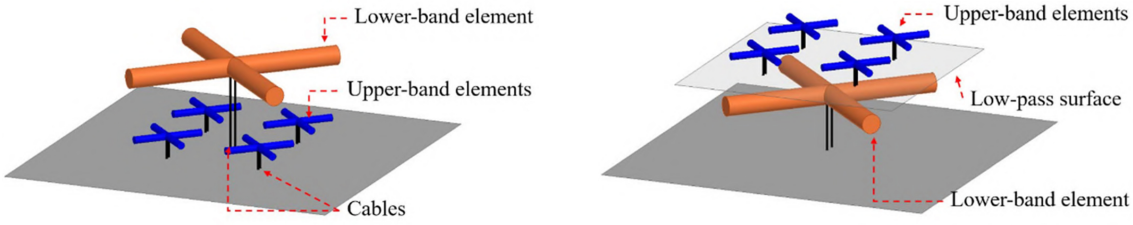

(a) (b)

Figure 2.10: Configuration of the stacked-scheme-based dual-band array [25]. (a) HB antennas positioned below the LB antenna. (b) HB antennas positioned above the LB antenna.

The stacked scheme, depicted in Figure 2.10, is a practical configuration for dual-band shared-aperture antenna arrays, where HB antennas are placed either above or below LB

antennas. An FSS is introduced between the two bands of antennas to electrometrically isolate them, thereby suppressing mutual interference and ensuring stable radiation performance [25–29].

The FSS serves two primary functions: it reflects signals from the antenna band placed above it to prevent interference with the antennas below, while allowing signals from the antennas below to pass through unimpeded. Additionally, the FSS provides capacitive loading, which enhances impedance matching for the antennas positioned above it.

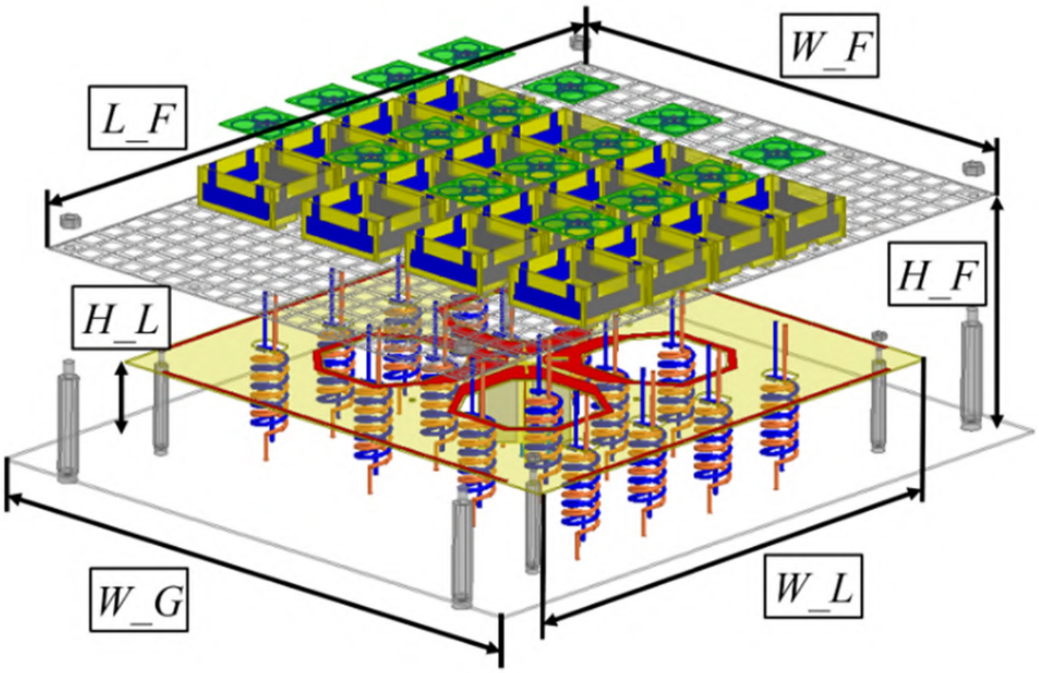

Figure 2.11: The stacked-scheme-based dual-band array from [27], incorporating helical torsion coaxial cables to feed the antennas placed above the FSS.

To further minimize cross-band interference, supplementary decoupling approaches such as helical torsion coaxial cables [27] or customized baffles [28, 29] are incorporated. The helical torsion cables in [27] exhibit open-circuit characteristics at the operating band of the antennas below the FSS, effectively suppressing detrimental impact from

the densely arranged cables while preserving radiation performance. Its structure can be referenced in Figure 2.11.

Despite its benefits, the stacked scheme introduces certain challenges. The increased stacked profile of the array may be unsuitable for compact installations or urban environments. Additionally, integrating FSSs or helical torsion coaxial cables adds to manufacturing complexity and cost. Compared to the interleaved and embedded schemes, the stacked scheme offers improved cross-band isolation through FSSs and flexibility in spatial arrangement but at the expense of increased height and design complexity.

2.2.2.4 Back Cavity Scheme

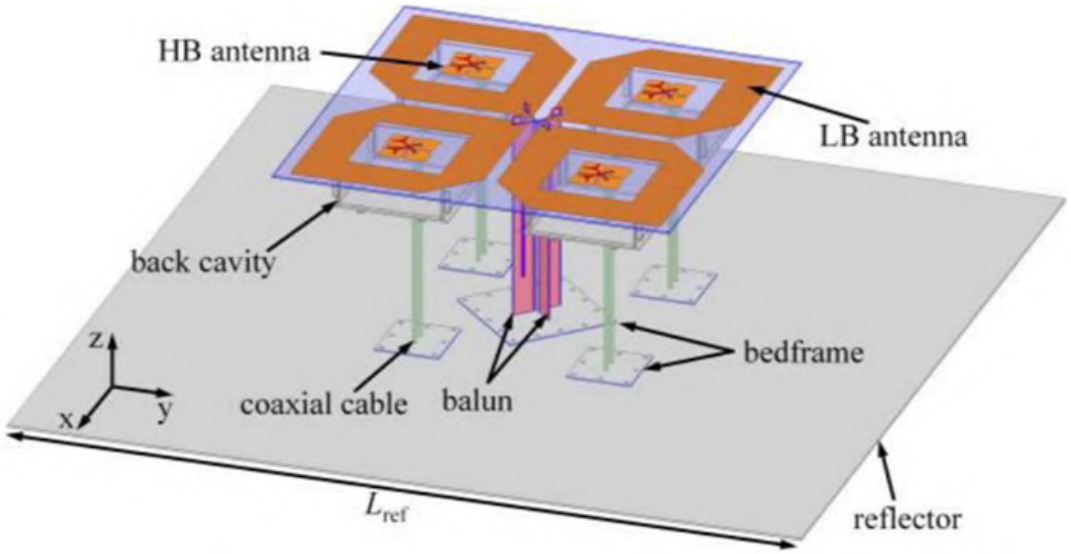

Figure 2.12: Configuration of the back-cavity-scheme-based dual-band array [30].

The back cavity scheme, depicted in Figure 2.12, offers another integrated solution for dual-band antenna arrays. It embeds HB antennas within the LB radiating arms, backed by metal cavities that act as HB reflectors [30, 31]. The LB radiators also function as reflectors for HB antennas. This design creates independent radiating environments for each band, allowing both bands to radiate with reduced interference.

This back cavity design has the following characteristics. First, the cavities act as reflectors for HB antennas, directing HB radiation outward and suppressing side and back lobes. Second, the cavities physically isolate HB antennas from LB radiators, reducing mutual cross-band impact and ensuring stable radiation performance. Third, for the LB antenna, these cavities act as electrical small structures, having minimal impact on LB radiation. Experimental implementations of the back cavity scheme achieve bandwidths of 0.69-0.96 GHz for LB and 3.3-3.8 GHz for HB, with port isolations exceeding 25 dB [30, 31]. This scheme provides compact and high-performance options for shared-aperture arrays.

In summary, the back cavity scheme eliminates the height challenges associated with the stacked scheme by maintaining a planar arrangement. However, HB antennas must have sufficiently small apertures to be embedded within the LB radiators, making this design ideal only for cases where the two bands are well-separated. Achieving optimal performance requires precise alignment and careful design of cavity dimensions, with considerations of manufacturing complexity. When evaluated alongside interleaved and embedded configurations, both schemes demonstrate their strengths in addressing specific design priorities, offering diverse options for shared-aperture multi-band array applications.

2.3 UWB antenna arrays

2.3.1 Consideration for Designing UWB antenna arrays

Integrating multiple narrowband designs in close proximity on the same complex electromagnetic platform inevitably needs to address the serious cross-band interference and consequent degradation of radiation performance. By covering the entire operating band with a single UWB array design, this problem can be avoided while significantly

reducing cost, power consumption, and space resources [32]. This has made the UWB antenna array a promising solution in modern communications systems. Designing UWB antenna arrays requires careful consideration of several critical factors:

1. Bandwidth and Impedance Matching: UWB antenna arrays must maintain stable impedance matching over a broad range of frequencies to achieve effective radiation and minimize signal reflections. This challenge becomes more pronounced when spanning multiple octaves of bandwidth. Designers must therefore leverage advanced methods such as multi-resonant element designs, essential reactance compensation loadings, or tapered feed structures that can stabilize impedance variations across UWB frequency coverage. Consistently low return loss underpins reliable signal quality, making bandwidth and impedance control critical for next-generation UWB systems.

2. Enhanced Beam Scanning Range: Supporting wide-angle scanning enables adaptability to different spatial coverage requirements, from satellite communication links to ground-based surveillance. However, significant impedance variations, radiation pattern degradation, and beam squint can arise when steering beams at large angles across a broad frequency range. This demands designs that minimize impedance variations and beam squint. Ongoing research in scalable and high-performance beam-scanning techniques continues to be essential for achieving fast, accurate, and broad beam-scanning coverage in practical UWB scenarios.

3. Effective Feeding without unwanted resonances: Feeding networks in UWB arrays must transform electromagnetic energy efficiently across multiple octaves, avoiding degraded modes-such as common-mode resonances-and minimizing ohmic losses to maintain high transmission efficiency. Achieving these goals often involves low-loss transmission lines, careful layout geometry, and effective common-mode current control. Since UWB arrays typically operate over a broad range of wavelengths, each feeding part must be meticulously designed to prevent parasitic coupling effects and ensure

consistent phase and amplitude distribution.

4. Compact Implementation: Compact and lightweight implementations are increasingly in demand for advanced applications with stringent space constraints. Beyond simply minimizing physical dimensions, a compact configuration must also preserve enhanced bandwidth, gain, and radiation characteristics. Achieving this often involves strategies such as folded/meandered radiators or feeding lines, and advanced materials (e.g., low-loss dielectrics or flexible substrates) that maintain compactness without compromising electromagnetic performance Ensuring seamless compact integration and mechanical robustness further expands the array's suitability across diverse deployment scenarios.

2.3.2 Realization Forms of UWB antenna arrays

Numerous UWB antenna array designs have been developed over the past decades. Among them there are mainly two types: one is to design the UWB antenna element first, and then replicate and expand it into an array. A major drawback of this method is that interelement coupling can only be considered after the antenna elements have been designed, which can lead to substantial impedance changes and unpredictable scanning behavior once the array is formed. The second approach is designing the array as a whole from the beginning, utilizing interelement interactions to optimize both wideband and wide-scan performance. Necessarily, the differences between the infinite and finite counterparts need to be considered. The primary techniques for designing UWB and wide-scan antenna arrays can be summarized as follows.

2.3.2.1 UWB-Element-based Array

Antenna elements that exhibit desirable octave bandwidths and therefore can be selected to form UWB antenna arrays are usually spirals [33], conical helices [34], or log-periodic

elements [35]. Despite their favorable characteristics, these elements often present practical challenges, such as being excessively large for the desired array lattice or incompatible with planar implementations.

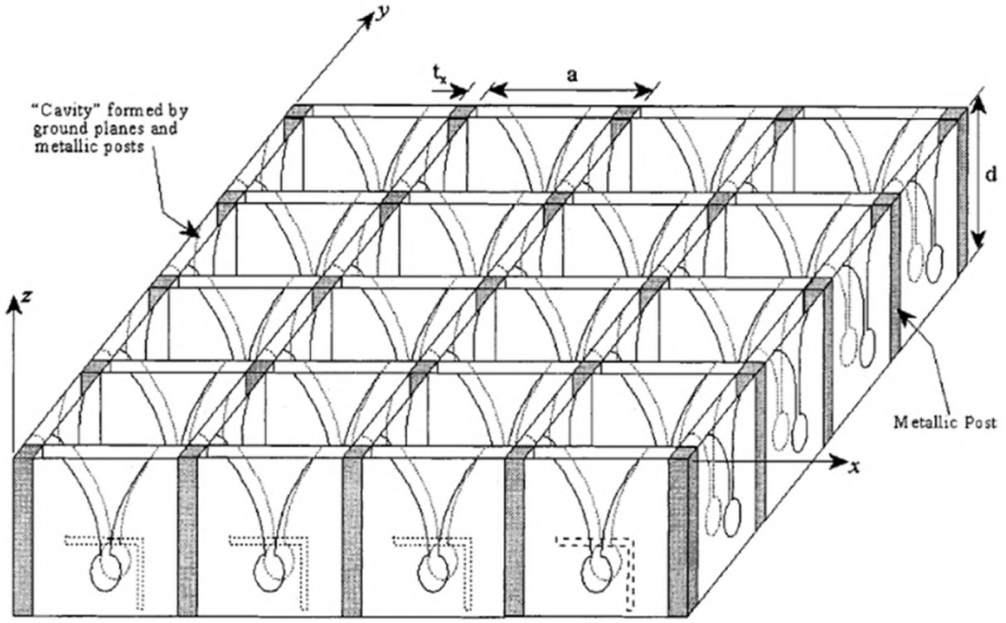

Figure 2.13: Configuration of a typical dual-polarized Vivaldi array [36].

Vivaldi antenna array, also known as tapered slot/flared notch antenna array, has emerged as a widely-used alternative in UWB applications [36–38]. Figure 2.13 shows a 4×4 dual-polarized Vivaldi array. Typically, the Vivaldi arrays can operate over 10:1 bandwidth and 45° scanning angle with VSWR <2:1 [39]. Theoretically, the impedance bandwidth of the Vivaldi antenna element is proportional to its longitudinal dimension [40]. Aiming to accomplish excellent broadband impedance matching performance, its longitudinal size is relatively large, usually 2–3 λ_{high} (λ_{high} represents the wavelength at the highest frequency). The excessive profile leads to elevated cross-polarization levels when scanning off broadside, due to the presence of strong currents perpendicular to the array plane along the slot line direction. These currents can cause the “polarization reversal” phenomenon where the cross-polarized radiation level exceeds the co-polarization

level, especially in D-plane scanning. This may occur even at scan angles as low as 30° [41].

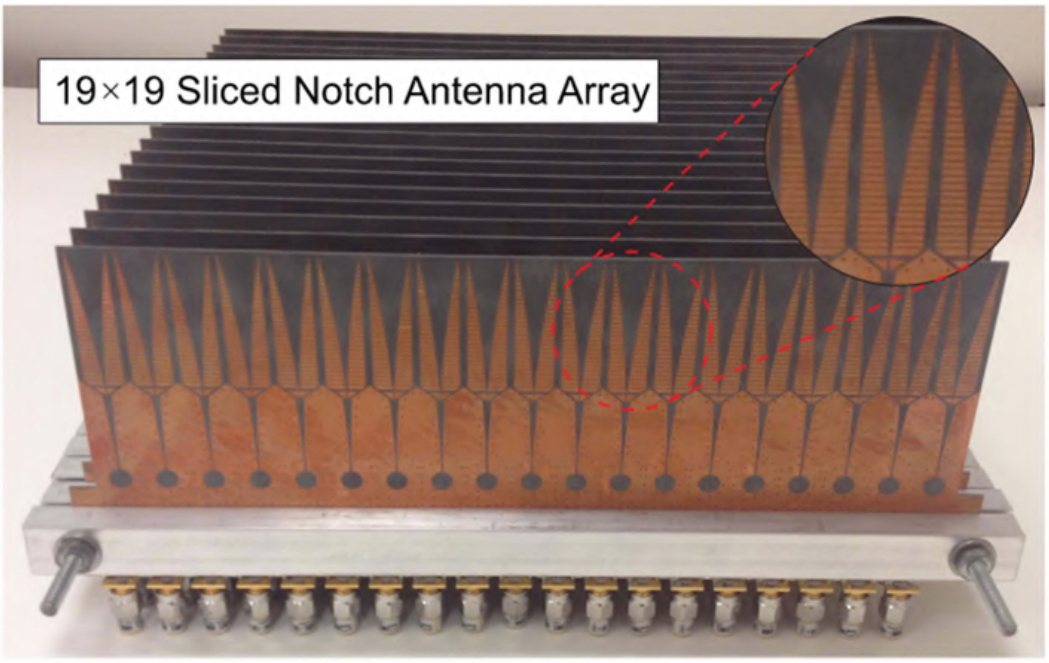

Figure 2.14: Configuration of the Sliced Notch Antenna (SNA) array [42].

In [42, 43], the Sliced Notch Antenna (SNA) array achieves effective control of cross-polarization by cutting the original radiating fins into discrete slices, as shown in Figure 2.14. Following this operation, the vertical current vector on the slotted line can be selectively regulated and constrained. It is demonstrated that the polarization purity of the SNA is improved by more than 20 dB at the high frequency in the D-plane [42]. However, the profile is still as high as $3\lambda_{\text{high}}$, which will limit its application in certain scenarios.

2.3.2.2 Tightly-coupled dipole array (TCDA)

Another class of UWB antenna array, referred to as the current sheet array (CSA), has drawn great attention in recent years. The CSA is based on Wheeler's current sheet theory [44, 45], operating differently from that of the traditional antenna array. Based

on a hypothetical waveguide model, it is derived that the radiation impedance of the elements placed in an infinite planar current sheet under the open boundary condition does not vary with frequency, implying an infinite impedance bandwidth.

A typical CSA form is the tightly-coupled dipole array (TCDA) [46, 47]. It works by setting up densely arranged dipoles to mimic an equivalent electric current sheet with continuous and uniform current sheet distribution, thereby achieving UWB operation. It has several well-known advantages including extremely wide bandwidths, compact sizes, low profiles, and improved cross-polarization performance [48]. This section presents notable advancements in TCDA, focusing on bandwidth enhancement, extended beam scanning range, and feeding network designs, with selected works illustrating the key principles and implementation strategies.

A. Bandwidth enhancement While TCDAs theoretically exhibit infinite bandwidth in open-boundary conditions, practical implementations require a ground plane (GP) for unidirectional radiation. The inclusion of a GP introduces significant inductance at low frequencies, resulting in impedance mismatches and bandwidth limitations. Additionally, short-circuit bands arise when the distance between the dipole and the GP is about $N\lambda/2$ (where $N = 0, 1, 2, 3, \ldots$). In these frequency bands, upward-radiated waves and GP-reflected waves have equal amplitude but opposite phase, leading to mutual cancellation and severely impairing the array's radiation efficiency. Consequently, these short-circuit bands constrain the operational bandwidth of the array.

The inductance brought by GP at the low-frequency end can be compensated by introducing capacitive coupling between adjacent dipoles. Figure 2.15 illustrates a single-polarized TCDA where the dipole arm is modified with interdigital edges to enhance mutual capacitive coupling. Usually, the bandwidth of a TCDA is around 4:1 through inducing capacitance inter-element coupling [46, 49]. By incorporating materials such as dielectric superstrates, the bandwidth can increase up to about 12:1 [50]. Notably,

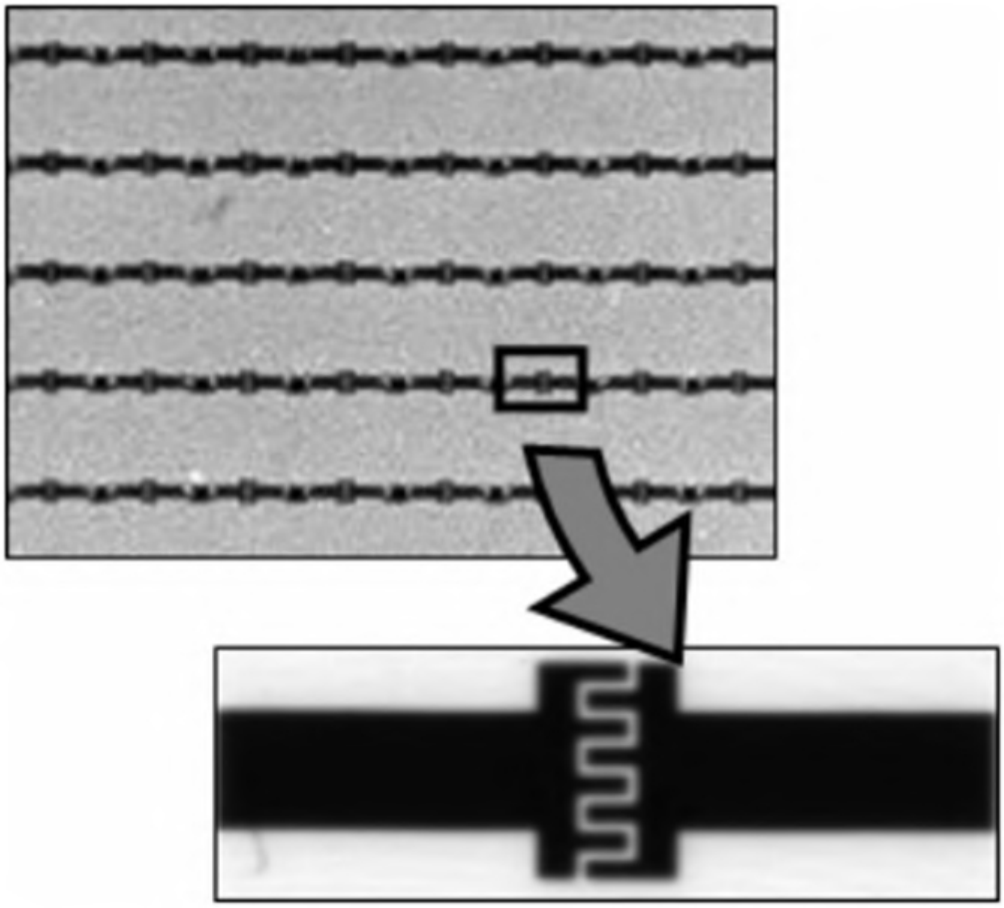

Figure 2.15: Interdigital-edge loaded dipoles for enhanced capacitive coupling in TCDA [49].

some coupling loading designs demonstrate instantaneous bandwidths reaching 10:1 without resorting to lossy materials or dielectric superstrates [51, 52]. However, the short-circuit effect caused by the GP poses significant challenges in further extending the bandwidth [47].

Highly lossy materials are usually incorporated to address short-circuit resonances. For instance, resistive cards are inserted between the dipole surface and the GP [53–55]. By optimizing the unit resistance, geometry, and height of these resistive materials, their absorbing frequency range can be aligned with the short-circuit resonances. This operation facilitates the absorption of backward-radiated waves, effectively eliminating

the short-circuit effect. Such a design enables a significant bandwidth expansion of up to 46:1 by addressing multiple short-circuit bands, and the fabricated array prototype is shown in Figure 2.16 [55]. However, the inclusion of lossy components inevitably reduces the array's radiation efficiency, which remains at approximately 73%, even with partial compensation provided by the superstrate.

An alternative design employs a polarization-converting GP to address the short circuit without the use of resistive parts. By shifting the polarization of reflected waves, this approach achieves a bandwidth of 20.9:1 while maintaining high radiation efficiency [56]. The fabricated array structure is shown in Figure 2.17. The polarization conversion by the GP effectively prevents wave cancellation that typically leads to short-circuit bands, thereby broadening the operational bandwidth. However, this design induces elevated cross-polarization levels, which compromise radiation purity and limit its applicability to polarization-insensitive applications.

In summary, this part discusses key strategies for the bandwidth enhancement of TCDAs. First, capacitive compensation is often introduced to counteract the inductance caused by the GP. This approach typically achieves about a 4:1 bandwidth. However, achieving larger bandwidths, especially for over 10:1, requires addressing the short-circuit effect. Commonly, resistive materials are added to eliminate short-circuit resonances, but this solution reduces the array's radiation efficiency. Meanwhile, polarization conversion offers another strategy. It does not rely on resistive materials, yet it is limited to polarization-insensitive scenarios where high radiation purity is not a strict requirement. Achieving an optimal balance among bandwidth, efficiency, and radiation performance necessitates careful consideration of these trade-offs. Future investigations may explore hybrid methodologies and advanced material technologies, which have the potential to extend bandwidth while preserving high levels of radiation efficiency and purity.

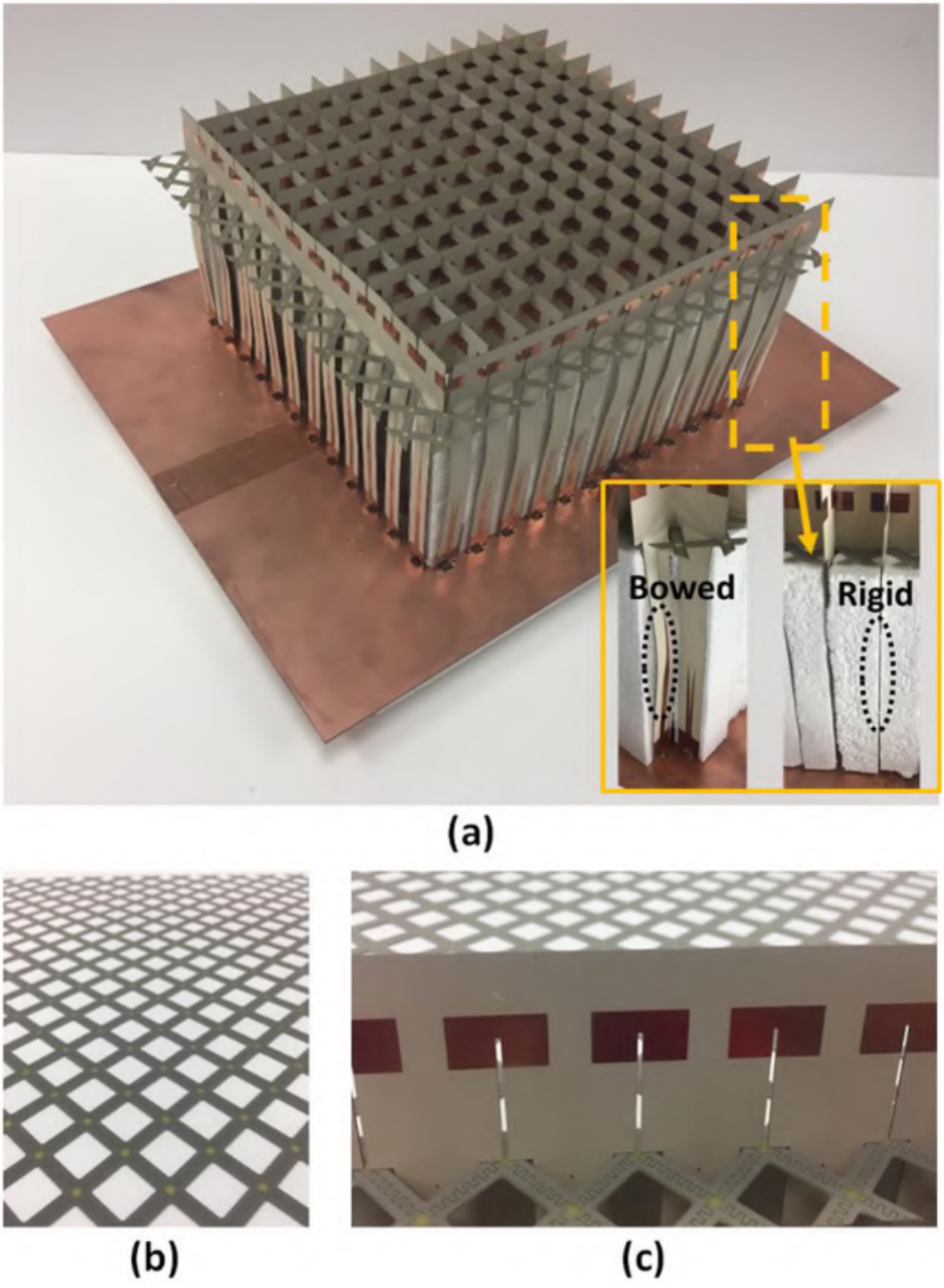

Figure 2.16: Prototype of the TCDA achieving 46:1 bandwidth with resistive FSS. (a) 12×12 finite array. (b) Resistive FSS. (c) Vertical dipole substrate [55].

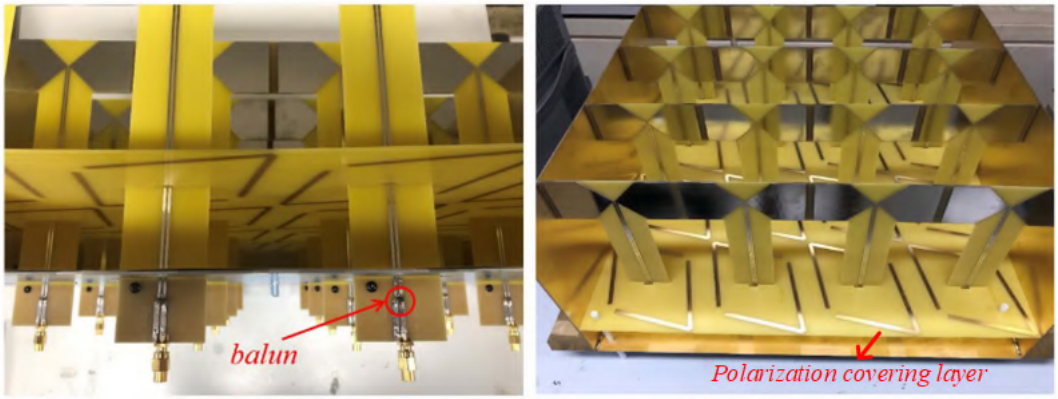

Figure 2.17: Prototype of the TCDA achieving 20.9:1 bandwidth with polarization-converting GP [56].

B. Enhanced Beam Scanning Range Wide-angle scanning performance of an antenna array is influenced by both the active element pattern (or embedded element pattern) and the active input impedance [57]. The active element pattern is the element pattern within the array environment when all other elements are terminated with matched loads. To achieve wide-angle scanning, elements with wide beams are necessary. Both the Vivaldi array and TCDA, as mentioned earlier, are composed of such elements. However, mutual coupling causes the active input impedance to vary notably with scan angles, so minimizing impedance fluctuations is essential to maintain stable scanning performance.

Wide-angle impedance matching (WAIM) designs effectively mitigate significant variations in active element impedance [58]. A common approach involves loading one or more dielectric superstrates as WAIM layers above the array to enhance the active impedance properties [47, 59, 60]. Figure 2.18 shows a TCDA loaded with dielectric superstrates, achieving scan angles up to 60° [60]. However, high dielectric constant layers can excite surface waves, leading to scanning blindness [59, 60]. While reducing the dielectric constant through regular perforations can mitigate this issue, it also increases the weight and cost of the array.

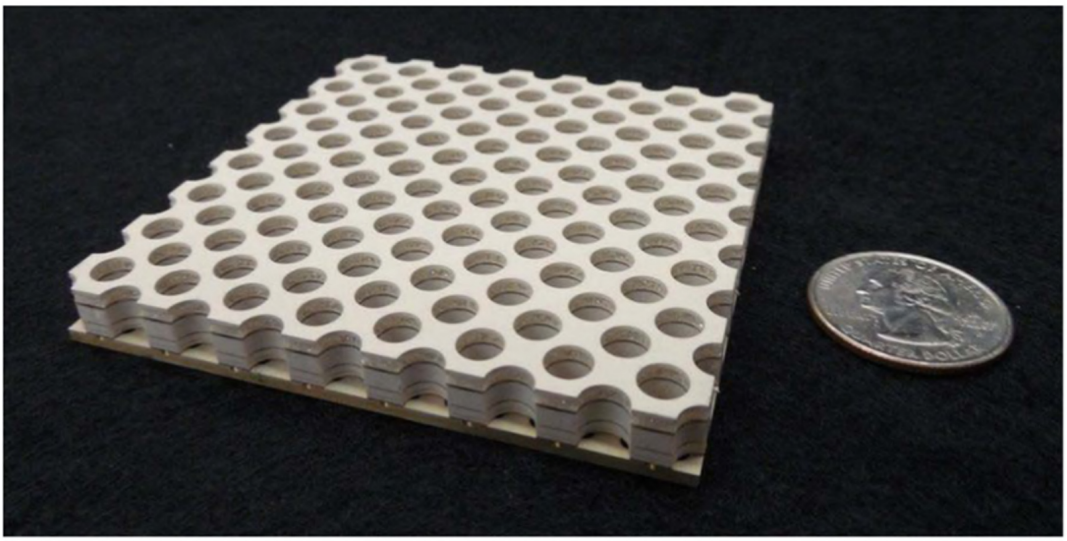

Figure 2.18: Prototype of the TCDA loaded with perforated dielectric superstrates for WAIM design [60].

Several lightweight PCB-based WAIM designs have been proposed in the literature. For instance, the FSS-based WAIM layout shown in Figure 2.19, which was constructed on the same substrate with the dipole array, facilitates scanning ranges of {¬±75°, ¬±70°, ¬±60°} in the {E-, D-, H-} planes, with a 6.1:1 bandwidth and a VSWR of less than 3.2 [61]. However, as the operating bandwidth increased to 9:1 or higher, scanning performance in the H-plane significantly degraded, with the VSWR rising above 6 [14, 20]. Other WAIM approaches such as metasurfaces [62–64], multilayer metallic strips [65], and planar split rings [66] enable TCDAs to achieve a maximum scan angle of 70° in one plane. For instance, the metasurface WAIM design in Figure 2.20 allows the TCDA to achieve a 5.5:1 bandwidth while scanning up to 70° in the E-plane and 55° in the H-plane [62, 63]. These approaches focus on bandwidths of less than a decade, simultaneously offering desirable features such as low profile, reduced cost, and ease of fabrication.

In summary, WAIM techniques play a pivotal role in maintaining stable performance across wide scan angles for TCDAs and other wide-beam arrays. While various methods-ranging from dielectric superstrates to lightweight PCB-based WAIM solutions-

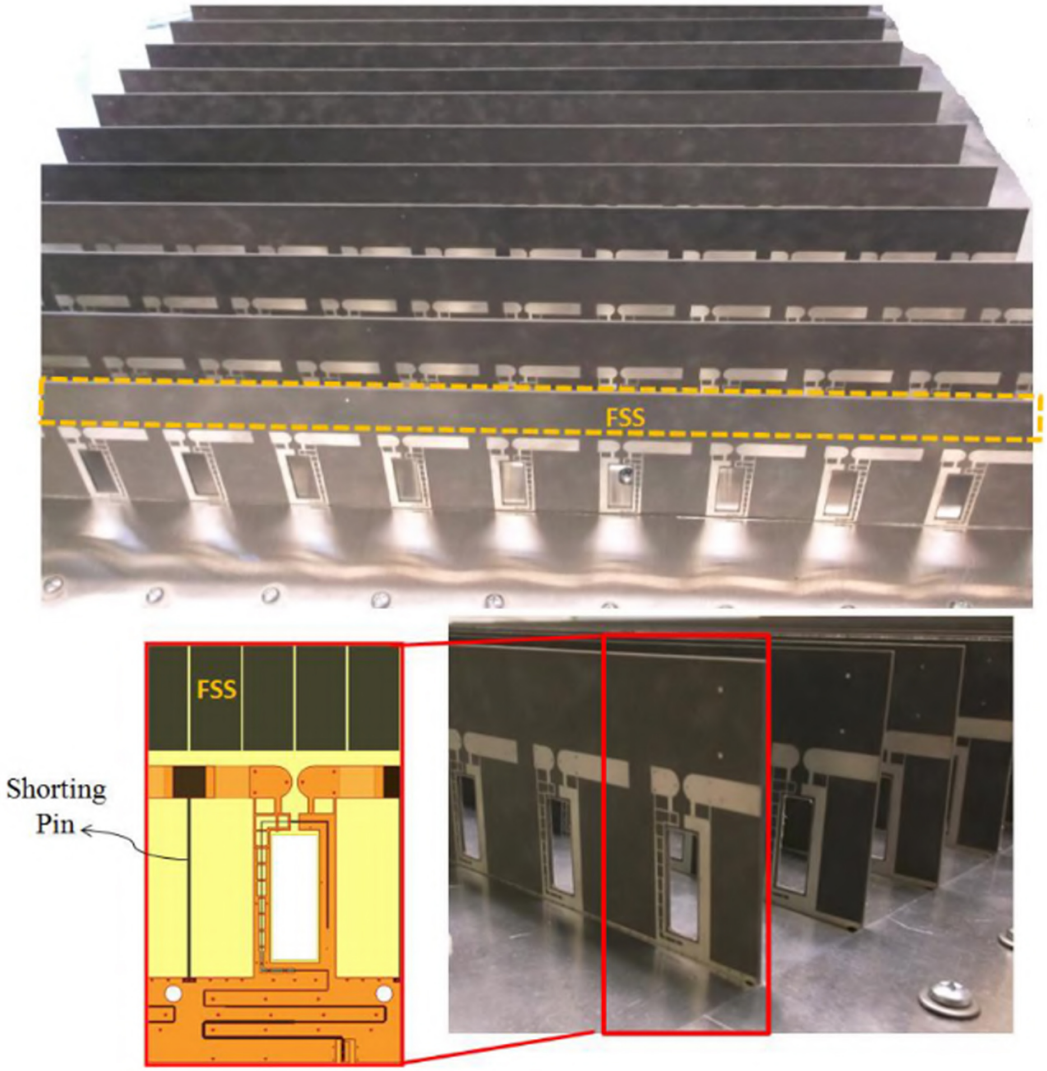

Figure 2.19: Prototype of the TCDA loaded with FSS for WAIM design [61].

can mitigate impedance fluctuation and enhance scanning, their trade-offs in terms of bandwidth, scanning stability, weight, and cost require careful consideration. Ongoing research in novel materials, advanced fabrication, and optimized coupling strategies offers promising avenues to further expand both the bandwidth and scan range of phased array systems.

B. Feeding design without bad resonances Feeding schemes for a CSA aim to transform a 50 Ω unbalanced input to about 100–200 Ω at a radiator port while avoiding

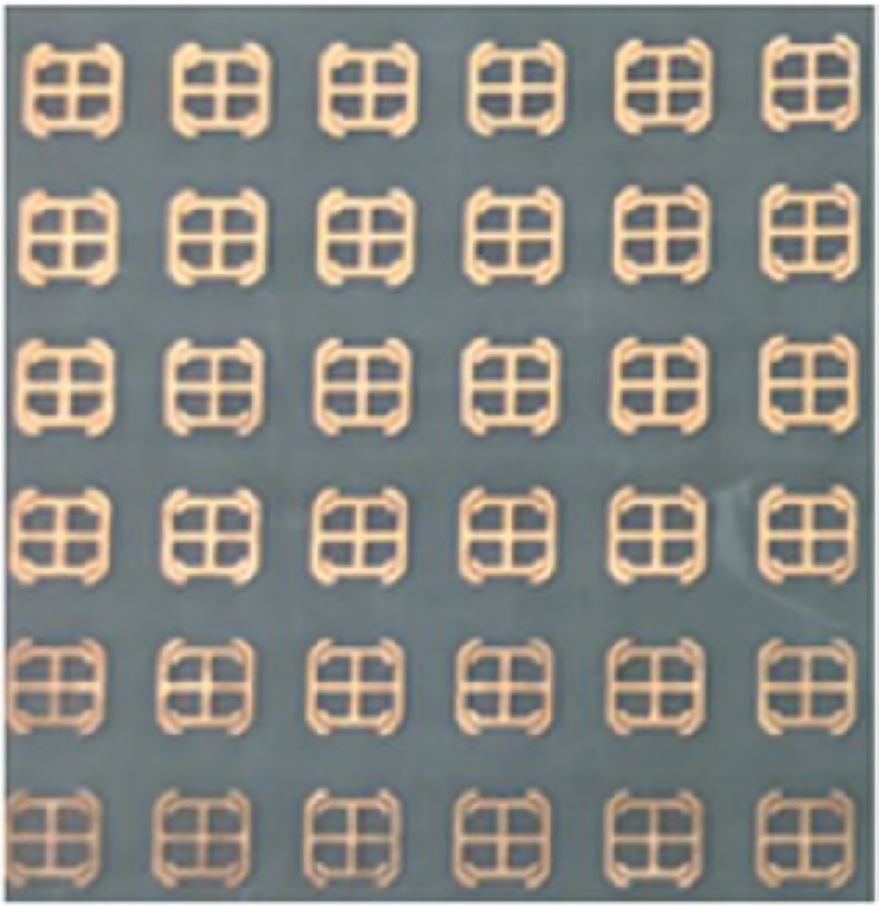

Figure 2.20: Prototype of the 6×6 metasurface WAIM design for the TCDA [62].

undesired resonances. Typically, when long feeding lines are integrated into a densely arranged periodical array, coupling between adjacent unit cells can induce common-mode currents on the feeding lines and dipole arms [67, 68]. These currents can result in undesirable common-mode resonances, significantly reducing the operational bandwidth of the array.

The initial feeding design for a TCDA utilizes the “feed organizer”, as shown in Figure 2.21 [49]. Each feed organizer includes four coaxial cables for a dual-polarized array unit cell and offers broadband common-mode suppression. However, it requires additional 0°/180° hybrids to generate the necessary phase difference, and its non-compact structure occupies extra space.

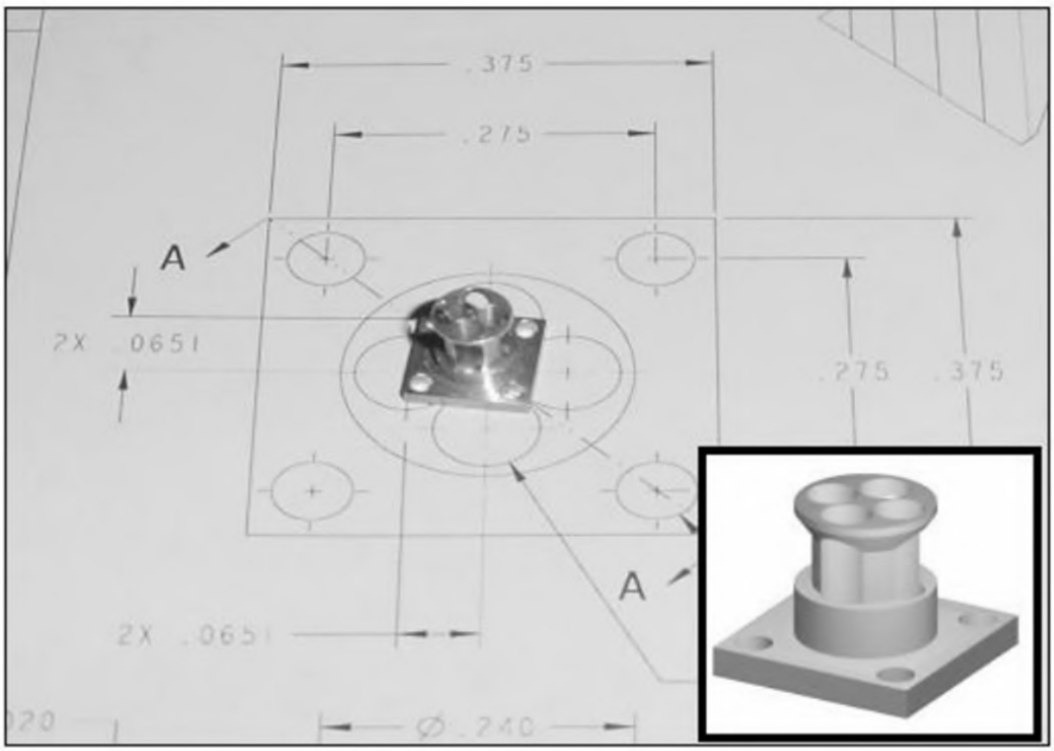

Figure 2.21: Prototype of the “feed organizer” [49].

Some TCDAs adopt unbalanced feeding without incorporating baluns. In such designs, each array unit cell is directly excited by a coaxial cable: the cable’s outer conductor is soldered to the GP, and the center conductor attaches to one dipole arm. The other arm is grounded via shorting vias [69], plated vias [59], capacitively-loaded vias [60], or capacitively metallic walls [70]. This approach suppresses common-mode currents and achieves common-mode rejection. Figure 2.22 illustrates the configuration of the array unit cell from [69], where shorting vias are used to tune out the common-mode resonance that often arises near the mid-band due to unbalanced feeding. However, these designs typically support bandwidths below one decade, with a maximum reported 6.5:1 bandwidth [70].

The other TCDAs employ balanced feeding configurations, where UWB baluns are critical components. Various commercial balun designs have been developed to support

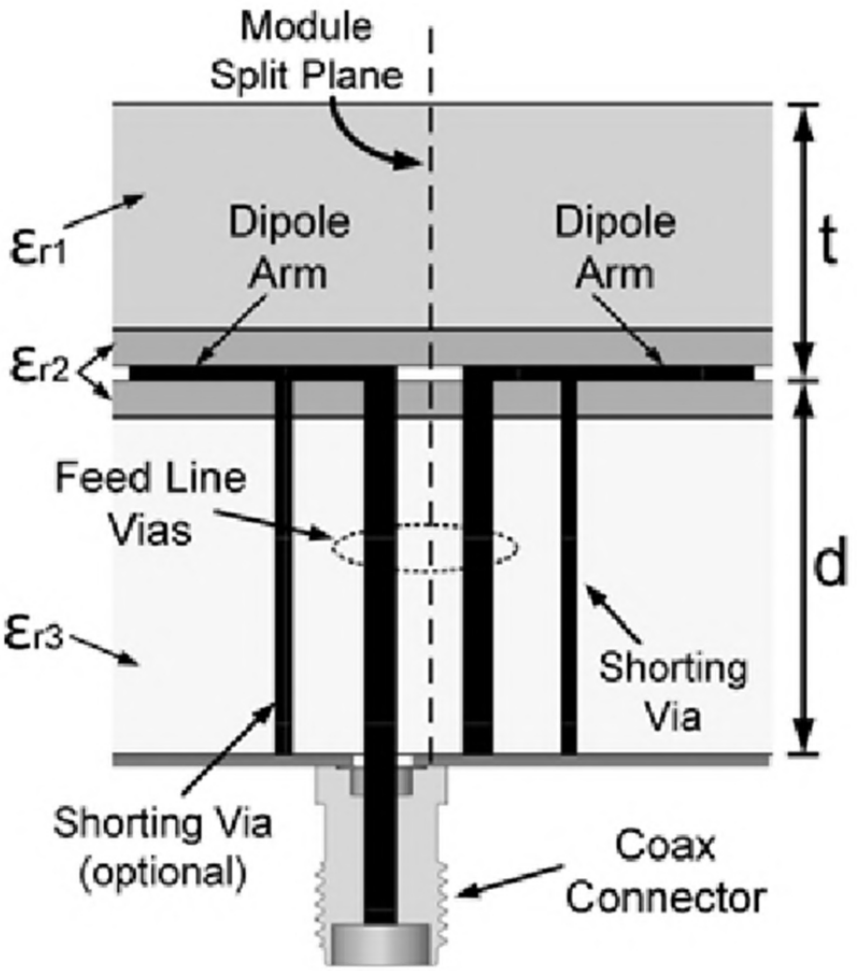

Figure 2.22: Side view of a TCDA unit cell using shorting vias for common-mode suppression [69].

wideband applications while simultaneously suppressing common-mode resonance. These include aperture-coupling-based transformers [67, 68, 71], double-Y baluns [72, 73], and Marchand baluns [54, 61, 74], tapered baluns [75, 76].

For aperture-coupling-based transformers [67, 68, 71], in [67, 71], the use of a coplanar strip-line (CPS) to grounded coplanar strip-lines (GCPS) transformer effectively shortens the electrical path between the dipole arms and the feed circuit. This configuration allows for the tuning out of common-mode resonance at the high-frequency end. However, due to the loop length defined by the structure, the differential bandwidth of

this design remains narrow. By incorporating radial/circular stubs [68], the differential mode bandwidth can be extended to a 10:1 bandwidth, but this structure does not facilitate impedance transformation. Similarly, while double-Y baluns [72, 73] can achieve a 10:1 bandwidth, they also do not provide impedance transformation capabilities.

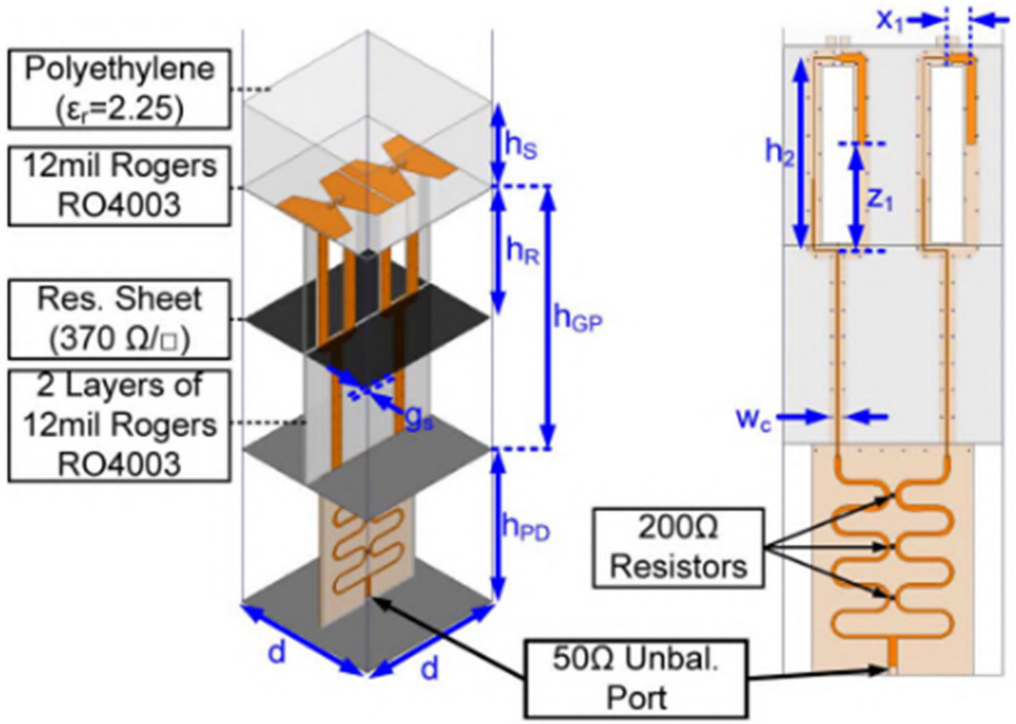

Figure 2.23: Configuration of the TCDA unit cell using the Marchand balun and power divider [54].

Marchand baluns [54, 61, 74] can suppress common-mode resonance and offer some degree of impedance transformation, with a widest achieved bandwidth of 13.9:1 [54]. However, additional components, such as power dividers or striplines, are needed to convert the high impedance at the unit port to the required 50 Ω. Figure 2.23 illustrates the configuration of a TCDA unit cell that employs a Marchand balun in conjunction with a power divider to achieve both common-mode suppression and impedance transformation [54].

Tapered baluns [55, 75–77] offer an attractive solution by achieving a high impedance

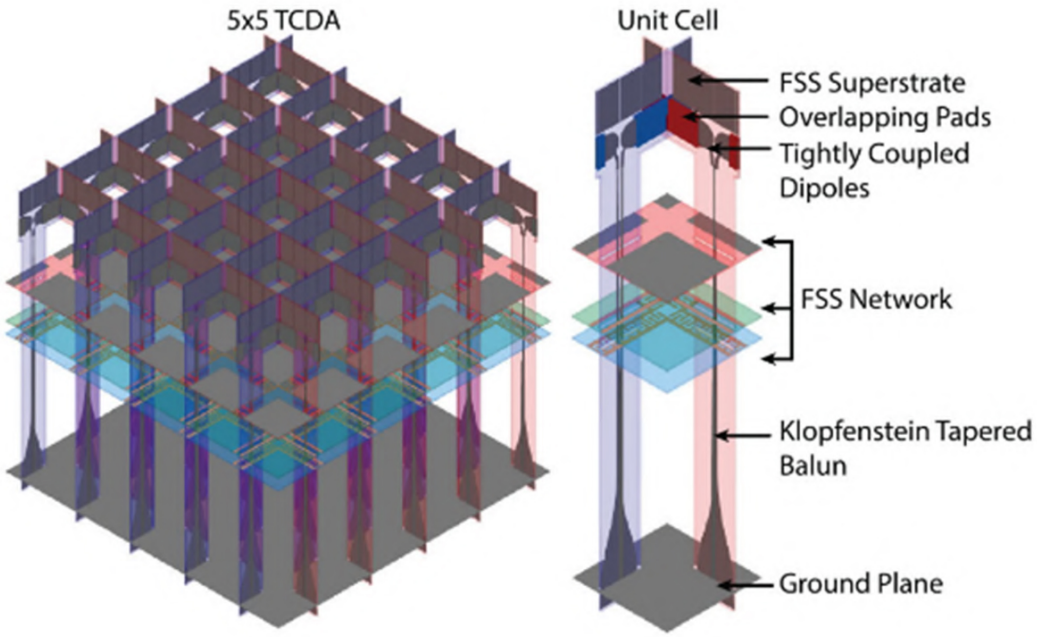

Figure 2.24: Configuration of the TCDA using the Klopfenstein tapered balun [77].

transformation ratio with simple single-substrate layouts. Figure 2.24 depicts the configuration of a TCDA utilizing the Klopfenstein tapered balun, achieving a bandwidth up to 28:1 [77]. What should be noted is that tapered baluns are typically employed in arrays constructed with lossy materials, which help suppress common-mode resonance. Therefore, for arrays operating over a decade of bandwidth without the use of absorbing materials, it becomes crucial to implement additional feeding schemes specifically designed to mitigate unwanted resonances.

In summary, TCDA feeding designs focus on achieving UWB impedance transformation and suppressing common-mode resonances. While unbalanced feeding designs with shorting vias offer simplicity, they typically operate in limited bandwidths to below one decade. Balanced feeding using UWB baluns, such as aperture-coupling-based transformers, double-Y, Marchand, and tapered baluns, provide wider bandwidth, albeit with varying impedance transformation capabilities. Tapered baluns offer the widest bandwidth, but are typically used in arrays with lossy materials that do not face common-mode

resonance challenges. For wideband TCDAs without absorbing materials, additional resonance-mitigation strategies are necessary. Overall, each feeding design presents distinct advantages and is suitable for different design scenarios based on the specific requirements of the TCDA.

2.4 Identified Research Challenges

Building upon the design considerations and comprehensive literature review in Section 2.2 and 2.3, this section identifies key research challenges that remain unresolved in multi-band and UWB antenna array designs. While these two types of arrays have distinct design requirements, they share many common challenges, such as impedance matching, beam scanning performance, structural compactness, and efficient feeding networks. Addressing these challenges is essential to advancing next-generation wireless communication systems.

2.4.1 Challenges in Multi-Band and UWB Antenna Arrays

1. *Ensuring Multi-Band / UWB Stable Radiation Performance*

Both multi-band and UWB antenna arrays require consistent radiation performance across multiple frequency bands or a broad continuous spectrum. However, challenges such as impedance mismatches, variations in realized gain, and radiation pattern distortions persist. Current techniques, including FSSs, choke-based filtering, and capacitive loading, provide partial solutions but often require trade-offs in bandwidth or efficiency. Further research is needed to achieve stable radiation characteristics without compromising other design aspects.

2. *Optimizing Impedance Matching and effectively managing mutual coupling*

In multi-band arrays, mutual coupling between antenna elements often leads to cross-band interference, degrading impedance matching and radiation performance,

thus necessitating suppression. Conversely, in certain UWB arrays, such as TCDA, mutual coupling can be exploited to enhance impedance bandwidth. Therefore, effective mutual coupling management is crucial,Äînot only to mitigate adverse effects but also to harness its benefits. The challenge lies in striking a balance where impedance matching is optimized while mutual coupling is strategically controlled to enhance overall array performance.

3. *Achieving Wide-Angle Beam Scanning with Minimal Performance Degradation*

Antenna array systems are expected to maintain beam integrity across wide scanning angles, but both multi-band and UWB antenna arrays encounter challenges such as beam squint, radiation pattern degradation, and impedance variations. Wide-angle impedance matching (WAIM) techniques, coupled with innovative element designs, can help mitigate these effects, though current implementations still require significant optimization for practical deployment.

4. *Advanced Feeding Networks and Suppression of Undesirable Resonances*

Feeding network design is critical for both multi-band and UWB antenna arrays, as it directly impacts impedance matching, phase distribution, and overall efficiency. Unwanted resonant modes such as common-mode resonances can degrade performance, particularly in wideband scenarios. Research into improved feeding techniques, such as wideband balun designs, common-mode-rejection shorting structures, differential feeding methods, and hybrid networks, is essential to achieving efficient energy distribution with minimal loss.

5. *Compactness, Structural Integration, and Manufacturability*

Shared-aperture integration in multi-band arrays and closely spaced elements in UWB antenna arrays introduce constraints on size, weight, and material properties. Achieving compact and lightweight designs while maintaining performance is an ongoing challenge, particularly for mobile and airborne applications. Innovations in high-

performance materials and manufacturing techniques could enhance structural integration while ensuring electromagnetic stability.

6. *Cost, Scalability, and Long-Term Stability*

Large-scale deployment of advanced antenna arrays is often hindered by manufacturing complexity and cost. Many high-performance techniques, such as metasurface-based filtering and dielectric superstrate enhancements, introduce challenges in mass production and material consistency. Additionally, environmental factors such as temperature variations, mechanical stress, and aging effects can lead to performance degradation over time. Addressing these challenges requires robust design methodologies that consider manufacturability, cost-effectiveness, and long-term reliability.

2.4.2 Towards Unified Solutions for Multi-Band and UWB Antenna Arrays

While multi-band and UWB antenna arrays have traditionally been studied as separate categories, their shared challenges suggest that unified design strategies could lead to more efficient and flexible solutions. Future research could focus on:

- **Hybrid Aperture-Sharing Design Strategies:** Exploring innovative shared-aperture configurations that integrate multi-band and UWB functionalities within a single antenna system.
- **AI-Assisted Optimization and Automated Tuning:** Leveraging AI and machine learning for rapid design iterations, performance optimization, and adaptive tuning.
- **Novel Materials and Additive Manufacturing for Enhanced Performance:** Investigating the use of advanced materials, such as low-loss dielectrics and conduc-

tive polymers, to improve performance while reducing weight and manufacturing costs.

- **Multi-Functional and Reconfigurable Antenna Technologies:** Developing antennas capable of dynamic reconfiguration to adapt to changing frequency and beamforming requirements in real-time applications.

By addressing these challenges and exploring unified solutions, this research aims to contribute to the advancement of next-generation multi-band and UWB antenna arrays, paving the way for more efficient, adaptable, and high-performance wireless communication systems.

CHAPTER 3

MULTI-BAND SHARED-APERTURE ANTENNA ARRAY BASED ON EMBEDDED SCHEME

This chapter introduces an embedded dual-band array with wideband cross-band scattering suppression capabilities. By integrating innovative helical filters into the LB radiators, the undesired scattering effects from the LB antenna on the HB antennas are significantly reduced. This demonstrates a successful implementation of filtering structures within embedded schemes for multi-band antenna arrays, achieving a remarkably wide HB de-scattering bandwidth of 1.36-2.72 GHz (66.7%). Additionally, the LB antenna achieves enhanced impedance matching within 0.8-0.96 GHz (17.1%) due to the inclusion of specially designed LC series circuits in its baluns. Its compact aperture improves LB in-band isolation, while customized 3D-printed T-shaped supports ensure mechanical stability. The measured results of the fabricated array closely align with the simulations, validating the performance and reliability of the embedded shared-aperture array design.

3.1 Introduction

The continued growth in demand for high-speed, high-quality signal transmission in modern mobile communication systems has led to increasingly stringent performance requirements for base station antenna (BSA) arrays. To fulfill the large network capacity requirements in these systems, BSAs must effectively cover multiple frequency bands [2]. In typical dual- and multi-band BSAs operating in the sub-6 GHz spectrum, the LB typically includes standards such as GSM700 (698–793 MHz), GSM850 (824–894 MHz), and GSM900 (880–960 MHz), whereas the high-frequency band (HB) spans 1710–2690 MHz, encompassing DCS (1.71–1.88 GHz), PCS (1.85–1.99 GHz), UMTS (1.92–2.17 GHz), LTE2300 (2.3–2.4 GHz), and LTE2500 (2.5–2.69 GHz). Recently, frequencies in the 1.4–1.7 GHz range have also been adopted in certain regions for 4G LTE and 5G NR per 3GPP specifications. Consequently, integrating this band into the upper frequency range is essential, resulting in an expanded high-frequency band spanning 1.4-2.7 GHz with an approximately 63.4% fractional bandwidth.

Although several single-band BSA designs have addressed this wider bandwidth [78–80], it remains challenging to integrate such wideband elements into dual-band arrays. One key concern is *cross-band scattering*, which occurs when antennas working in different frequency bands share the same aperture. In practice, LB antennas generally exert a larger scattering effect on HB antennas, due to their larger electrical size [2]. Minimizing cross-band scattering is essential for achieving reliable multi-band BSA array solutions.

Existing methods for mitigating cross-band scattering in dual-band arrays can be categorized into two principal approaches. The first involves designing new array schemes to physically isolate the LB and HB antennas; for instance, using stacked schemes [26, 30] or cavity-backed schemes [30]. These schemes often incorporate frequency-selective surfaces (FSSs) [26, 28] or cavities [30] to prevent the LB antenna from obstructing

HB radiation. However, doing so commonly requires elevating either the HB [26, 30] or LB [28] antennas, complicating the overall design. The second approach focuses on modifying the LB antennas themselves to make them electromagnetically "invisible" at higher frequencies [1, 81]. Possible techniques include employing chokes [1, 4], adding 2.5-D cloaking structures [13], or etching slots [6, 7] and U-shaped structures [10]. Alternatively, other methods involve integrating FSS-based [16, 17] or split-ring resonator (SRR)-based [18] filtering elements, or partially reflecting surfaces (PRSs) [81]. However, these methods often suffer from limited HB bandwidth, as attaining electromagnetic invisibility over a wide frequency range remains inherently challenging. Consequently, most dual-band BSA arrays implementing cross-band scattering suppression achieve a maximum fractional HB bandwidth of approximately 45.5% (1.7-2.7 GHz), which is lower than the 66.7% reported in this work.

Addressing the unwanted cross-band scattering across a wider bandwidth can potentially be resolved by the *bowl-shaped LB antenna*. Its hollow-cubed geometry greatly reduces blockage effects on adjacent HB antennas when when placed in an embedded array configuration, as depicted in Figure 3.1. In this setup, HB patterns can be largely recovered by adding specialized baffles or by elevating the HB antennas [21, 24]. But these operations incur increased cost and compromise the mechanical stability of the HB antennas. Additionally, the maximum HB bandwidth of such embedded array scheme is generally limited to around 45.8% (1.7–2.71 GHz) [24]. So far, there is no investigation regarding modifying LB antennas to enhance the suppression of scattering effects on HB antennas over a wider frequency range. Also, directly implement existing scattering mitigation methods [1, 81] for bowl-shaped antennas encounter considerable difficulties.

Figure 3.1: Side view of a typical base station antenna (BSA) array using an embedded scheme.

This work thus proposes an embedded shared-aperture array, employing an innovative filtered bowl-shaped LB antenna that achieves enhanced cross-band scattering suppression over an extended bandwidth. The proposed design allows the HB antenna to function well across 1.36-2.72 GHz (66.7%) without elevating its height:

1. **Wideband Cross-Band Suppression**: Cross-band scattering is effectively suppressed over 66.7%, the widest yet reported.

2. **Improved Impedance Matching**: A novel LB balun design is used to optimize LB matching while reducing its adverse impact on HB gain.

3. **Compact LB Design**: The LB antenna has a compact aperture of $0.38\lambda_{L_0} \times 0.38\lambda_{L_0}$, where λ_{L_0} is the LB center wavelength. This compact form significantly improves LB isolation in the array.

3.2 HB Antenna with Wide Impedance Bandwidth

Figure 3.2 depicts the structure of the proposed HB antenna, which adopts a crossed-dipole configuration. It consists of four radiating arms arranged in a square aperture, enabling $\pm 45^\circ$ dual-polarized radiation.

(a) (b)

(c)

Figure 3.2: HB antenna design. (a) Perspective view of the entire antenna. (b) Top view of the radiators. (c) Top view of the baluns. (Unit: mm).

Each of the four radiating arms comprises three square loops, which facilitate multiple resonances and broaden the operational bandwidth. The radiating arms are printed on the top side of a Rogers 4003 substrate ($\varepsilon_r = 3.55$, $\tan\delta = 0.002$, thickness = 1.016 mm), while the corresponding baluns are fabricated on both surfaces of FR-4 substrates ($\varepsilon_r = 4.4$, $\tan\delta = 0.02$, thickness = 1.016 mm).

Figure 3.3 shows the simulated S-parameters, radiation patterns, and realized gain of this HB antenna. Only +45° polarization patterns and gain are provided due to the antenna's symmetry.

(a) (b)

(c)

Figure 3.3: Simulated HB antenna performance. (a) S-parameters. (b) Radiation patterns in the yoz-plane. (c) Realized gain.

As seen in Figure 3.3(a), the antenna achieves a 64.7% impedance bandwidth (1.39–2.72 GHz) while maintaining reflection coefficients below −14 dB and port isolation exceeding 26 dB. Representative yoz-plane radiation patterns at 1.4 GHz, 1.7 GHz, 2.0 GHz, 2.35 GHz, and 2.7 GHz in Figure 3.3(b) indicate stable half-power beamwidths (HPBWs) of $66^\circ \pm 3^\circ$ throughout the band. The cross-polarization discrimination (XPD) exceeds 20 dB at boresight and remains above 10 dB for $-60^\circ < \theta < 60^\circ$. As illustrated in Figure 3.3(c), the realized gain ranges from 8.24 dBi to 9.72 dBi over the entire operating frequency range.

3.3 LB Antenna with Wide Scattering Suppression Bandwidth

Figure 3.4(a) illustrates the proposed ±45°-polarized LB antenna. The design comprises four sub-dipoles, each equipped with PCB baluns and supported by T-shaped dielectric structures, forming a hollow, cube-like bowl that can house one HB antenna. Sub-dipoles 1 and 3 are driven in-phase and with equal amplitude to generate +45° polarization, while sub-dipoles 2 and 4 operate similarly to yield −45° polarization.

The T-shaped dielectric supports in Figure 3.4(b) hold the metallic portions of the radiators, each comprising cuboid holders and cylindrical holders with helical grooves. Figure 3.4(c) illustrates the metallic components of the LB radiator, each consisting of two U-shaped enclosures and a helical filter. The helical filter is realized by winding a conductor within the helical grooves, whose dimensions are carefully tuned. Two U-shaped enclosures provide additional capacitance to counteract the significant inductance introduced by the helical filters.

Four baluns, each implemented on both sides of FR-4 substrates ($\varepsilon_r = 4.4$, $\tan\delta = 0.02$, thickness = 1.016 mm), feed the LB antenna [Figure 3.4(d)]. These baluns incorporate meander lines for added inductance and small rectangular patches on both surfaces for extra capacitance. Together, these components refine the matching response and reduce the effect on the HB antenna.

Figure 3.4(d) illustrates the structure of the LB balun, which is implemented on both sides of FR-4 substrates ($\varepsilon_r = 4.4$, $\tan\delta = 0.02$, thickness = 1.016 mm). The balun incorporates meander lines to increase inductance and small overlapping rectangular patches on both sides to enhance capacitance. These features improve LB matching and mitigate its negative impact on HB gain. The T-shaped supports, metal parts, and baluns in Figure 3.4(b)–(d) are manufactured individually and then assembled to form

the overall LB antenna shown in Figure 3.4(a).

Figure 3.4: LB antenna design. (a) Perspective view of the complete structure. (b) T-shaped dielectric support. (c) Metal portion of a radiator. (d) Top view of both sides of the balun. (Unit: mm).

3.3.1 Radiators with Wideband De-Scattering Capability

Helical filters are inserted into the LB radiators to suppress scattering at HB frequencies. These inductive coils can be modeled as a practical parallel circuit, exhibiting high terminal impedance at resonance while significantly decreasing on either side of it. This indicates that the helical structure can be utilized to achieve a low-pass, high-stop performance. By adjusting the dimensions of the helical structure, the low-pass, high-stop filtering response can be precisely tuned, forming a wide stop band. Furthermore, the insertion of the helical filter segments the LB radiators into electrically smaller sections, keeping them well below half-wavelength at the upper HB frequency limit. As a result, the LB antenna's impact on the HB antenna is significantly reduced.

In the initial simulation stage, to quickly verify the de-scattering capability of the filtered LB radiators, the monostatic radar cross section (RCS) results of both unfiltered and filtered designs are compared, as shown in Figure 3.5. While simulating the total scattering cross section (SCS) over the entire solid angle would provide a more comprehensive evaluation, it is time-consuming and requires more computing resources. Therefore, monostatic RCS analysis was adopted at this stage as a practical approach.

Figure 3.5: Comparison of the monostatic RCS of unfiltered and filtered LB radiators.

Both models are under identical plane-wave excitation, with the E-field aligned parallel to the HB radiators. To better simulate a realistic resonant dipole, a lumped

port is used in both cases to connect the two LB radiators. A comparison of the scattering results shows that the filtered LB radiator achieves a significant reduction in RCS within the HB frequency range: at least 14.8 dB at 1.4 GHz and up to 30.6 dB at 2.2 GHz. This demonstrates the high-pass performance of the filtered LB radiators. In the LB frequency range, the scattering result of the filtered LB radiators shows a comparable level with the unfiltered LB radiators, confirming the intended low-pass characteristics. Notably, after incorporating the helical filters, the effective LB dipole arm length is reduced from approximately $0.5\lambda_{L_0}$ to $0.26\lambda_{L_0}$.

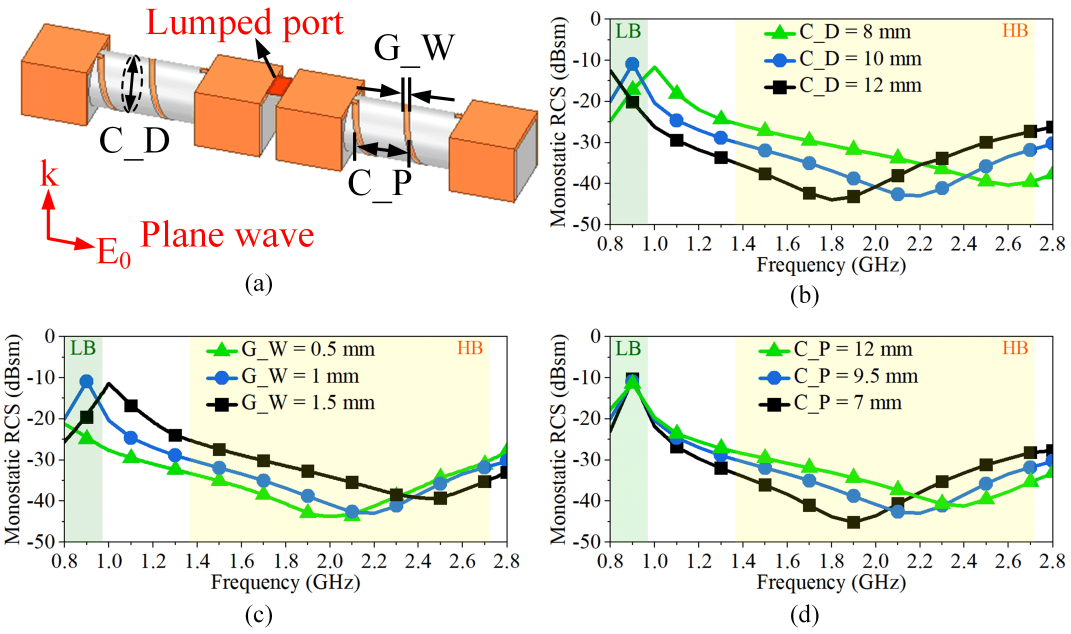

Figure 3.6: Parameter sweep of three key design parameters of the helical filter and their effects on the RCS results. (a) Illustration of the three key parameters. Variation of the monostatic RCS with different values of (b) C_D, (c) G_W, and (d) C_P.

Figure 3.6 illustrates the parameter sweep of three key design parameters of the helical filter and their effects on the RCS results. The three parameters include the diameter of the cylindrical holder C_D, the diameter of the conducting wire G_W, and the distance between neighboring turns C_P. During the parameter sweep, only one parameter is varied while all the other parameters remain fixed with the values given in

Figure 3.4.

As shown in Figure 3.6(b), for the HB, a larger C_D moves the minimum point of the RCS to a lower frequency, corresponding to the parallel resonant point of the helical filter moving to a lower frequency. This is because increasing C_D increases both L and C of the helical filter, consequently decreasing the parallel resonant frequency. Figure 3.6(c) shows a larger G_W shifts the minimum point to a higher frequency, as it reduces L. Figure 3.6(d) shows a larger C_P moves the minimum point to a higher frequency, as it reduces C.

Additionally, the change of these parameters could also affect the low-pass performance in the LB. A larger C_D moves the maximum point to a lower frequency and a larger G_W moves it to a higher frequency. The C_P has a minor impact on the maximum point but could slightly influence the low-pass bandwidth. The final selected values for the three parameters are C_D = 10 mm, G_W = 1 mm, and C_P = 9.5 mm, which ensure that the filtered LB radiators attain the necessary low-pass, high-stop performance in the two target bands.

The filtering ability of the proposed filtered LB radiators is further evaluated within the dual-band embedded array. The configurations of the comparative models are depicted in Figure 3.7, representing the smallest modular unit of the complete array shown in Figure 3.1. In both cases, the LB baluns are removed to focus on the influence of the LB radiators.

Figure 3.7: Simplified dual-band BSA arrays. (a) Case 1: HB antennas with unfiltered LB radiators. (b) Case 2: HB antennas with filtered LB radiators.

Figures 3.8 and 3.9 compare the performance of HB Ant1 and HB Ant2, respectively, in terms of radiation patterns, S-parameters, and realized gain when adjacent to either unfiltered or filtered LB radiators.

Figure 3.8: HB Ant1 performance with unfiltered and filtered LB radiators. (a) Radiation patterns in the yoz-plane for +45° polarization at three sample frequencies. (b) S-parameters. (c) Realized gain for +45° polarization.

In Figure 3.8, the presence of unfiltered LB radiators significantly degrades the performance of HB Ant1. This degradation manifests as distorted radiation patterns, reduced HPBW stability, and increased cross-polarization levels. Additionally, the reflection coefficient deteriorates notably at lower HB frequencies, resulting in a constrained operational bandwidth and a realized gain as low as 1.14 dBi at 1.86 GHz.

In contrast, when filtered LB radiators are employed, HB Ant1 demonstrates sub-

stantial improvements. The radiation patterns become more stable with reduced cross-polarization, as shown in Figure 3.8(a). Meanwhile, the reflection coefficient is effectively restored, accompanied by a 6.66 dB increase in port isolation, illustrated in Figure 3.8(b). In addition, the realized gain remains consistently above 6.75 dBi across the entire frequency band, as depicted in Figure 3.8(c).

Figure 3.9: HB Ant2 performance with unfiltered and filtered LB radiators. (a) Radiation patterns in the yoz-plane for +45° polarization at three sample frequencies. (b) S-parameters. (c) Realized gain for +45° polarization.

A comparison of the results in Figure 3.9 with those in Figure 3.8 reveals that HB Ant2 experiences less performance degradation than HB Ant1. This is primarily due to its greater distance from the LB radiators, which reduces the shielding effect. However, the integration of filtered LB radiators still notably enhances HB Ant2's performance.

Specifically, cross-polarization levels are further reduced, port isolation improves by over 9 dB, and the realized gain increases by 1.55 dB, as demonstrated in Figure 3.9(a), (b), and (c), respectively. These results highlight the advantages of using filtered LB radiators in embedded dual-band arrays.

3.3.2 Modified Balun for Impedance Matching and Gain Enhancement

The LB balun plays a crucial role in this design, as it must both ensure appropriate impedance matching despite the presence of helical filters and minimize its impact on the HB antenna in the dual-band array. In this configuration, the LB baluns surround the HB antenna, which can degrade the HB performance. To mitigate this, a microstrip balun with LC series loading is introduced, utilizing meander lines as inductors and overlapped patches as capacitors, as shown in Figure 3.4(d).

Figure 3.10: Comparison of the LB antenna input impedances over 0.82–0.96 GHz when fed by Balun1 and Balun2.

Figure 3.10 compares the input impedances of LB radiators fed by the balun without LC loading (Balun1) and the one with LC loading (Balun2). For simplicity, ideal lumped ports are used, and the inner feeding lines are omitted. The Smith chart is normalized

to 150–200jΩ to shift the impedance loci toward the center, facilitating observation. As shown, adding LC series structures concentrates the impedance locus, particularly in the lower frequency range, improving better matching. Furthermore, it introduces a new resonance that broadens the overall bandwidth. Subsequent fine-tuning of the feeding line transforms this impedance to the required 50 Ω.

Figure 3.11: (a) HB Ant1 realized gains in four cases. (b) Current distributions at 1.5 GHz on Balun1 and Balun2 when HB Ant1 is excited.

What should be noted is that the four surrounding LB baluns affect the radiation of HB Ant1 in the dual-band array configuration. As shown in Figure 3.11(a), two noticeable gain drops around 1.5 GHz and 2.2 GHz appeared after adding the four LB baluns. Adding baffles helps improve gain in the 1.7-2.7 GHz range, but they are ineffective at lower frequencies. Incorporating LC circuits into the LB baluns addresses this issue, increasing the realized gain at low frequencies. For instance, the realized gain at 1.5 GHz is raised from 5.67 dBi to 7.95 dBi. This effect is further clarified by comparing the current distributions on Balun 1 and Balun 2, as depicted in Figure 3.11(b). As shown, at 1.5 GHz, the LC-loaded balun suppresses induced currents on the main balun body. While significant induced currents remain in the meander line section, opposing currents

along adjacent meander paths cancel each other's far-field contributions, effectively reducing the overall impact on the HB antenna.

3.4 Dual-Band BSA Array

3.4.1 Simulated and Measured Results

A 1L3H array prototype, consisting of one LB and three HB antennas, was constructed to validate the filtering technique.

Figure 3.12: (a) The fabricated 1L3H array prototype. (b) Port numbering of the 1L3H array.

As shown in Figure 3.12(a), one HB antenna is housed inside the LB cavity, while the other two are placed externally. The HB element spacing is 140 mm. Figure 3.12(b) presents the assembled prototype. The T-shaped dielectric supports of the LB antenna

were 3D-printed using ABS-M30 ($\varepsilon_r = 2.6$), while the U-shaped enclosures were fashioned from aluminum and tin-plated for soldering. Helical filters were formed by winding copper wires onto designated grooves in the dielectric supports, with junctions soldered for stable electrical contact. Two commercial power dividers were incorporated to feed the LB antenna.

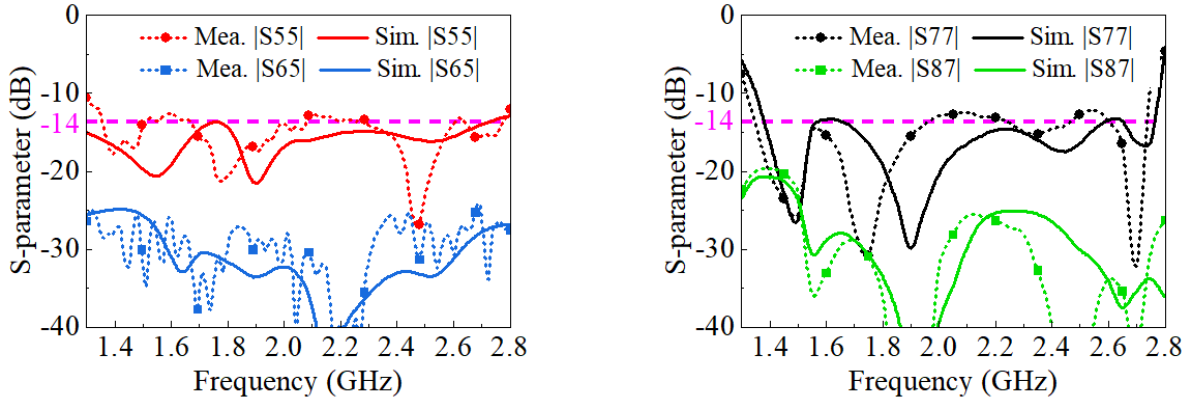

(a) (b)

Figure 3.13: Simulated and measured S-parameters of (a) HB Ant1 and (b) HB Ant2 in the 1L3H array.

Figure 3.13 compares the simulated and measured S-parameters of HB Ant1 and HB Ant2 in the 1L3H array. The measured reflection coefficients are mostly below -14 dB, with some values around -12.6 dB across the 1.36-2.72 GHz range (66.7%). The port isolation remains above 20 dB.

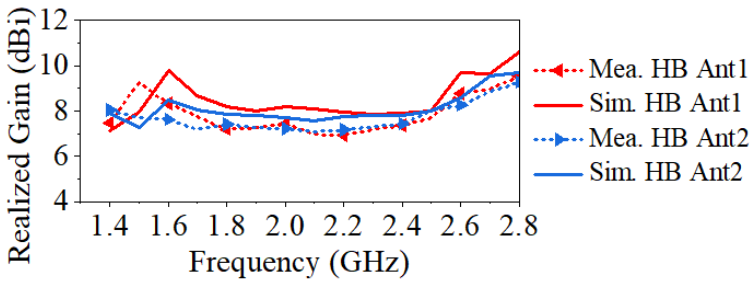

Figure 3.14: Simulated and measured realized gain of the HB antennas in the 1L3H array for +45° polarization.

Figure 3.15: Simulated and measured yoz-plane radiation patterns at five frequencies for (a) HB Ant1 and (b) HB Ant2 in the 1L3H array for +45° polarization.

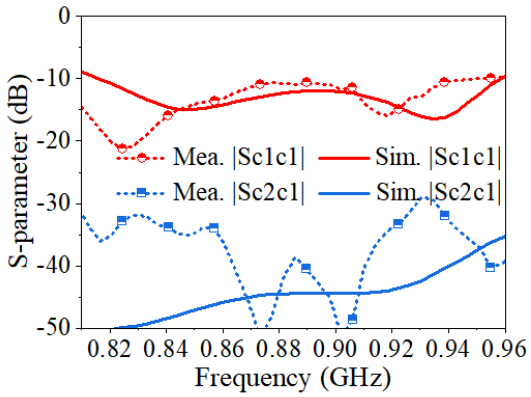

(a)

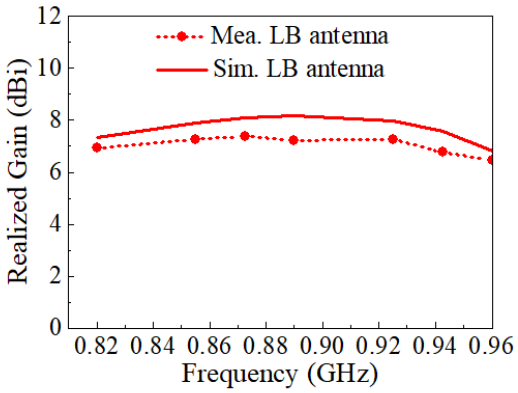

(b)

(c)

Figure 3.16: Simulated and measured LB antenna performance in the 1L3H array. (a) S-parameters. (b) Realized gain for +45° polarization. (c) Radiation patterns at 0.82 GHz, 0.89 GHz, and 0.96 GHz in the yoz-plane for +45° polarization.

Figure 3.14 shows the measured realized gains, ranging from 6.95 dBi to 9.25 dBi for HB Ant1 and 7.10 dBi to 8.86 dBi for HB Ant2. HB Ant1 has a slightly higher gain, possibly due to the LB baluns forming a partially open cavity that concentrates the radiated fields.

Figures 3.15(a) and (b) show strong agreement between the simulated and measured radiation patterns of HB Ant1 and HB Ant2. For HB Ant1, the measured half-power beamwidth (HPBW) remains within $65° \pm 22°$, with a boresight cross-polarization discrimination (XPD) surpassing 16.08 dB. For HB Ant2, the HPBW is $68.5° \pm 12.5°$, and the boresight XPD exceeds 20.49 dB.

Figure 3.16 presents the LB antenna's performance in the 1L3H array. The measured reflection coefficient remains below -10 dB in 0.8-0.96 GHz (17.1%), while port isolation exceeds 28.91 dB, as shown in Figure 3.16(a). For the +45°polarization, the realized gain ranges from 6.47 dBi to 7.38 dBi, as depicted in Figure 3.16(b). Notably, the LB antenna maintains a realized gain below -19.78 dBi over the HB band from 1.36 to 2.72 GHz, confirming its effective filtering functionality. The radiation patterns exhibit stable HPBWs of $59.5° \pm 9°$, with XPD values exceeding 16.03 dB at boresight, as illustrated in Figure 3.16(c). The results for the -45°polarization show a similar trend and are therefore omitted.

Figure 3.17 shows the cross-band coupling coefficients between the proposed LB antenna, HB Ant1, and HB Ant2. In Figure 3.17(a) and (b), the measured transmission coefficients between the LB and HB antennas remain below -25.32 dB in the LB and below -19.03 dB in the HB. The measured transmission coefficients between HB antennas are below -19.29 dB, as shown in Figure 3.17(c).

Figure 3.17: Simulated and measured transmission coefficients in the 1L3H array: (a) between HB and LB antennas in the LB band, (b) between HB and LB antennas in the HB band, (c) between HB antennas in the HB band.

3.4.2 Comparison and Discussion

Table 3.1 compares the proposed structure with previously reported cross-band designs, listed by increasing HB bandwidth. The LB antenna presented herein supports an unprecedented HB bandwidth of 66.7% (1.36–2.72 GHz).

Table 3.1: Comparison with Published Cross-Band Array Designs

Refs	De-scattering Measures	LB Antenna Bandwidth (GHz)	HB Antenna Bandwidth (GHz)	LB Aperture Size ($\lambda_{L_0} \times \lambda_{L_0}$)
[30]	Back cavity array scheme	0.69–0.96 (32.7%)	3.30–3.80 (14.1%)	0.50×0.50
[21]	Embedded scheme	0.82–0.96 (15.7%)	1.71–2.17 (23.7%)	0.50×0.50
[1]	Chokes	0.82–1.00 (19.8%)	1.71–2.28 (28.6%)	0.42×0.42
[26]	Stacked array scheme	0.69–0.96 (32.7%)	3.50–4.90 (33.3%)	0.69×0.69
[7]	Etched slots	0.69–0.96 (32.7%)	1.70–2.40 (34.2%)	0.42×0.42
[81]	Partially Reflecting Surfaces	0.68–0.96 (34.2%)	1.71–2.69 (44.6%)	0.43×0.43
This work	Helical filters	0.80–0.96 (18.2%)	1.36–2.72 (66.7%)	0.38×0.38

λ_{L_0} denotes the wavelength at the LB center frequency.

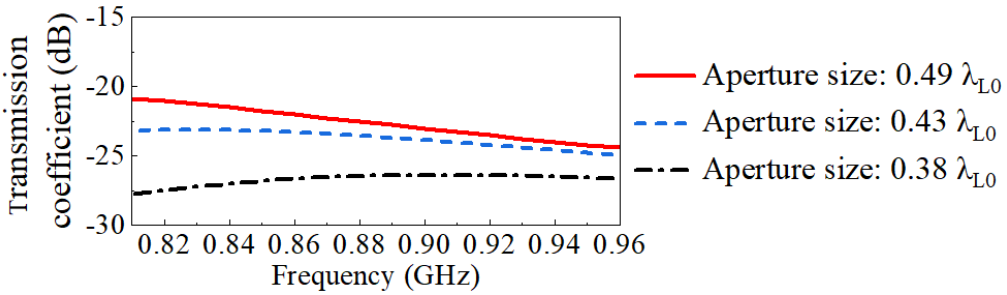

Figure 3.18: +45°-polarized in-band isolation between adjacent LB antennas at a fixed element spacing of 280 mm ($0.83\lambda_{L_0}$) for different aperture sizes.

The helical filters extends the current path on the LB radiators, thereby effectively reducing the LB aperture to about $0.38\lambda_{L_0} \times 0.38\lambda_{L_0}$. As illustrated in Figure 3.18, a

smaller aperture can improve in-band isolation for given element spacings. Notably, achieving both enhanced scattering suppression and a reduced aperture comes with trade-offs, including a narrower LB impedance matching bandwidth and increased structural complexity.

3.5 Conclusion

This work presents a dual-band shared-aperture array based on an embedded scheme, achieving wideband cross-band scattering suppression. By incorporating innovative helical filters into the LB antenna, the adverse scattering interference of closely positioned LB antennas on HB antennas is effectively mitigated over a wide frequency range of 1.36-2.72 GHz (66.7%). Despite the matching challenges introduced by the helical filters, the LB antenna achieves reliable impedance matching within the 0.8-0.96 GHz band (17%) through integrating specially designed LC series circuits in the LB baluns. Additionally, the extended current paths enabled by the helical filters allow for a compact LB aperture, resulting in improved in-band isolation within the array. The consistency between simulated and measured results of the fabricated array confirms the effectiveness of this design approach.

CHAPTER 4

MULTI-BAND SHARED-APERTURE ANTENNA ARRAY BASED ON A NEW BUFFERING SCHEME

This chapter proposes a shared-aperture dual-band array based on a newly developed buffering scheme. Unlike conventional shared-aperture array schemes, such as the embedded scheme presented in Chapter 3, which primarily aim to minimize coupling between LB and HB antennas to mitigate cross-band interference, this design strategically leverages structural coupling to enhance overall performance. This buffering-scheme-based array introduces a unique tightly coupled buffering layer (TCBL) that is strongly coupled with both the LB and HB radiators, offering three key benefits: (1) it significantly reduces the profile of the LB antenna while maintaining wideband bandwidth, (2) it enhances the bandwidth of the HB antenna from 45.5% to 59.0%, and (3) it acts as an "electromagnetic buffer", capturing coupled energy and preventing its transmission to cross-band ports, effectively suppressing cross-band interference. By leveraging this innovative scheme, the developed dual-band array achieves stable radiation performance across 0.69-0.96 GHz (32.7%) for the LB and 1.47-2.7 GHz (59.0%) for the HB, while maintaining a ultra-low profile of only $0.087\lambda_L$ (λ_L is the wavelength at the lowest LB

frequency) and inherently suppressing cross-band coupling and scattering. The proposed buffering scheme eliminates the need for additional filtering or frequency-selective structures, offering a more compact and efficient array solution for dual-band operation.

4.1 Introduction

In multi-band antenna arrays, the close spacing between antennas operating at different frequency bands often results in significant cross-band scattering and coupling interferences. To mitigate these effects, various methods have been proposed, typically implemented through several typical array schemes. Their schematic typologies are illustrated in Figure 4.1.

In the commonly used interleaved scheme, illustrated in Figure 4.1(a), LB and HB antennas share a common ground, where the HB antennas naturally reside in the shadows of the larger LB antennas. This arrangement obstructs HB radiation and introduces significant cross-band scattering interference, leading to degraded HB radiation performance [2]. To mitigate this issue, LB antennas are usually modified to be 'electromagnetically invisible' at HB frequencies using various techniques, including chokes [1, 3–5], etched slots [6–9], U-/L-shaped structures [10–12], 2.5-D cloaks [13], absorbing metasurfaces with bandstop characteristics [14, 15], and filter-based arms paired with frequency-selective surfaces (FSSs) [16, 17], split-ring resonators (SRRs) [18], or metasurfaces [19]. Although these methods effectively reduce LB-induced interference on HB antennas, they often compromise LB antenna performance or complicate LB impedance matching [13].

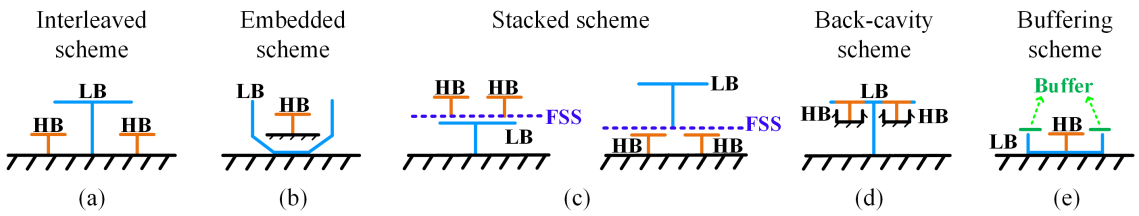

Figure 4.1: Typologies of different dual-band shared-aperture array schemes. (a) Interleaved scheme. (b) Embedded scheme. (c) Stacked scheme. (d) Back-cavity scheme. (e) Buffering scheme proposed in this work.

Another commonly used array scheme is the embedded scheme, shown in Figure 4.1(b), where an HB antenna is positioned within a bowl-shaped LB antenna. The hollow-cubed structure of the LB antenna reduces its blockage effects on the HB antenna compared to the interleaved scheme. However, it does not completely eliminate cross-band interference, often necessitating additional solutions such as customized baffles or increasing the height of HB antennas, which adds structural complexity [20–24]. Alternative approaches include lowering the height of LB antennas or using filtering LB antennas introduced in Chapter 3 [82, 83]. However, this makes it more challenging to achieve a wide LB bandwidth, restricting it to approximately 18.7% (0.82-0.99 GHz) [82] or 18.2% (0.80-0.96 GHz) [83].

The stacked scheme [25–29] and the cavity-backed scheme [30, 31], illustrated in Figure 4.1(c) and Figure 4.1(d), respectively, offer alternative solutions. In the stacked scheme, HB antennas are placed above [25–27] or below LB antennas [28, 29], with FSSs in between to isolate LB and HB antennas. In the cavity-backed scheme, HB antennas are raised to the LB aperture level, and backed cavities act as HB reflectors, ensuring unobstructed radiation. While both schemes reduce cross-band interference, adjusting HB or LB antenna heights and integrating FSSs or back cavities add complexity and cost.

This work presents a novel buffering scheme for dual-band shared-aperture arrays for the first time. The key innovation lies in the unique buffer TCBL, shown in Fig-

ure 4.1(e), which enables an ultra-low-profile configuration while enhancing dual-band impedance matching performance and inherently suppressing cross-band interference. The developed buffering-scheme-based array covers a wide dual-band range, spanning 0.69-0.96 GHz (32.7%) in the LB and 1.47-2.7 GHz (59.0%) in the HB. Compared to previous shared-aperture array schemes, the buffering scheme operates differently and offers the following key advantages:

1. It attains a more compact structure with an ultra-low profile of $0.087\lambda_L$ (where λ_L is the wavelength at the lowest frequency of the LB, 0.69 GHz);

2. It avoids performance degradations in either band and further improves impedance matching performance for both bands;

3. It inherently suppresses cross-band interference without resorting to de-scattering or decoupling measures typically used in other array schemes.

This design can be readily extended to future multi-band shared-aperture BSA configurations.

The remainder of this chapter is organized as follows. Section 4.2 presents the low-profile wideband LB antenna design and analyzes its evolution process showing how such a low profile is achieved. Section 4.3 discusses the HB antenna configuration, detailing performance improvements when coupled with the TCBL. Section 4.4 focuses on the buffering-scheme-based shared-aperture array and its inherent ability to suppress cross-band interference. Section 4.6 provides fabrication and measurement results, along with comparisons to leading-edge shared-aperture arrays.

4.2 Low-Profile Wideband LB Antenna

Standard-height LB antennas often block adjacent HB antennas, degrading their performance. Reducing the LB profile mitigates this issue but deteriorates impedance matching. To address this, we introduce a novel TCBL and four shorting strips. This section outlines the evolution toward the final low-profile wideband LB antenna by analyzing the input impedance of five models. Figure 4.2 illustrates this evolution. The initial design (Model 1) uses a conventional standard-height bowl-shaped structure consisting of four identical sub-dipoles that form a hollow-cubed assembly [20]. For analytical simplicity, each of the four sub-dipoles is excited by a lumped port located at a corner (see Figure 4.2(a)).

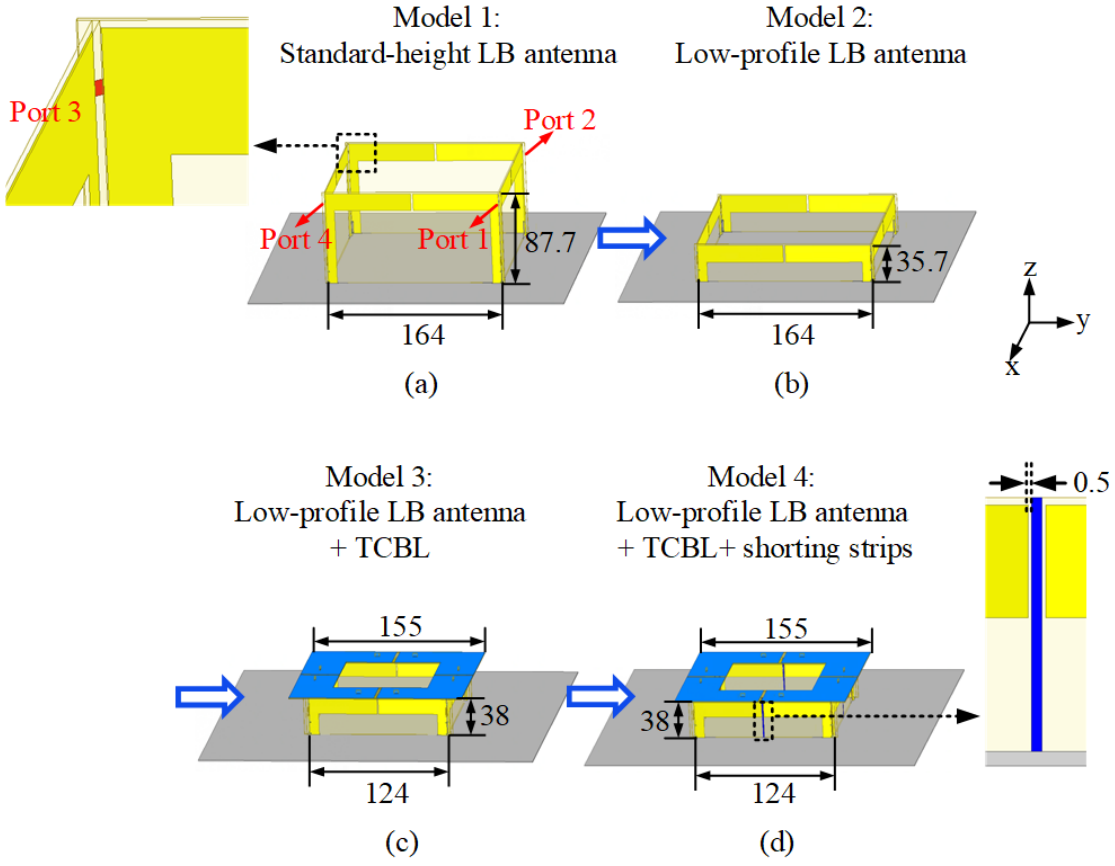

Figure 4.2: Evolution process of the proposed low-profile wideband LB antenna with key geometries. (a) Model 1. (b) Model 2. (c) Model 3. (d) Model 4. (Unit: mm).

Ports 1 and 3 are driven in-phase and equal-amplitude for +45° polarization, creating a combined port c_1, while ports 2 and 4 similarly form port c_2 for −45° polarization. We then calculate the S-parameters of the combined ports by applying the four-port single-ended network transformations [84]:

$$S_{c1c1} = 0.5 \times (S_{11} + S_{13} + S_{31} + S_{33}) \tag{4.1}$$

$$S_{c2c2} = 0.5 \times (S_{22} + S_{24} + S_{42} + S_{44}) \tag{4.2}$$

where S_{ij} indicates the scattering parameter between ports i and j. These equations incorporate mutual coupling and allow an evaluation of the S-parameters for the combined ports without any external power-divider network.

4.2.1 Evolution from Standard-Height to Reduced-Profile Model

Figure 4.3(a) displays the input impedance traces on the Smith chart for each intermediate model shown in Figure 4.2, while Figure 4.3(b) shows the corresponding reflection coefficients.

Model 1 has a profile of $0.24\lambda_0$, where λ_0 is the wavelength at the LB center frequency of 0.82 GHz. Its impedance locus, as shown in in Figure 4.3(a), moves clockwise from low to high frequencies, crossing the Smith chart's real axis once at approximately 0.83 GHz. Consequently, Model 1 has only a single resonance and is inherently bandwidth-limited, which could be obviously observed in in Figure 4.3(b).

Model 2 is realized simply by directly reducing the height to $0.098\lambda_0$. However, this height reduction introduces significant inductive reactance [26], shifting the impedance locus into the upper edge of the inductive region on the Smith chart. This results in severely worsened matching, as seen in Figure 4.3(b).

To mitigate the newly introduced inductance, a TCBL is added, creating **Model 3**. The TCBL is printed on the top layer of the horizontal substrate, separated from the LB

dipole arms by a small gap equal to the substrate thickness, enabling strong capacitive coupling. This added capacitance offsets the strong inductive reactance at low frequencies, bringing the impedance locus closer to the center of the Smith chart. Additionally, a new resonance at about 0.71 GHz is introduced, further enhancing the overall bandwidth, as shown in Figure 4.3(b). Notably, the aperture size of Model 3 is reduced to 155 mm, compared to 164 mm in Model 2.

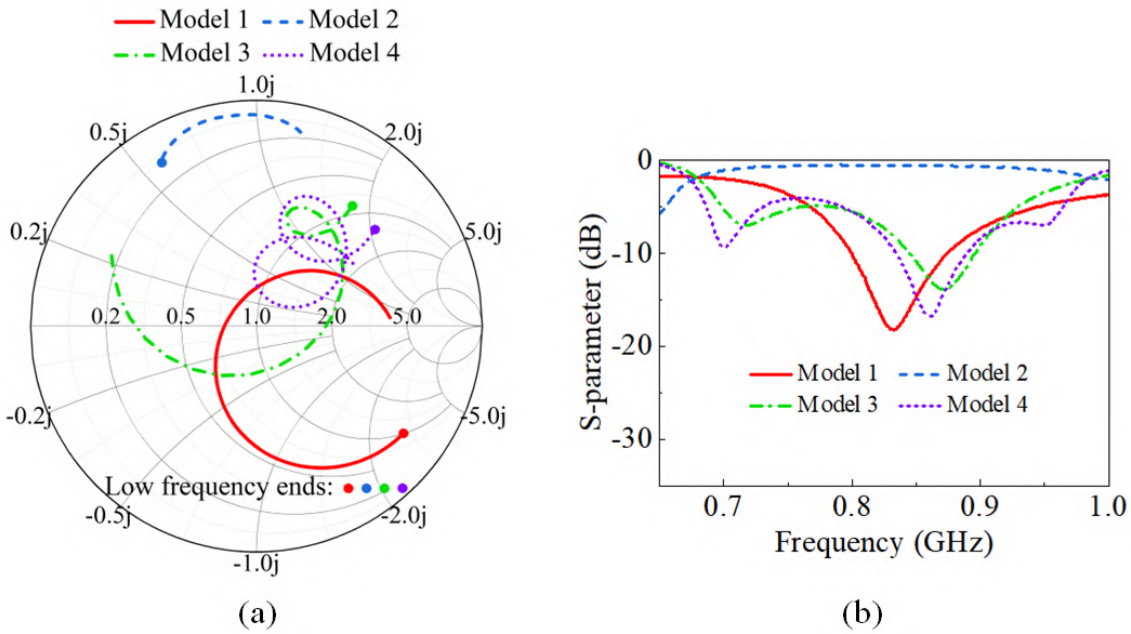

Figure 4.3: Comparison of port c1 input impedances for Models 1–4 in Figure 4.2. (a) Input impedance on the Smith chart over 0.69–0.96 GHz (normalized to 50 Ω). (b) Reflection coefficients.

To enhance high-frequency impedance matching, **Model 4** incorporates four shorting strips. Each strip is positioned between two adjacent sub-dipoles while maintaining a small gap from the dipole arms. These strips generate additional resonance modes, which help refine the impedance locus at the high-frequency range. As a result, Model 4 achieves a third resonance at approximately 0.95 GHz, as shown in Figure 4.3(b).

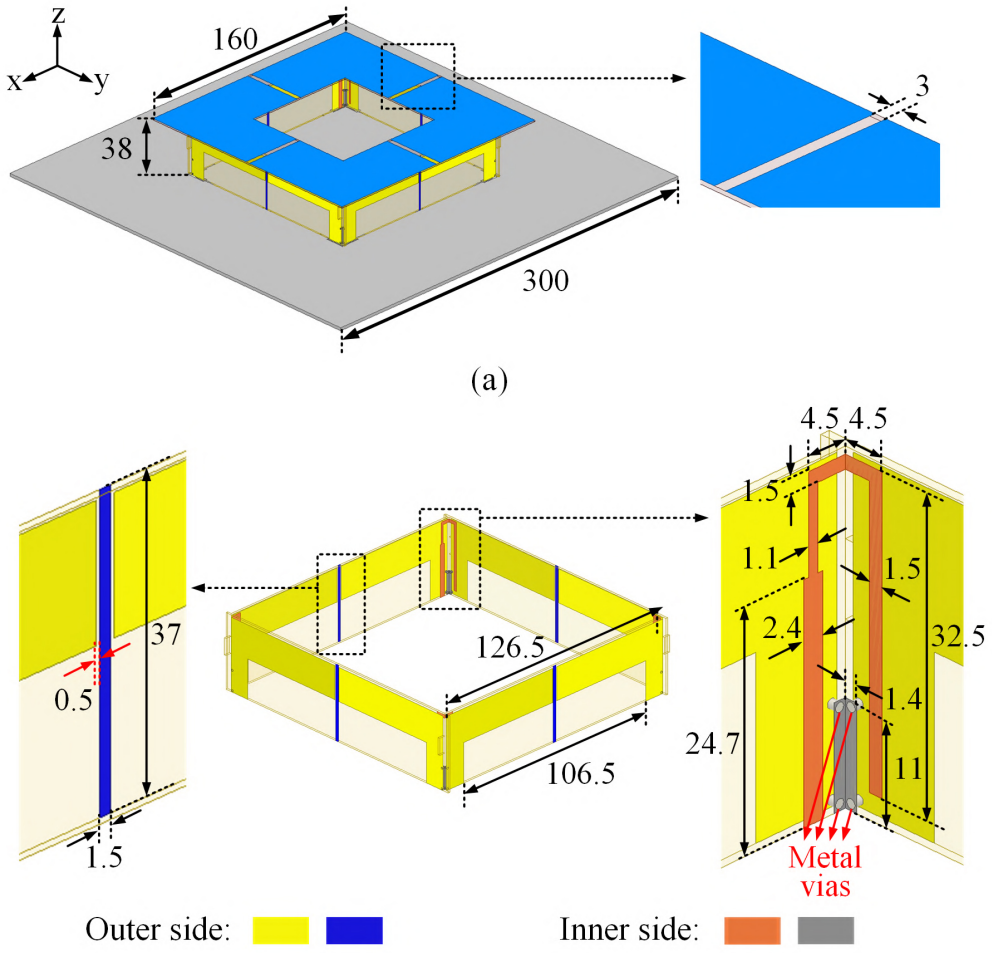

Figure 4.4: Model 5: Model 4 with feeding baluns. (a) Full configuration with zoomed-in details. (b) Hollow-cubed dipoles (enlarged). (Unit: mm).

The input impedance results of Models 1-4 are obtained without baluns to eliminate their influence when evaluating the impedance matching capabilities of the different designs. In **Model 5**, baluns are added to each sub-dipole of Model 4. The detailed geometry of Model 5 is presented in Figure 4.4. The substrates supporting the LB dipoles and the TCBL are made from Taconic RF-35, with a relative permittivity ε_r of 3.5, a loss tangent $\tan\delta$ of 0.0018, and a thickness of 1.016 mm.

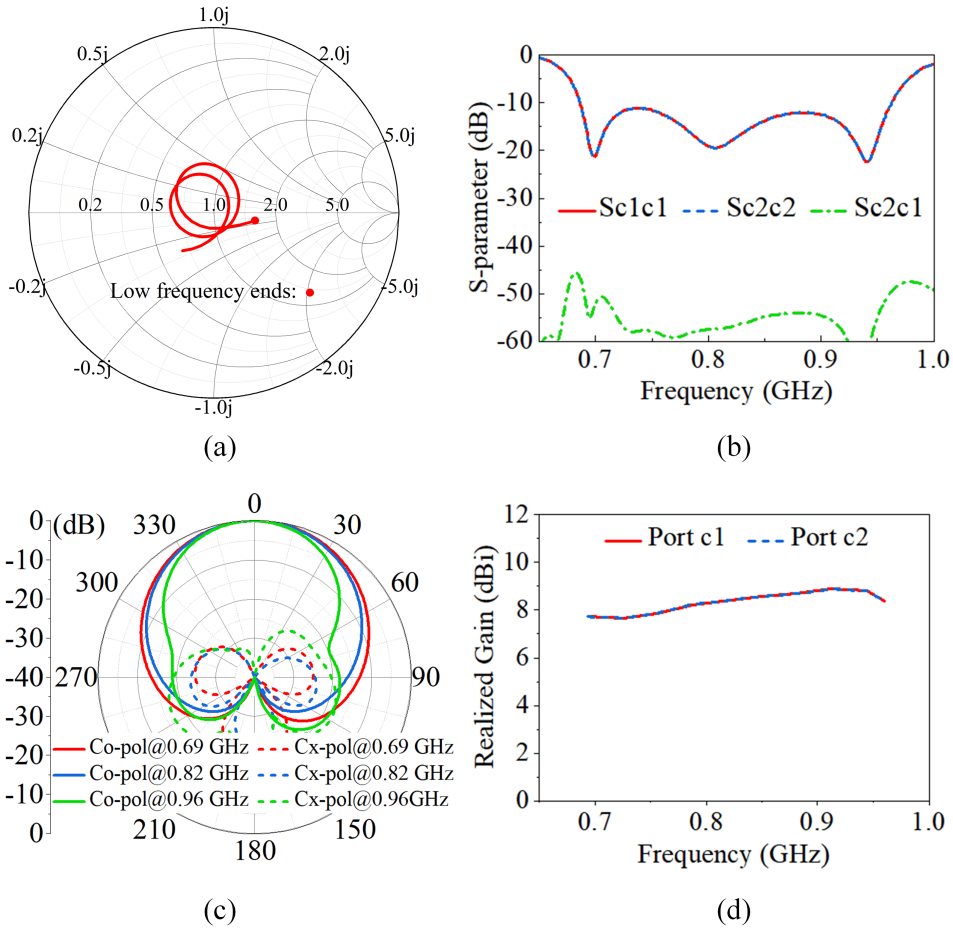

Figure 4.5: Performance of Model 5. (a) Input impedance on the Smith chart over 0.69–0.96 GHz (normalized to 50 Ω). (b) S-parameters. (c) Radiation patterns (port c1) in the yoz-plane. (d) Realized gain across the LB band.

The performance of Model 5 is illustrated in Figure 4.5. The impedance locus and reflection coefficient, shown in Figure 4.5(a) and (b), demonstrate successful impedance matching within the frequency range of 0.69-0.96 GHz for both ±45° polarizations. Exceptional port isolation of exceeding 51.2 dB is achieved, as displayed in Figure 4.5(b). Notably, the TCBL plays a crucial role in enabling this LB antenna to achieve a wide bandwidth with a significantly reduced profile. As shown in Figure 4.5(c), the antenna maintains stable radiation patterns with XPD greater than 45.1 dB at the boresight. Additionally, the realized gain ranges from 7.7 to 8.9 dBi across the operating bandwidth,

as depicted in Figure 4.5(d).

4.3 HB Antenna

4.3.1 HB Antenna Alone

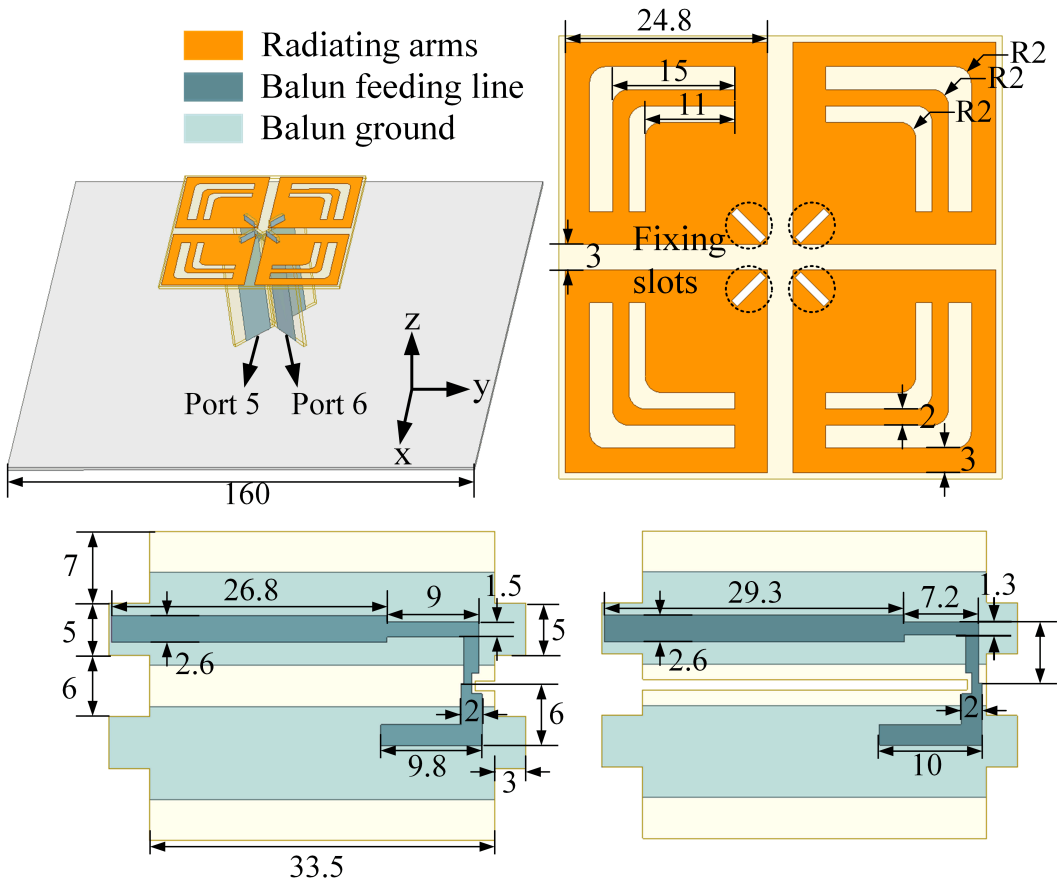

Figure 4.6: HB antenna design. (Unit: mm).

Figure 4.6 illustrates the structure of the HB antenna. The design adopts a conventional cross-dipole configuration, comprising two sub-dipoles oriented perpendicularly for ±45° dual-polarized radiation [85]. Each radiator and balun is fabricated on a Taconic RF-35 substrate, which has a relative permittivity of $\varepsilon_r = 3.5$, a loss tangent $\tan\delta = 0.0018$, and a thickness of 1.016 mm.

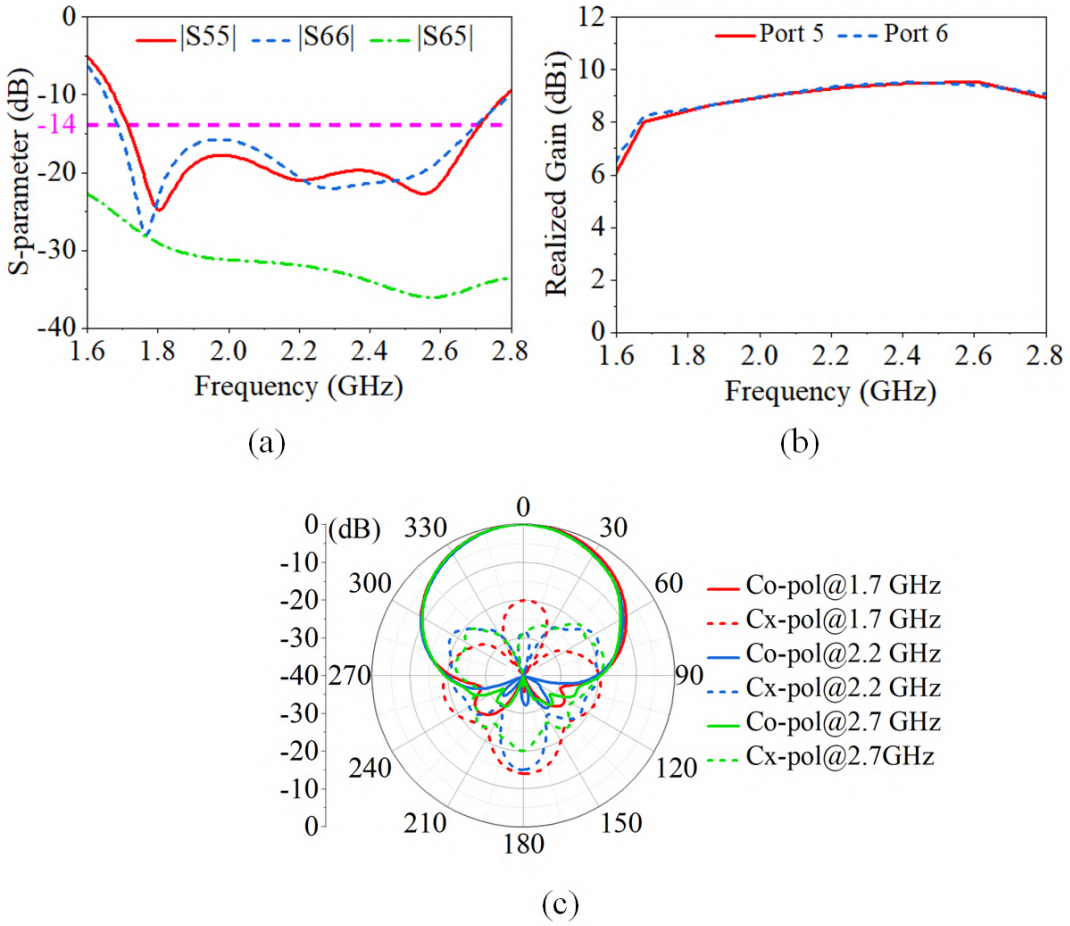

Figure 4.7: Performance of HB antenna alone. (a) S parameters. (b) Realized gain. (c) Radiation patterns for port 5 in the yoz-plane.

Figure 4.7(a)–7(c) present the simulated S-parameters, realized gains, and radiation patterns, respectively, of the proposed HB antenna. Owing to the symmetrical structure of the design, the radiation patterns for port 6 closely resemble those of port 5, and thus the port 6 patterns are omitted for brevity. As depicted in Figure 4.7(a), the reflection coefficients stay below -14 dB across the 1.7-2.7 GHz frequency range (45.5%), with port isolation exceeding 26.4 dB in the same band. Figure 4.7(b) shows that the realized gain varies from 8.1 dBi to 9.3 dBi for both port 5 and port 6 throughout the operating band. Furthermore, from Figure 4.7(c), it can be seen that the radiation patterns exhibit minimal variation over the entire bandwidth. The XPD is greater than 20.3 dB in the

boresight direction and stays above 9.5 dB for angles within $-60° < \theta < 60°$.

4.3.2 HB Antenna with TCBL

The HB antenna is meant to be placed inside the LB antenna to maximize space utilization efficiency. In such shared-aperture configurations, it is typically expected that the LB antenna will deteriorate the performance of the HB antenna [21, 22, 24, 83], especially given the wide operating bandwidth of the HB antenna. In [83], wide-band filters had to be inserted into the LB radiators to ensure they were electromagnetically invisible to the HB element. This not only increased fabrication difficulty but also reduced the bandwidth of the LB antenna. In contrast, no additional filtering is needed in this work because, rather than degrading the HB antenna's performance, the TCBL introduces a new resonant mode that further expands the HB bandwidth from 45.5% to 59.0%.

To investigate this improvement more thoroughly, the HB antenna is examined under three different scenarios, as illustrated in Figure 4.8:

- Case A: HB antenna alone
- Case B: HB antenna + TCBL
- Case C: HB antenna + TCBL + LB antenna

Figure 4.8(a) shows that the stand-alone HB antenna (Case A) exhibits resonances at approximately 1.8 GHz, 2.2 GHz, and 2.55 GHz, labeled R_{A1}, R_{A2}, and R_{A3}.When the TCBL is introduced in Case B, additional capacitive coupling is added, enhancing impedance matching at lower frequencies. This modification gives rise to a new resonance, R_{B0}, at 1.5 GHz, effectively extending the HB bandwidth from 45.5% (1.7-2.7 GHz) to 60.2% (1.45-2.7 GHz). Meanwhile, R_{A1} shifts to R_{B1} at 1.7 GHz, and R_{A2} moves to R_{B2} at 2.0 GHz. The third resonance, R_{B3}, remains nearly unchanged from R_{A3} due to weaker coupling at higher frequencies. Notably, in Case C, the inclusion of the LB dipoles does

not negate the bandwidth enhancement. Instead, the HB bandwidth under Case C still achieves 1.47–2.7 GHz (59.0%), with a reflection coefficient lower than −14 dB, which is broader than the initial stand-alone scenario (Case A).

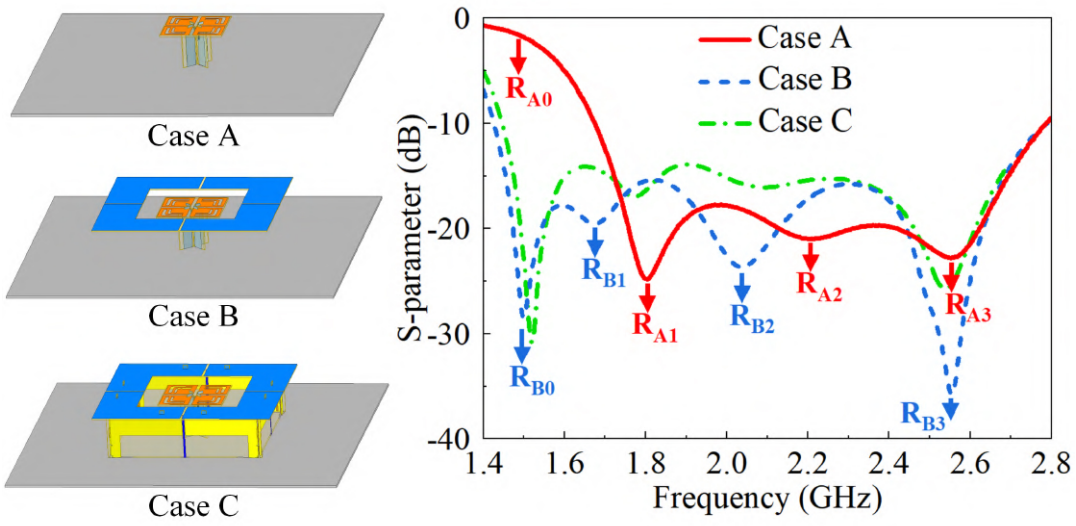

Figure 4.8: Comparison of $|S_{55}|$ of the HB antenna in three cases: Case A: HB antenna alone; Case B: HB antenna + TCBL; Case C: HB antenna + TCBL + LB antenna.

To clarify the reason behind this bandwidth enhancement, Figure 4.9 compares the current distributions at resonances R_{A0}–R_{A3} in Case A to R_{B0}–R_{B3} in Case B, using arrows to indicate the direction of current flow. At 1.5 GHz, the HB antenna in Case A has an aperture size of only 0.26 × 0.26 wavelengths, which limits the current paths and restricts efficient radiation. In contrast, Case B at this frequency exhibits significantly extended coupled currents on the TCBL. These currents on the TCBL, which are more pronounced than the currents on the HB aperture, form an effective resonance mode at 1.5 GHz. For the other three resonances, the current distributions on the HB radiators in both Case A and Case B remain similar, with minimal induced currents observed on the TCBL. Consequently, the TCBL contributes a newly generated resonance mode, while leaving the original resonant states of the HB antenna largely unaffected.

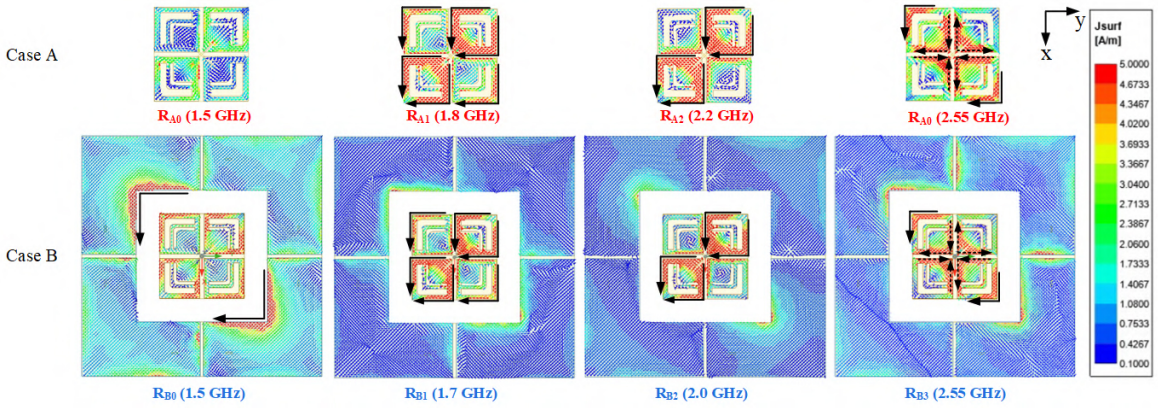

Figure 4.9: Current distributions on the TCBL and HB radiators in Case A at R_{A0}-R_{A3} and in Case B at R_{B0}-R_{B3} when port 5 is excited (-45°polarization).

4.4 Shared-Aperture Dual-Band Antenna Array

Controlling cross-band scattering and coupling is critical for shared-aperture arrays, as they directly affect radiation patterns and port isolation. The proposed buffering-scheme-based array incorporates the novel TCBL, which not only enables a compact low-profile configuration but also functions as an "electromagnetic buffer" to suppress cross-band interference. This section explores how the TCBL minimizes unwanted scattering and coupling, with Part A and Part B demonstrating its respective impact, and how it contributes to overall array performance.

Figure 4.10 shows the final structure of the buffering-scheme-based shared-aperture antenna array. To reduce the gain variation observed in the HB antenna when it is placed in the array environment, additional side reflectors are incorporated between the HB and LB antennas. These side reflectors follow a conventional approach widely adopted in array optimization [20, 22, 23, 82]. Various slots and protruding blocks are strategically incorporated on the dielectric substrates and ground plane to form reliable mechanical and electrical connections across different parts of the overall structure.

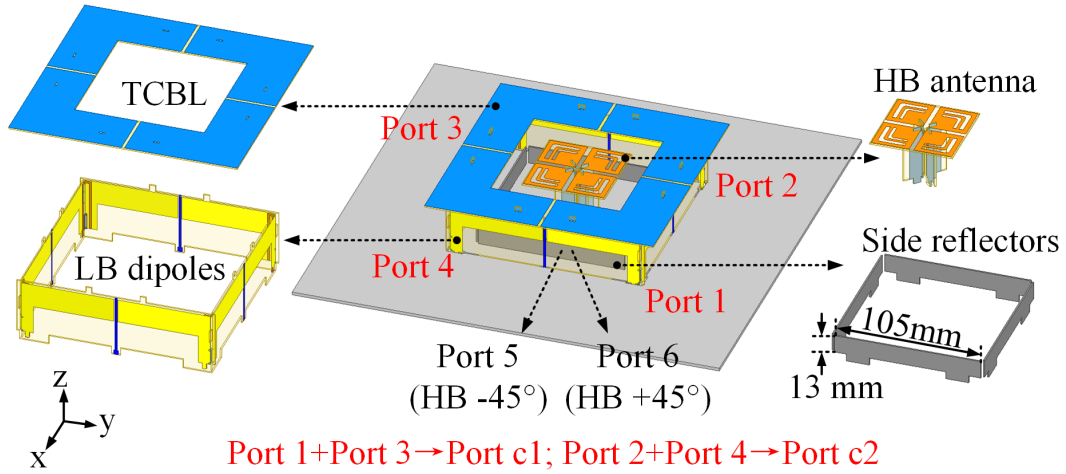

Figure 4.10: Final configuration of the shared-aperture dual-band antenna array. (Unit: mm).

4.4.1 Mitigated Cross-Band Scattering

In conventional dual-band array arrangements such as those shown in Figure 4.1(a) and (b), the HB antennas are often placed under the LB antennas. Consequently, the HB radiation is blocked and scattered by the overlying LB antennas, causing significant pattern distortion. To alleviate this distortion, LB antennas are often redesigned with filtering properties so that they become electromagnetically transparent in the HB [2]. By contrast, the LB antenna in the proposed buffering scheme has a height similar to that of the HB antenna, significantly reducing its blockage of the HB radiation. This is investigated by comparing the HB antenna's radiation performance in four different scenarios, as shown in Figure 4.11:

- Scenario 1: HB antenna alone
- Scenario 2: HB antenna with a standard-height LB antenna
- Scenario 3: HB antenna in the proposed buffering scheme
- Scenario 4: HB antenna in the buffering scheme with side reflectors

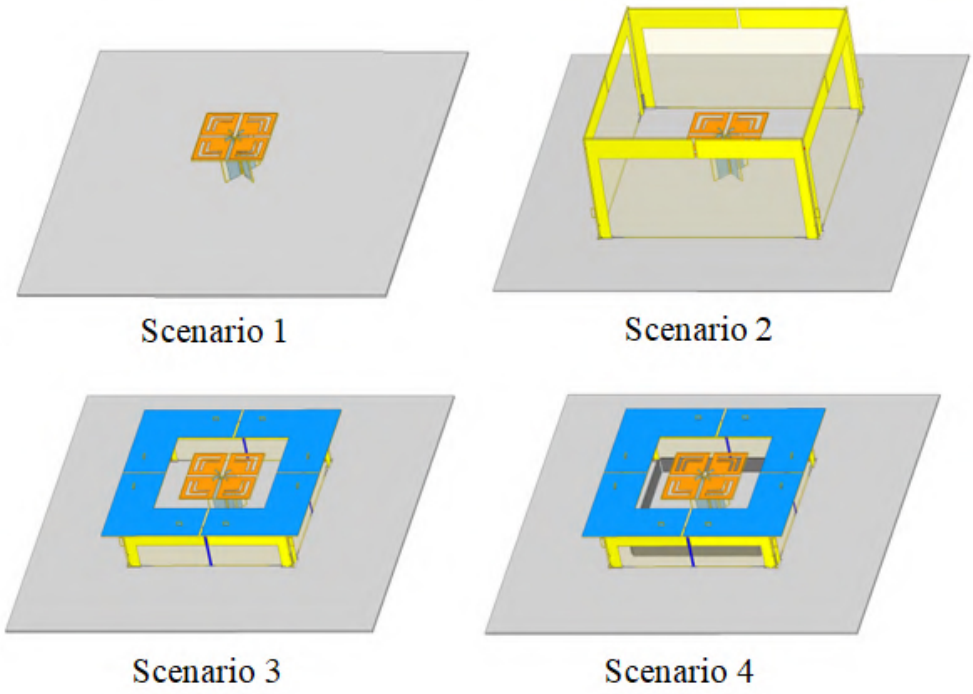

Figure 4.11: Four scenarios for evaluating HB scattering.

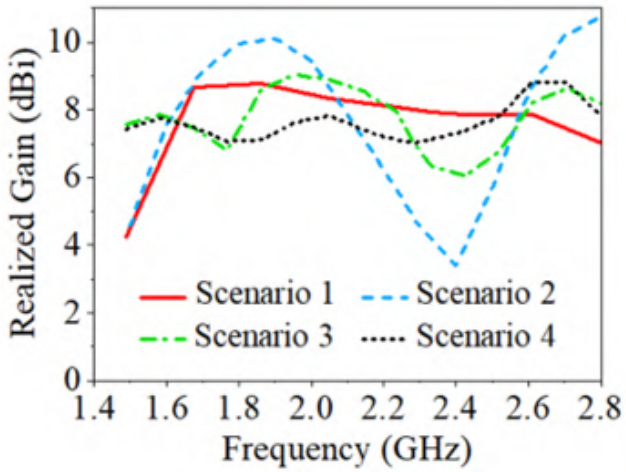

Figure 4.12: Comparison of HB realized gains in all four scenarios.

Figure 4.12 shows the realized gains in these four scenarios. In Scenario 1, the stand-alone HB antenna maintains stable gain within its original impedance bandwidth (1.7-2.7 GHz) but experiences a sharp drop below 1.7 GHz due to poor matching. In Scenario 2, embedding the HB antenna in a standard-height LB cavity causes severe

gain fluctuations, reaching a minimum of 3.4 dBi at 2.4 GHz with a variation of 6.8 dB, primarily due to blockage and scattering by the LB antenna, as noted in prior studies. In Scenario 3, however, when the HB antenna is integrated with the newly proposed low-profile LB antenna, the gain performance improves significantly: the minimum gain is raised to 6.0 dBi, and the overall variation narrows to 3.0 dBi. Finally, by introducing side reflectors in Scenario 4, the HB gain difference further decreases to 1.7 dB, while the realized gain spans from 7.1 dBi to 8.8 dBi.

Figure 4.13: Co-polarized patterns at 1.5, 1.9, 2.3, and 2.7 GHz for Scenarios 1, 2, and 4.

The radiation patterns in Figure 4.13 further confirm these findings by comparing the HB antenna's performance in Scenarios 1, 2, and 4 at 1.5 GHz, 1.9 GHz, 2.3 GHz, and

2.7 GHz. In Scenario 1, the standalone HB antenna maintains stable beamwidths but exhibits low boresight gain at 1.5 GHz due to impedance mismatch. In Scenario 2, the HB patterns are clearly degraded by severe scattering, leading to substantial beamwidth variations. Conversely, in Scenario 4, the HB antenna patterns are nearly restored to what they were in the standalone configuration (Scenario 1), indicating that cross-band scattering from the LB is effectively suppressed. This demonstrates that the proposed buffering scheme yields mitigated scattering and hence preserved HB radiation performance.

4.4.2 Suppressed Cross-Band Coupling

Leveraging the uniquely designed TCBL, the proposed shared-aperture dual-band array achieves effective cross-band isolation without requiring any added decoupling structures. Figure 4.14 demonstrates this by comparing the cross-band coupling coefficients $|S_{15}|$, $|S_{16}|$, $|S_{25}|$, and $|S_{26}|$ in both bands for two cases: with and without the TCBL. Due to symmetry, the behavior of other ports is similar and thus omitted.

From Figure 4.14(a), without the TCBL, the cross-band coupling coefficients remain below -18.7 dB in the LB but only -10.7 dB in the HB. In comparison, Figure 4.14(b) demonstrates that incorporating the TCBL provides considerable isolation improvement between the LB and HB antennas: the cross-band coupling coefficients improve to below -19.7 dB in the LB and -25.4 dB in the HB. This outcome confirms that the TCBL acts as an "electromagnetic buffer," effectively preventing cross-band energy from reaching other ports when either the LB or HB antennas are excited. Notably, the sharp resonance at 0.84 GHz in the LB cross-band coupling curves corresponds to a minor resonance of the HB antenna at this frequency. While this shift could be moved further from the operating band by adding a small resonance shifter to the HB balun [13], the cross-band isolation still remains above 24 dB even without such an adjustment.

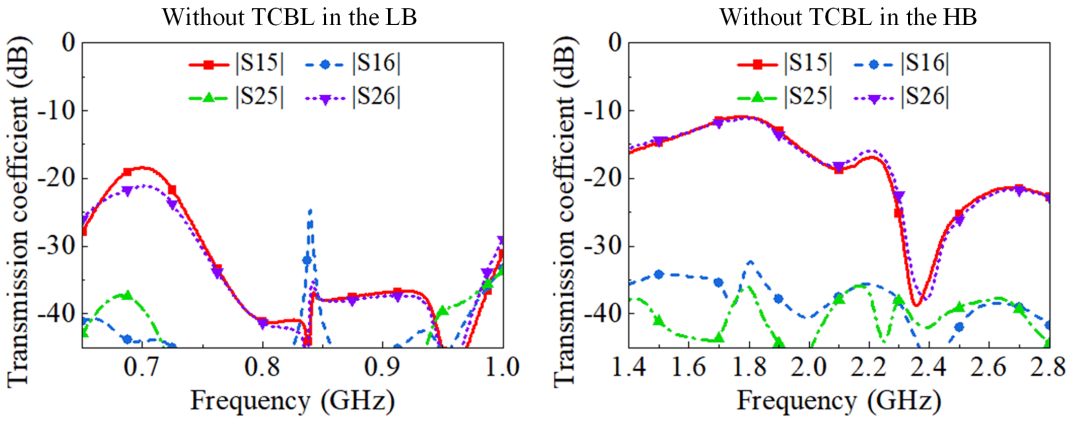

(a)

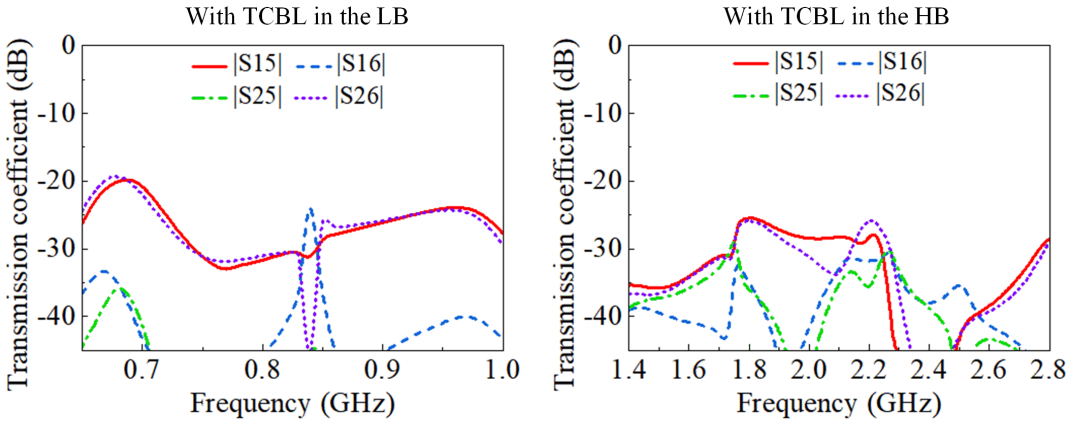

(b)

Figure 4.14: Comparison of cross-band coupling coefficients in both bands (a) without and (b) with the TCBL.

To illustrate this point, Figure 4.15(a) and (b) depict the current distributions in the array at three representative frequencies in the LB and HB, respectively. In Figure 4.15(a), when the LB ports (port 1 and port 3) are driven, strong coupling currents are observed on the TCBL, but the coupling to the HB antenna is well suppressed. In contrast, Figure 4.15(b) demonstrates that, with port 5 of the HB antenna excited, there is minimal current distributed at the LB ports, despite relatively strong coupling between the HB antenna and the TCBL at 1.5 GHz. This confirms that the TCBL effec-

tively isolates the LB and HB antennas from one another, thus diminishing cross-band interference.

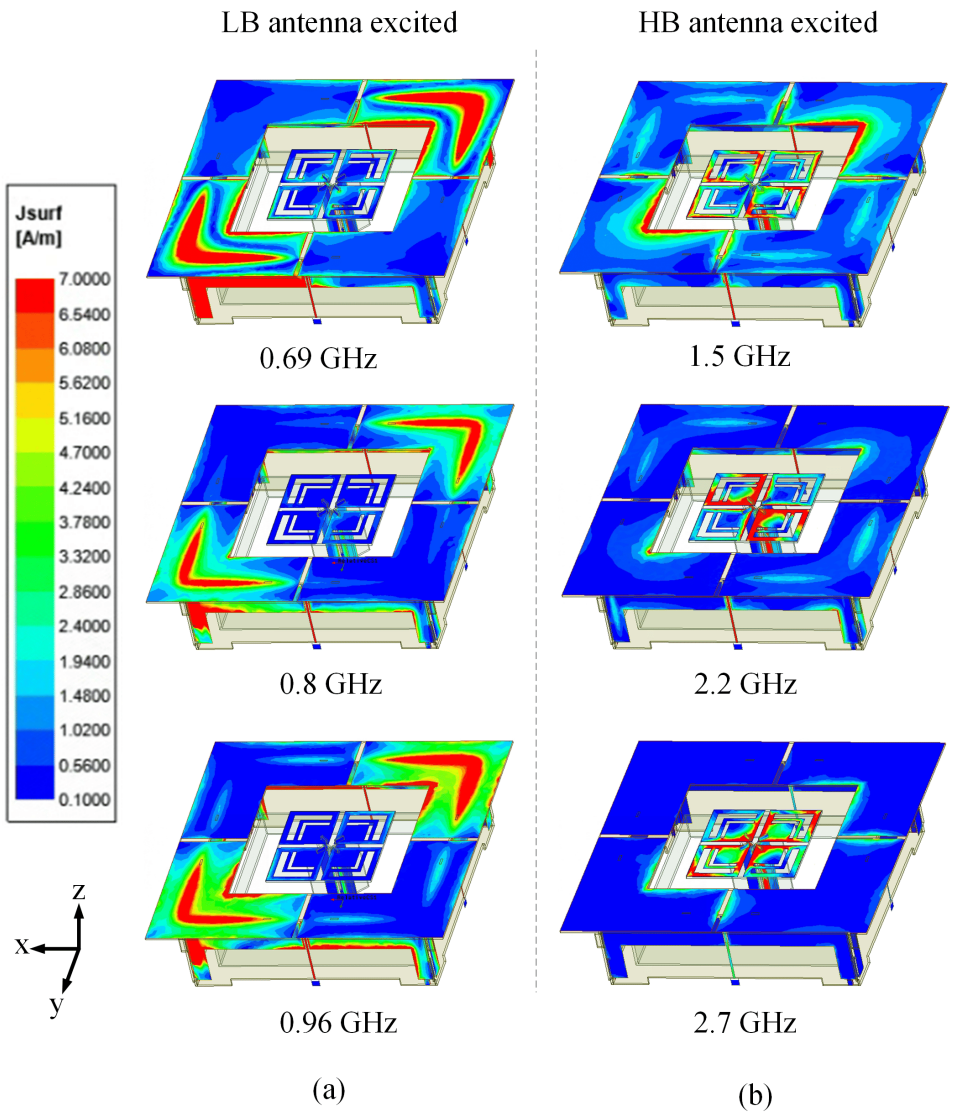

Figure 4.15: Current magnitude distributions at (a) 0.69, 0.8, 0.96 GHz in the LB and (b) 1.5, 2.2, 2.7 GHz in the HB.

4.5 Experimental Results

Figure 4.16 presents a photograph of the fabricated prototype. Two commercial power dividers are integrated into the LB antenna to feed its two polarization ports. A Rohde &

Schwarz ZNBT8 Vector Network Analyzer was employed for the S-parameter measurements, while a Keysight (Agilent) N5183A MXG Microwave Analog Signal Generator and an N5264B PNA-X Measurement Receiver were used in the far-field chamber for the radiation measurements.

Figure 4.16: Fabricated array prototype.

4.5.1 Measurement and Simulation Results

Figure 4.17 summarizes the performance of the completed LB antenna within this dual-band array. Generally, the measured results show good agreement with simulation. As observed in Figure 4.17(a), the measured reflection coefficients $|S_{c_1c_1}|$ and $|S_{c_2c_2}|$ are both under -10 dB over 0.69–0.96 GHz (yielding 32.7% bandwidth), and the measured mutual

coupling $|S_{c_1c_2}|$ is below -28.6 dB. Discrepancies between simulated and measured $|S_{c_1c_2}|$ values can be attributed to the fact that the simulation is idealized, whereas the practical setup includes real power dividers. Figure 4.17(b) indicates that the measured realized gains vary from 6.3 dBi to 8.3 dBi for port c_1 and from 6.8 dBi to 8.4 dBi for port c_2. Figure 4.17(c) shows stable measured radiation patterns for port c_1, where the boresight XPD exceeds 23.9 dB. Owing to the symmetrical geometry, the patterns for port c_2 remain similar and thus are not shown.

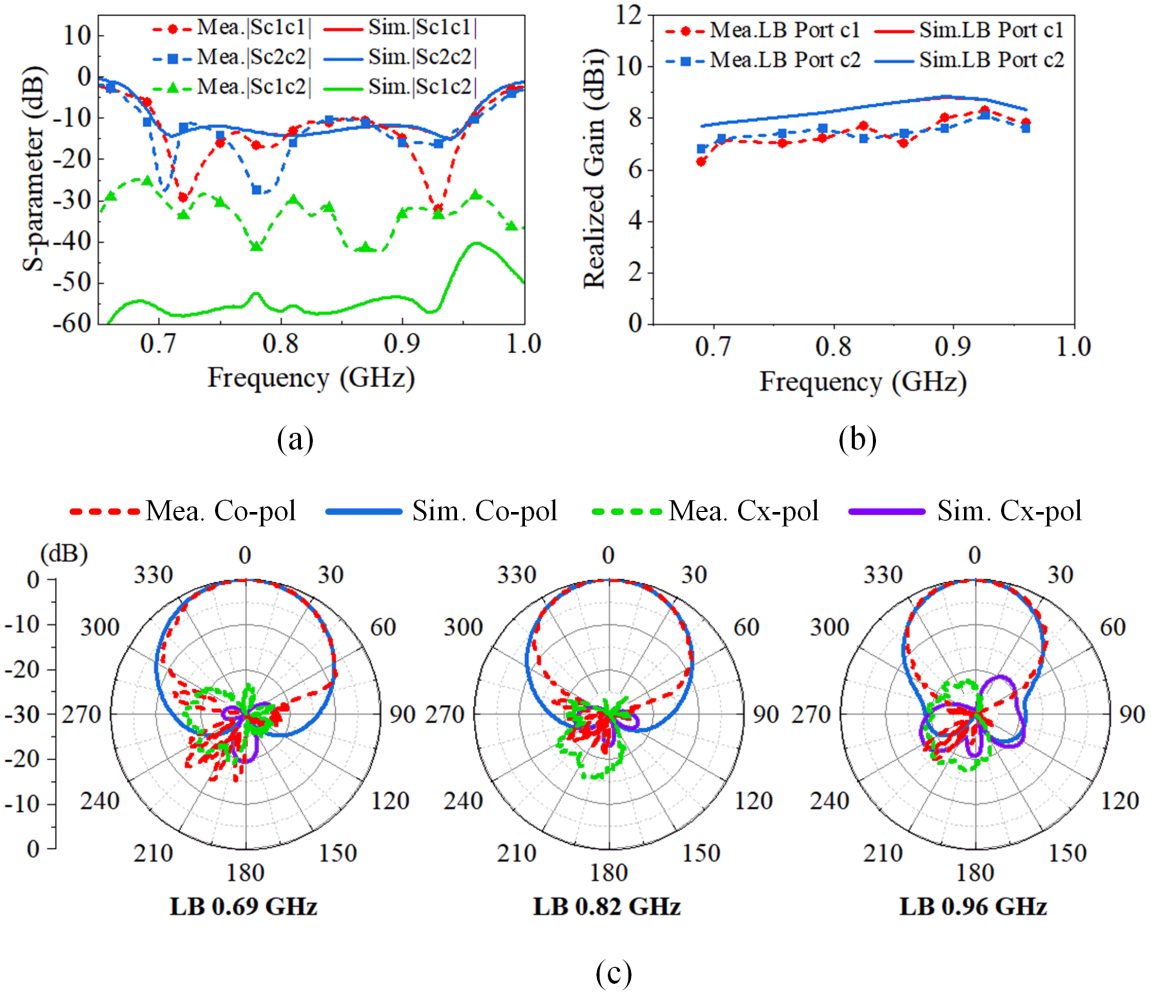

Figure 4.17: Measured and simulated LB performance. (a) S-parameters. (b) Realized gain. (c) Radiation patterns (port c1) in the yoz-plane.

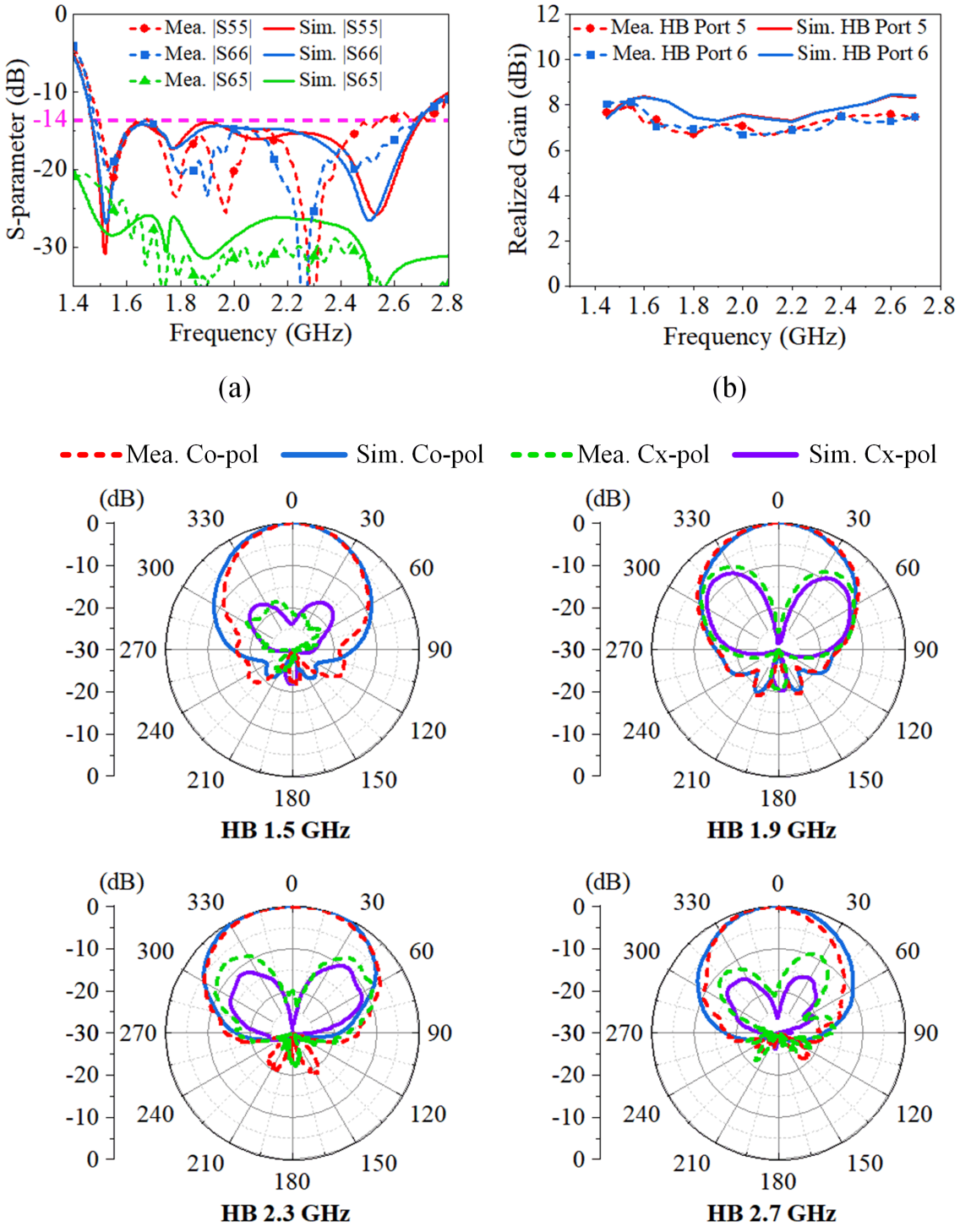

Figure 4.18: Measured and simulated HB performance. (a) S-parameters. (b) Realized gain. (c) Radiation patterns (port 5) in the yoz-plane.

Figure 4.18 compares the measured and simulated HB antenna results. From Figure 4.18(a), it can be seen that most of the measured $|S_{55}|$ and $|S_{66}|$ values remain below -14 dB within 1.47–2.7 GHz (59.0% bandwidth), except for a very narrow frequency region in which $|S_{55}|$ slightly rises to -12.8 dB. The measured $|S_{56}|$ stays below -22.3 dB throughout the same band. Figure 4.18(b) shows that the measured realized gains lie between 6.6 dBi and 7.9 dBi for port 5, and between 6.7 dBi and 8.0 dBi for port 6. In Figure 4.18(c), the measured HB radiation patterns align well with simulated results, and the measured XPDs exceed 18.5 dB at the boresight. Because the patterns for port 6 closely resemble those of port 5, only port 5 patterns are provided for succinctness.

Figure 4.19 illustrates the cross-band coupling levels between the LB and HB antennas in the realized array. The measured data agree closely with simulation, confirming cross-band coupling below -20.1 dB in the LB band and below -23.4 dB in the HB band.

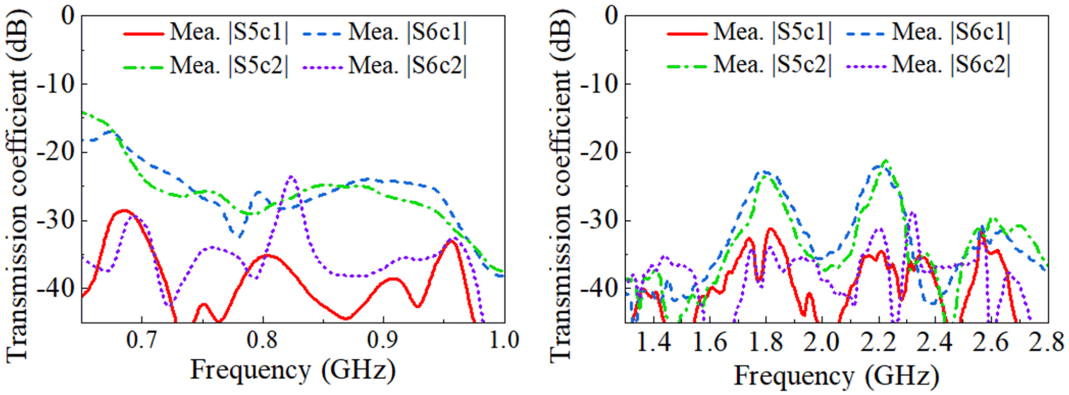

Figure 4.19: Measured and simulated cross-band coupling (a) in the LB and (b) in the HB.

4.5.2 Performance Comparison

Table 4.1 compares the proposed dual-band buffering-scheme-based shared-aperture array with several state-of-the-art designs. Within each category of array schemes, one recent work and one work with the lowest profile are included, sorted by ascending array

Table 4.1: Comparison of State-of-the-Art Dual-Band Dual-Polarized Shared-Aperture Arrays Based on Different Collocation Schemes

Ref. Year	Array Scheme	Array Profile	LB Antenna Size	LB Bandwidth	HB Bandwidth	Cross-Band Isolation (dB)
[14] 2024	Interleaved Scheme	0.159 λ_L	N.G.* ×N.G.* ×0.159λ_L	45.5% (1.7–2.7 GHz), VSWR < 1.92	14.1% (3.3–3.8 GHz), VSWR < 1.92	>28.0 (LB), >28.0 (HB)
[16] 2021	Interleaved Scheme	0.192 λ_L	0.303λ_L ×0.303λ_L ×0.192λ_L	40.0% (1.8–2.7 GHz), VSWR < 1.92	14.1% (3.3–3.8 GHz), VSWR < 1.92	>20.0 (LB), >20.0 (HB)
[82] 2018	Embedded Scheme	0.109 λ_L	0.394λ_L ×0.394λ_L ×0.109λ_L	18.7% (0.82–0.99 GHz), VSWR < 2	51.9% (1.68–2.86 GHz), VSWR < 2	>26.5 (LB), >20.0 (HB)
[24] 2023	Embedded Scheme	0.207 λ_L	0.284λ_L ×0.284λ_L ×0.207λ_L	40.2% (0.69–1.02 GHz), VSWR < 1.43	45.5% (1.70–2.71 GHz), VSWR < 1.43	>20.0 (LB), >20.0 (HB)
[86] 2022	Stacked Scheme	0.138 λ_L	0.285λ_L ×0.285λ_L ×0.119λ_L	32.7% (0.69–0.96 GHz), VSWR < 1.92	8.5% (3.4–3.7 GHz), VSWR < 1.92	>34.0 (LB), >32.0 (HB)
[29] 2024	Stacked Scheme	0.385 λ_L	0.303λ_L ×0.303λ_L ×0.136λ_L	30.0% (1.7–2.3 GHz), VSWR < 1.7	7.7% (2.5–2.7 GHz), VSWR < 1.7	>27.6 (LB), >27.0 (HB)
[30] 2021	Cavity-Backed Scheme	0.207 λ_L	0.414λ_L ×0.414λ_L ×0.207λ_L	32.7% (0.69–0.96 GHz), VSWR < 1.5	14.1% (3.3–3.8 GHz), VSWR < 1.5	>41.2 (LB), >25.4 (HB)
[31] 2021	Cavity-Backed Scheme	0.222 λ_L	0.396λ_L ×0.396λ_L ×0.222λ_L	32.7% (0.69–0.96 GHz), VSWR < 1.5	5.7% (3.4–3.6 GHz), VSWR < 1.5	N.G. (LB), >29.3 (HB)
This Work	Buffering Scheme	0.087 λ_L	0.345λ_L ×0.345λ_L ×0.087λ_L	32.7% (0.69–0.96 GHz), VSWR < 1.92	59.0% (1.47–2.7 GHz), VSWR < 1.5	>20.1 (LB), >23.4 (HB)

N.G. represents Not Given.
λ_L represents the free-space wavelength at the corresponding lowest frequency of the LB antenna.

profile. Compared to these other published methods, the newly proposed buffering scheme provides a substantially lower overall profile and simultaneously covers wide dual-band bandwidth. In fact, this configuration achieves the smallest array profile and the widest HB bandwidth among all compared works [14, 16, 24, 29–31, 82, 86]. Additionally, unlike other approaches requiring filtering or frequency-selective components [14, 16, 29, 82, 86], or that elevate the HB antenna [24], or utilize both concepts [30, 31], the proposed buffering scheme intrinsically suppresses cross-band coupling and scattering without additional filtering or decoupling measures.

4.6 Conclusion

An innovative shared-aperture dual-band array has been presented, based on a new buffering scheme that achieves a notably low profile of $0.087\lambda_L$, stable radiation characteristics, and suppressed cross-band interference across wide dual-band coverage of 0.69–0.96 GHz (32.7%) in the LB and 1.47–2.7 GHz (59.0%) in the HB. In contrast to existing shared-aperture arrays, this design leverages structural coupling to improve the overall performance while mitigating cross-band effects without resorting to any filtering or frequency-selective structures. Specifically, it features a unique buffer layer TCBL, which is tightly coupled with both the LB and HB radiators. By coupling to the LB radiators, the TCBL facilitates a notably low-profile LB design, leading to diminished blocking of the HB antennas and thus preserving the HB radiation patterns. Simultaneously, the TCBL introduces an additional resonance mode in the HB, extending the HB bandwidth from 45.5% to 59.0%. Moreover, even though the HB and LB antennas are positioned in close proximity, the array attains effective cross-band isolation exceeding 20.1 dB in the LB and 23.4 dB in the HB. The measurement results on a fabricated prototype corroborate the simulations, confirming the effectiveness of this approach.

CHAPTER 5

UWB TIGHTLY COUPLED DIPOLE ARRAY

Compared to multi-band antenna arrays that must address cross-band interference, the UWB array inherently avoids this issue by covering a continuous UWB frequency range. This chapter presents an UWB frequency-reconfigurable tightly-coupled dipole array (FR-TCDA). The proposed array achieves high radiation efficiency and wide-angle beam-scanning through a custom-designed frequency-reconfigurable layer combined with a wide-angle impedance matching (WAIM) structure. The reconfigurable layer, which employs PIN diodes, functions as a phase-shifting surface that transforms an unwanted out-of-phase ground-plane (GP) reflection into a favorable in-phase reflection with minimal insertion loss in each of its two contiguous frequency bands. Integrated dual-level, double-sided capacitively loaded loops (DLDS-CLLs) arranged in a coplanar configuration with the dipole elements serve as an effective WAIM structure, substantially improving beam-scanning performance. Each array element is fed by a Klopfenstein tapered balun equipped with a capacitance-loaded shorting pin, effectively suppressing common-mode resonances across the entire operating range. A 14×14 prototype was fabricated and measured, and the results align well with simulated predictions. In the broadside di-

rection, the two reconfigurable states cover $0.37-0.93\,\text{GHz}$ and $0.85-5.85\,\text{GHz}$ with a VSWR < 3 and radiation efficiency exceeding 95%. These two contiguous bands yield a combined bandwidth of 15.8:1 (0.37-5.85 GHz). When scanned up to $\{\pm 70^\circ, \pm 70^\circ, \pm 50^\circ\}$ in the $\{E-, D-, H\}$-planes, the array achieves a combined bandwidth of $13.7:1$ (0.42-5.77 GHz).

5.1 Introduction

The rapid growth of modern communications infrastructure drives the need for antenna arrays capable of supporting broad frequency range and wide-angle beam-steering while ensuring high-speed, stable, and uninterrupted connectivity [2]. Such stringent requirements have propelled the development of UWB phased arrays that meet evolving demands for bandwidth and angular coverage [87, 88].

Among various UWB phased array designs, tightly-coupled dipole arrays (TCDAs) [46, 89], based on Wheeler's current sheet theory [44, 45], have attracted significant interest. TCDAs offer exceptional bandwidth, compact form factors, low profiles, and excellent cross-polarization performance [48].

Typically, TCDAs achieve bandwidths around 5:1 by exploiting inter-element coupling [50, 89], and some variants have reached 10:1 bandwidths without lossy materials [51, 52]. However, further bandwidth extension is hindered by short-circuit resonances induced by the GP [89]. To mitigate these effects, highly lossy components have been introduced [53–55], but at the expense of reduced radiation efficiency. Another approach utilizes polarization-converting ground planes to achieve up to a 20.9:1 bandwidth without resistive losses, albeit with increased cross-polarization levels [56].

WAIM structures are often employed to broaden scan coverage and stabilize impedance [46, 58], achieving scanning angles up to 60° using dielectric superstrates [59, 60]. However, these methods can increase cost and weight. Some WAIM designs uti-

lize PCB fabrication methods, offering lightweight solutions. FSS-based WAIMs [55, 90], metasurfaces [62–64], planar metallic strips [65], wide-angle conjugate impedance matching (WACIM) layers [91], and planar split rings [66] have also been explored, but their bandwidths typically remain below 10:1.

This work introduces a frequency-reconfigurable TCDA (FR-TCDA) that employs a custom-designed reconfigurable layer and a DLDS-CLLs-based WAIM structure to achieve high efficiency and wide scanning angles across two contiguous frequency bands. The reconfigurable layer uses PIN diodes to provide a low-loss solution for overcoming short-circuit resonances without resorting to highly lossy materials. As a result, the array covers $0.37-0.93\,\text{GHz}$ (2.51:1) and $0.85-5.85\,\text{GHz}$ (6.88:1) at broadside with VSWR < 3, providing a combined bandwidth of 15.8:1 (0.37-5.85 GHz) while maintaining high radiation efficiency exceeding 95°. Under scanning up to $\pm 70^\circ$ in the E-plane, $\pm 70^\circ$ in the D-plane, and $\pm 50^\circ$ in the H-plane, these two states cover $0.42-0.93\,\text{GHz}$ (2.21:1) and $0.90-5.77\,\text{GHz}$ (6.41:1), respectively, realizing a combined 13.7:1 bandwidth (0.42-5.77 GHz). A 14×14 prototype was fabricated and tested, confirming the simulated performance.

The main contributions of this work are:

1. A new low-loss approach to overcome short-circuit resonances in TCDAs by employing a two-state reconfigurable layer that shifts in-phase reflection bands, enabling substantially enhanced bandwidth without sacrificing efficiency.

2. A DLDS-CLLs-based WAIM design to achieve improved scanning performance over two contiguous bands. Integrated in a co-planar configuration with the dipoles, the WAIM design is lightweight and features a straightforward, fabrication-friendly layout.

3. A specialized feeding scheme with Klopfenstein tapered baluns and capacitively-loaded shorting pins, ensuring UWB operation without undesirable resonances.

Section 5.2 describes the array configuration, including the reconfigurable layer, DLDS-CLLs, dipole arms with coupling pads, and the feeding scheme. Section 5.3 presents the fabrication and measurement results of the 14×14 prototype. Section 5.4 concludes the chapter.

5.2 Array Design

Figure 5.1(a) illustrates the unit cell of the proposed array, which was modeled and analyzed in ANSYS HFSS. The design exhibits a periodic spacing of 22 mm (0.43 λ_H, where λ_H represents the wavelength at the highest frequency) along both the x- and y-axes.

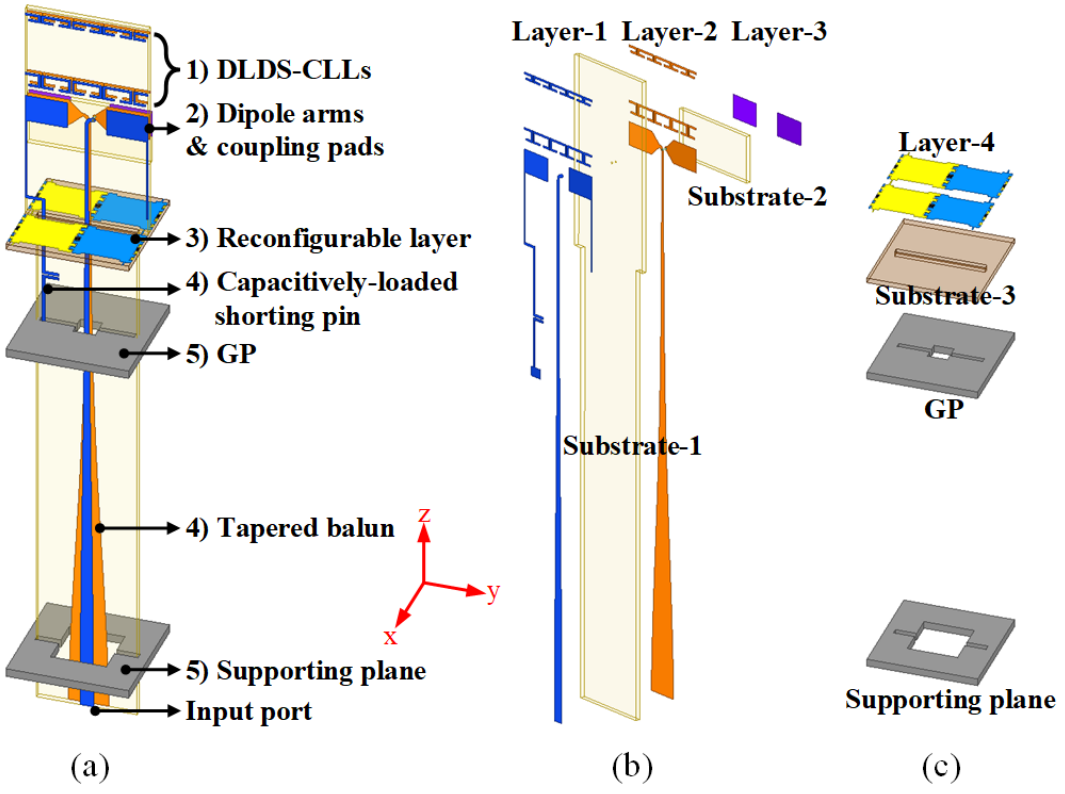

Figure 5.1: Unit cell design. (a) Isometric view. (b) Exploded view with vertically oriented elements. (c) Exploded view with horizontally oriented elements.

From top to bottom, the core parts of the unit cell include:

- **1)** DLDS-CLLs WAIM structure,
- **2)** dipole arms with coupling pads,
- **3)** reconfigurable layer,
- **4)** feeding section (incorporating the Klopfenstein tapered balun and the - capacitance-loaded shorting pin),
- **5)** GP and the supporting plane.

Figures 5.1(b) and 5.1(c) provide exploded views of the vertically and horizontally assembled structures, respectively. Components 1), 2), and 4) are printed on substrates oriented vertically, whereas Component 3), the reconfigurable layer, is realized on a horizontally oriented substrate. Substrate-1 is specially shaped to ensure secure vertical insertion into the corresponding slots on Substrate-3, the GP, and the supporting plane. Notably, the GP promotes unidirectional radiation and connects to the shorting pins. Meanwhile, the supporting plane provides mechanical support and alignment. Both the GP and the supporting plane have square apertures at their centers to prevent interference with the balun performance.

Substrate-1 and Substrate-2 use Taconic TLY (relative permittivity ε_r = 3, loss tangent $\tan\delta$ = 0.0009, thickness = 1.016 mm), whereas Substrate-3 employs Taconic TSM-DS3 (ε_r = 2.2, $\tan\delta$ = 0.0011, thickness = 1.016 mm).

Figure 5.2 provides examples of two array prototypes: a 1×3 linear array and a 3×3 finite array. Subsequent Sections 5.2.1–5.2.4 elaborate on the roles and design details of each key component.

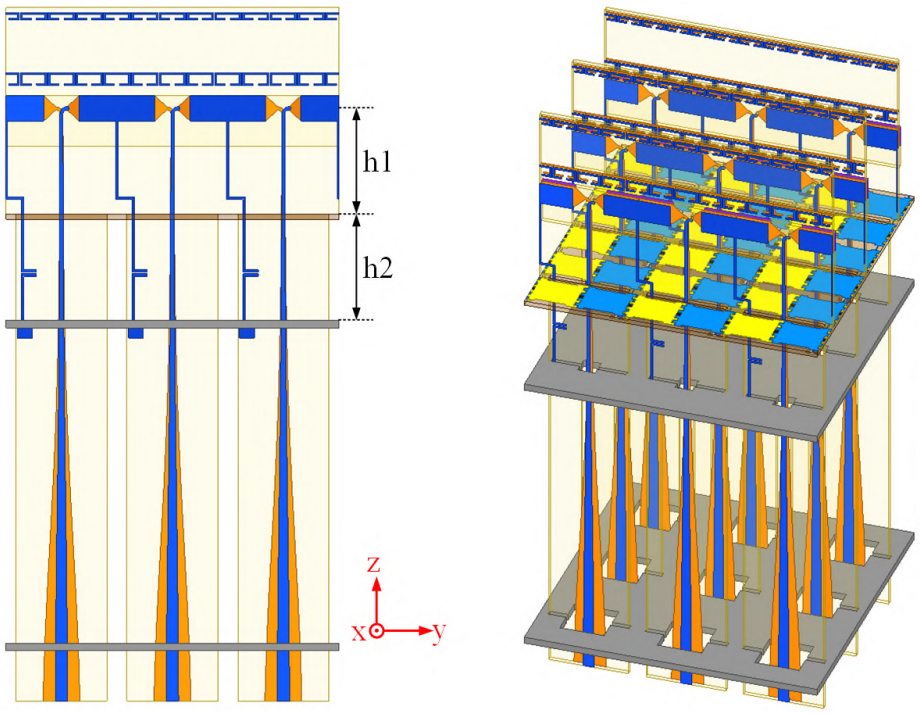

Figure 5.2: Example arrays: (a) Front view of a 1×3 linear array. (b) Isometric view of a 3×3 finite array.

5.2.1 Reconfigurable Layer

Figure 5.3(a) illustrates the detailed configuration of the reconfigurable layer's unit cell. Each cell consists of four metallic patches with interdigital edges, four PIN diodes, and two bias lines, all placed on the top side of Substrate-3. The Infineon BAR90-02ELS PIN diodes, which operate up to 6 GHz with low loss and distortion, were selected. The diodes are arranged between adjacent metallic patches, with a bias current of 10 mA. Those placed along the x-axis share the same orientation, while those placed along the y-axis are oriented oppositely. To control the diodes, each patch pair along the y-axis (in yellow and blue, respectively) is connected to the positive or negative DC bias lines. These lines are only 0.2 mm wide and oriented perpendicularly to the y-axis within each unit cell; thus, their influence on the co-polarization performance of the array is negligible.

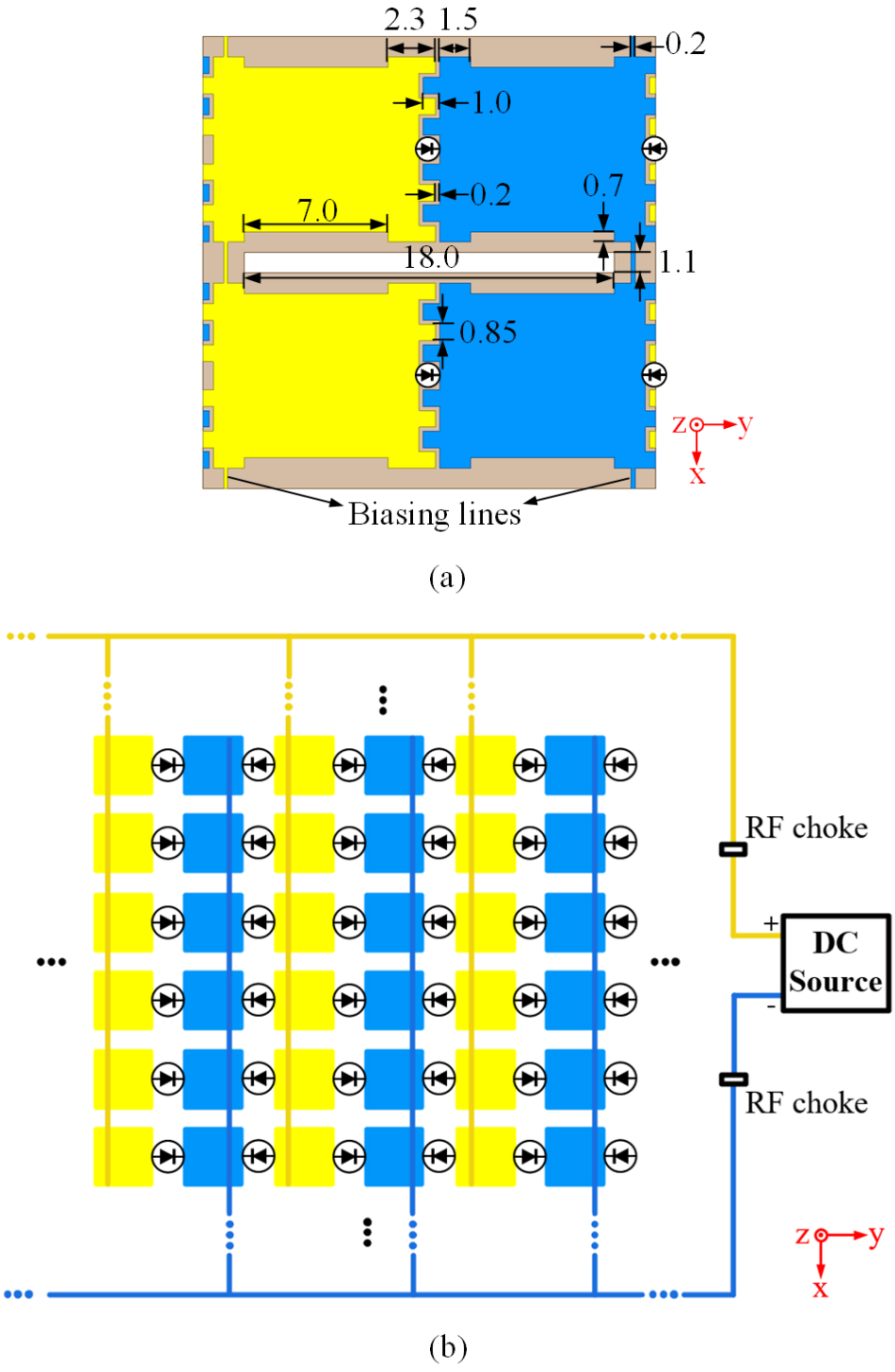

Figure 5.3: Reconfigurable layer. (a) Unit cell structure (dimensions in millimeters). (b) Biasing network schematic.

Figure 5.3(b) depicts the bias network for the reconfigurable layer, where a symbolic

representation of a 3×3 patch array is shown for clarity, omitting the other cells. Two commercially available UWB RF chokes (Mini-Circuits ADCH-80A+) are placed at the bias line terminations close to the DC source to ensure proper DC/RF isolation.

One of the primary challenges in achieving a TCDA with over a 10:1 bandwidth is the so-called short-circuit resonance band. Such bands appear when the dipole-to-GP distance approximates $\lambda/2$ at certain frequencies. In this configuration, the upward-traveling wave and the wave reflected from the GP have nearly equal magnitude yet opposite phase, causing mutual cancellation [47, 53, 87]. Moreover, these short-circuit resonances repeat periodically at heights $N\lambda/2$ (where N is a positive integer), degrading radiation performance and limiting the bandwidth. The proposed reconfigurable layer effectively prevents the occurrence of these bands.

In our design, the dipole surface is positioned 42 mm above the GP, leading to a short-circuit resonance at 3.57 GHz where $\lambda_s = c/2(h_1 + h_2)$. By inserting the custom reconfigurable layer between the dipole and the GP, the undesirable out-of-phase reflection band is replaced by an in-phase reflection band, facilitated by the PIN diodes that switch between two distinct frequency-band states. This reconfigurability extends the overall operating bandwidth while preserving the array's aperture size and maintaining low insertion loss.

A simplified unit-cell model was analyzed to investigate the in-phase reflection band, as shown in Figure 5.4(a). The reconfigurable layer lies directly above the GP and is surrounded by periodic boundaries in the x- and y-directions. A Floquet port is placed at the same height as the dipole surface, with the electric field aligned along the dipole's co-polarization direction (i.e., the y-axis). According to the datasheet, the PIN diodes are modeled as 1.8 Ω in series with 0.2 nH inductance in the on-state, and as 0.21 pF in series with 0.2 nH inductance in the off-state, consistent with lumped boundary modeling in HFSS.

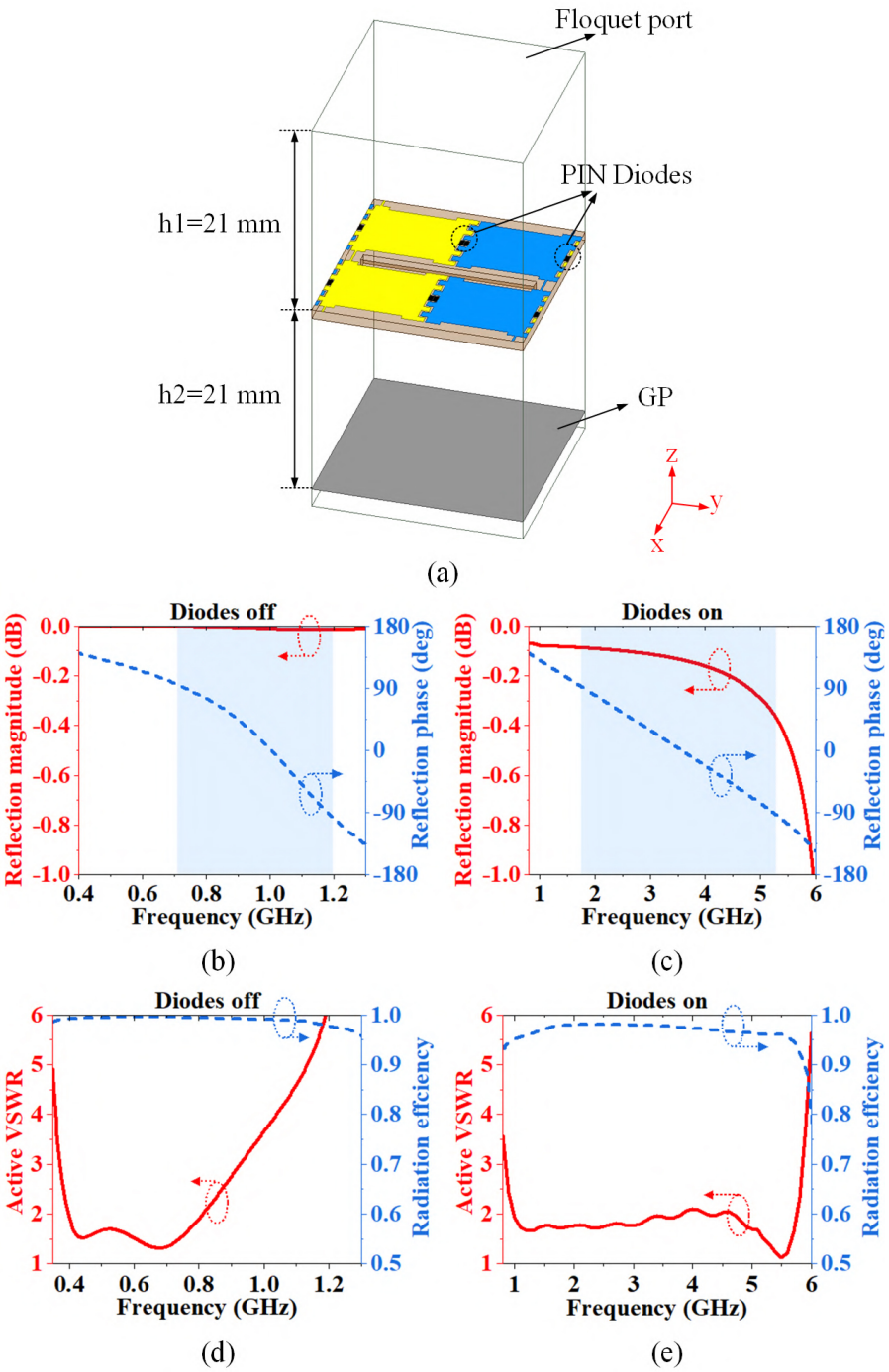

Figure 5.4: Reflection properties of the reconfigurable layer. (a) Simplified model. (b)–(c) Reflective magnitude and phase for off- and on-states, respectively. (d)–(e) VSWR and radiation efficiency of the FR-TCDA unit cell in broadside for the off- and on-states.

Figures 5.4(b) and 5.4(c) plot the reflection magnitude and phase for the simplified

model in the off-state and on-state, respectively, highlighting the regions where ±90° in-phase reflection occurs. With the diodes off, the in-phase reflection band is at relatively lower frequencies; when the diodes are on, it shifts to higher frequencies. This shift enables the final array (Figure 5.1(a)) to achieve band reconfiguration, verified by the broadside impedance matching results in Figures 5.4(d) and 5.4(e). The array's VSWR < 3 ranges from 0.37–0.93 GHz in the off-state and from 0.85–5.85 GHz in the on-state. For convenience, these two states are referred to as the lower-band state (LS) and higher-band state (HS) hereafter. The overall design further broadens the operating ranges of both states via the DLDS-CLLs and coupling pads, shifting the LS slightly downward in frequency to enlarge the contiguous dual-band coverage.

Critically, after parameter optimization, this reconfigurable approach offers high radiation efficiency in both states (exceeding 95% when the beam is aimed in the broadside direction), as evidenced in Figures 5.4(d) and 5.4(e). This advantage largely derives from the low insertion loss of the reconfigurable layer: for the off-state, the loss remains below 0.015 dB, whereas for the on-state it stays below 0.35 dB, as observed in Figures 5.4(b) and 5.4(c). These values are significantly lower than what is typically encountered in a GP loading approach employing resistive frequency selective surfaces, which can incur reflection losses near 3.8 dB [53].

To extend coverage of the LS while ensuring minimal overlap with the HS band, interdigitated patch edges are introduced on the reconfigurable layer. Three representative patch designs, illustrated in Figure 5.5(a), were examined:

- Model 1 has wider (3 mm) straight-edge gaps,
- Model 2 uses narrower (1 mm) straight-edge gaps,
- Model 3 employs interdigitated edges.

From Model 1 to Model 3, stronger coupling between adjacent patches arises, producing

distinct phase responses. Figures 5.5(b) and 5.5(c) present the reflection phases in the HS and LS, respectively. With the diodes on (HS), all three models exhibit nearly identical responses since the patches are electrically connected. In the off-state (LS), they differ noticeably. Model 1 shows a high-frequency segment of the LS in-phase reflection band overlapping with the HS band, reducing the overall dual-band coverage. Progressively increasing interpatch coupling (as in Model 3) shifts the LS band to lower frequencies, mitigating overlap with the HS. However, the in-phase reflection band becomes narrower as it migrates downward, necessitating careful parameter tuning of the interdigital geometry to optimize the collective bandwidth.

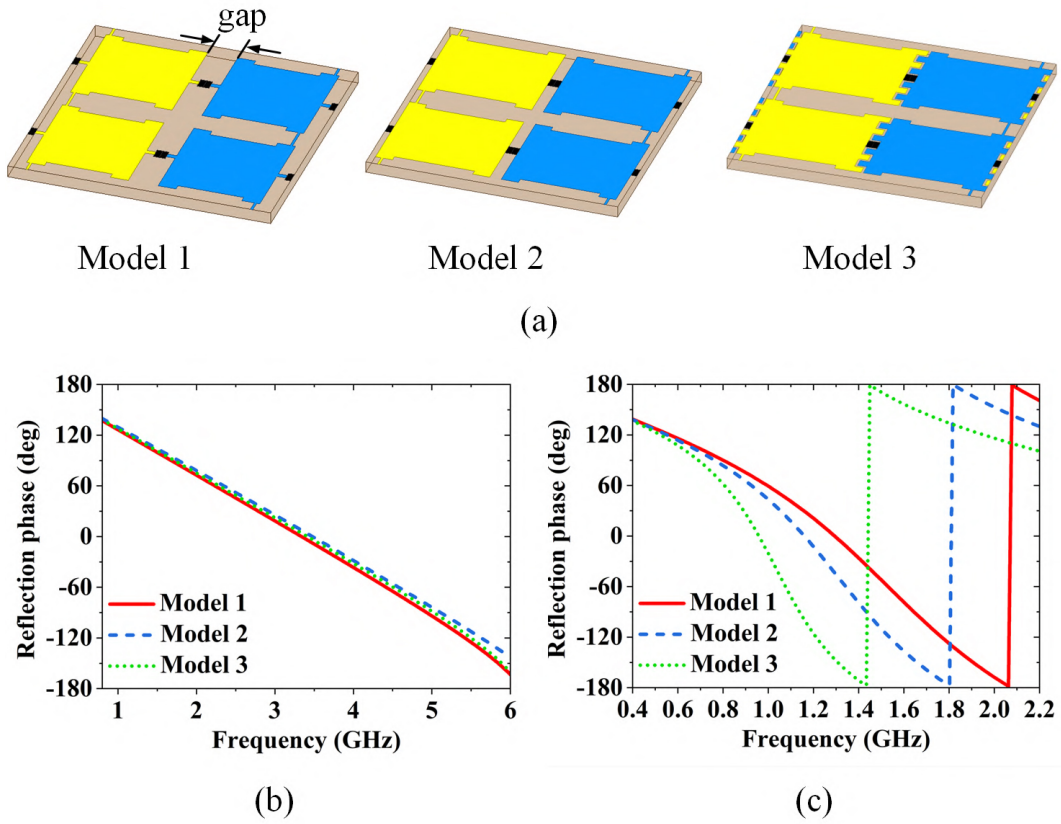

Figure 5.5: Influence of patch-edge configuration. (a) Three patch-edge models. (b) Reflection phases in the on-state. (c) Reflection phases in the off-state.

The power consumption of the diodes is minimal. It was assessed by comparing the

realized gain of the actual unit cell (with real diode values) to that of a reference unit cell (with ideal PEC segments in place of diodes). At the on-state, this difference was below 0.07 dB across the band of operation, and was negligible at the off-state (where ohmic losses are virtually absent).

5.2.2 Dual-level Double-sided Capacitively Loaded Loops (DLDS-CLLs)

The WAIM configuration, referred to as DLDS-CLLs, is illustrated in Figure 5.6. These CLLs share a co-planar arrangement with the dipole arms, producing a lightweight, readily manufactured structure. The DLDS-CLLs have a periodicity that is one-quarter of the overall 22 mm unit cell spacing. Two levels of CLLs are implemented, each patterned on both sides of Substrate-1. Minor dimensional differences are introduced at each level to optimize performance throughout both contiguous frequency bands of interest.

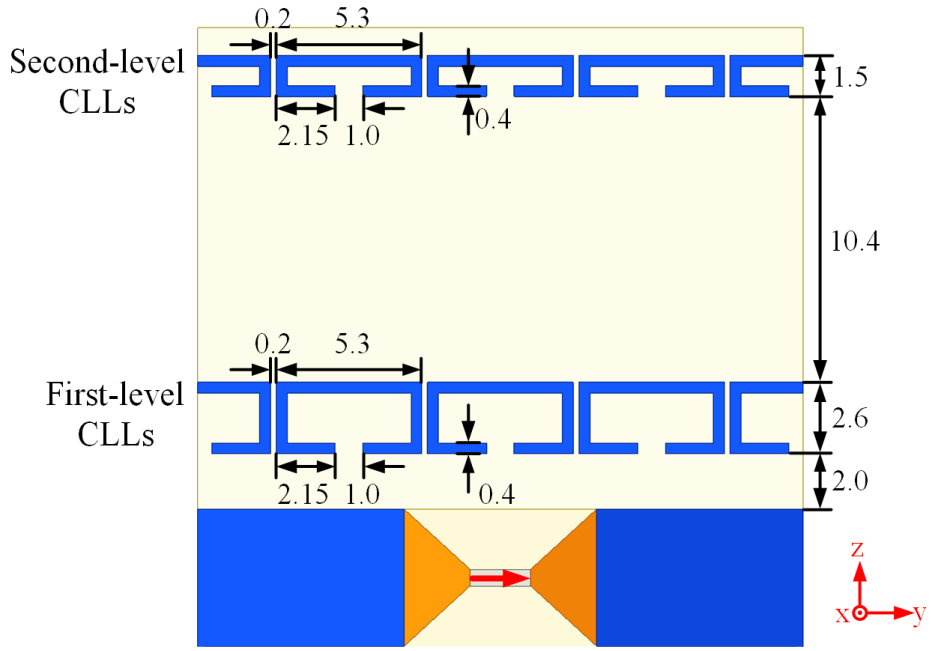

Figure 5.6: Dimensions of the DLDS-CLLs (in millimeters).

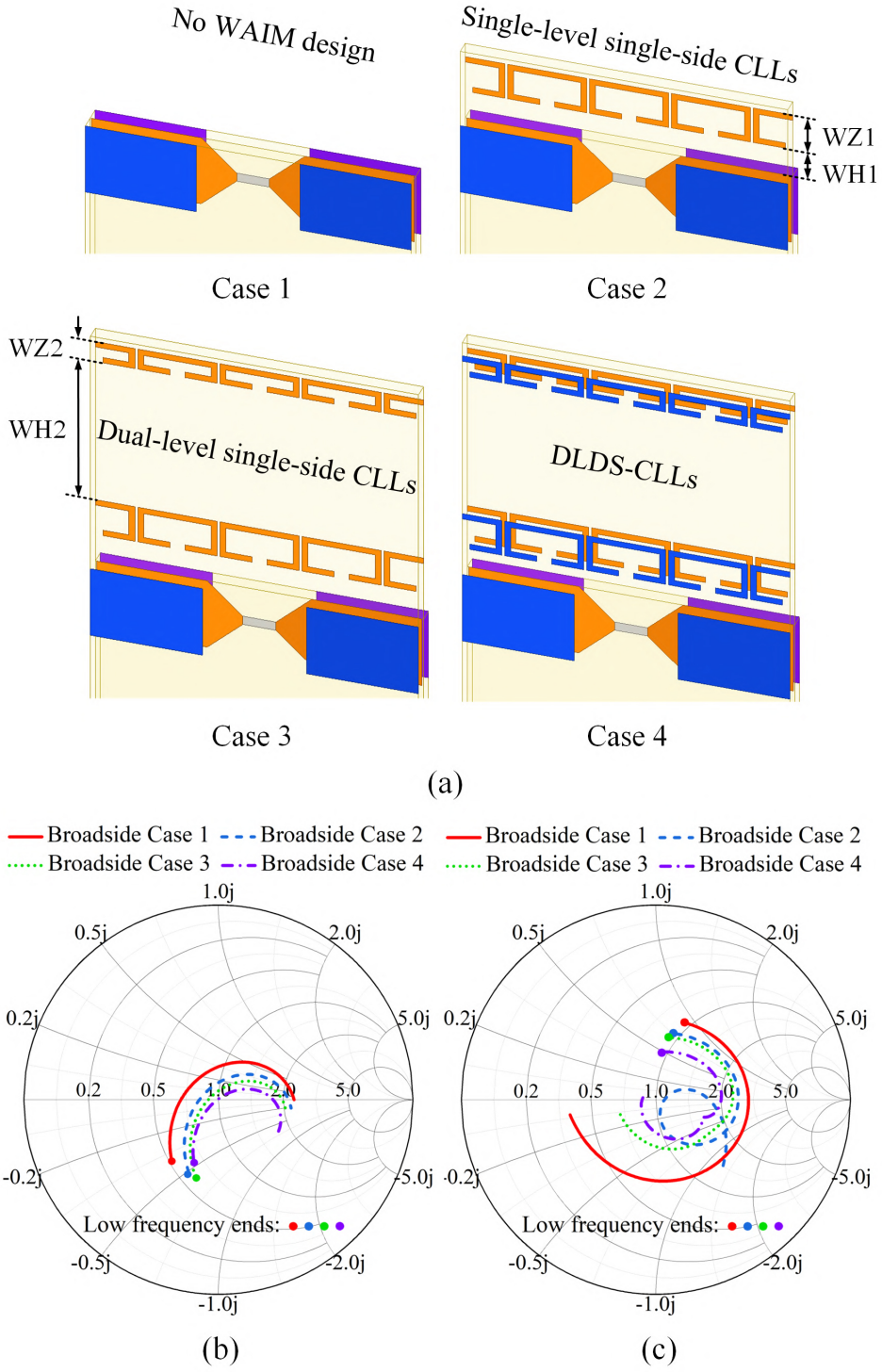

Figure 5.7: (a) Four simplified WAIM models. (b)–(c) Input impedance (normalized to 150 Ω) at broadside for the off-state (b) and on-state (c).

The DLDS-CLLs help alleviate variations in input impedance that arise at broad-

side and throughout beam scanning, across the array's two reconfigurable bands. To demonstrate how the DLDS-CLLs minimize impedance variation under broadside and scanning conditions, four configurations were compared in simulation:

- Case 1: no WAIM,
- Case 2: single-level single-side CLLs,
- Case 3: dual-level single-side CLLs,
- Case 4: the final DLDS-CLLs.

These four cases are illustrated in Figure 5.7(a). A simplified model was used wherein an ideal-fed dipole element was combined with a reconfigurable-layer state emulated by changing the dipole's height above the GP. Figures 5.7(b) and 5.7(c) show the active input impedance results for the LS and HS, respectively, for all four cases. The results confirm that the DLDS-CLLs (case 4) yield the smallest impedance variation and a correspondingly superior matching profile.

A series of parameter studies elucidated the evolution from single-level to dual-level CLLs. The selected key parameters include: WZ_1 (length of the first-level CLLs along the z-axis), WH_1 (spacing between the dipole and the first-level CLLs), WZ_2 (length of the second-level CLLs along the z-axis), and WH_2 (spacing between the first- and second-level CLLs). In case 2, the operational bandwidths for the LS and HS were comparatively narrow, and a clear trade-off existed between them. Figure 5.8(a) demonstrates that increasing WH_1 extends the LS band by pushing its upper frequency limit higher. However, this also reduces available HS bandwidth, as shown in Figure 5.8(b). Likewise, varying WZ_1 yields a similar trade-off, as shown in Figures 5.8(c) and 5.8(d).

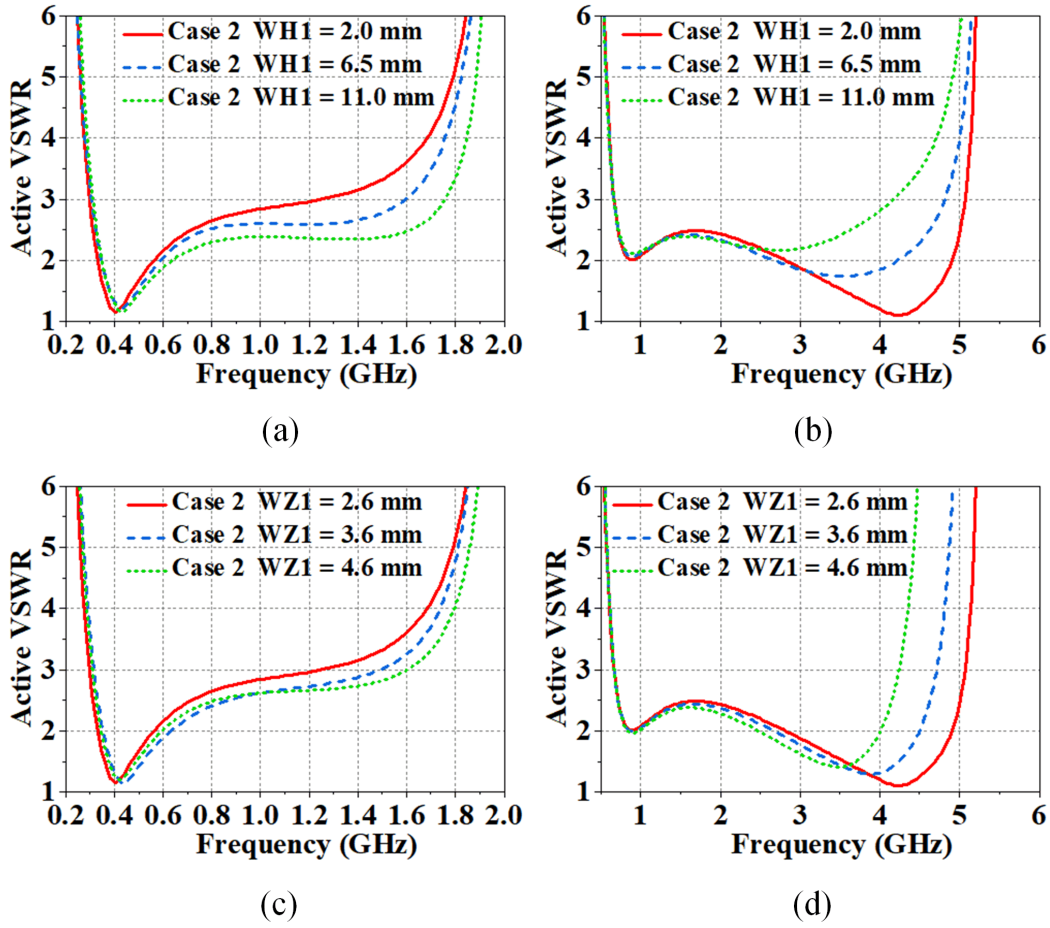

Figure 5.8: Parametric analysis of first-level CLLs in case 2: (a)–(b) effect of WH1 and (c)–(d) effect of WZ1.

To address this trade-off, a second-level of CLLs (case 3) was added, leading to an expansion of both bands simultaneously. As depicted in Figures 5.9(a)–5.9(d), the design parameters WH_2 and WZ_2 primarily fine-tune HS bandwidth while exerting less impact on the LS. Nevertheless, WH_2 still controls the HS bandwidth, initially increasing it, then gradually decreasing it for large values, as seen in Figures 5.9(a) and (b). Meanwhile, WZ_2 mainly modifies high-frequency matching in the HS, as seen in Figures 5.9(c) and (d).

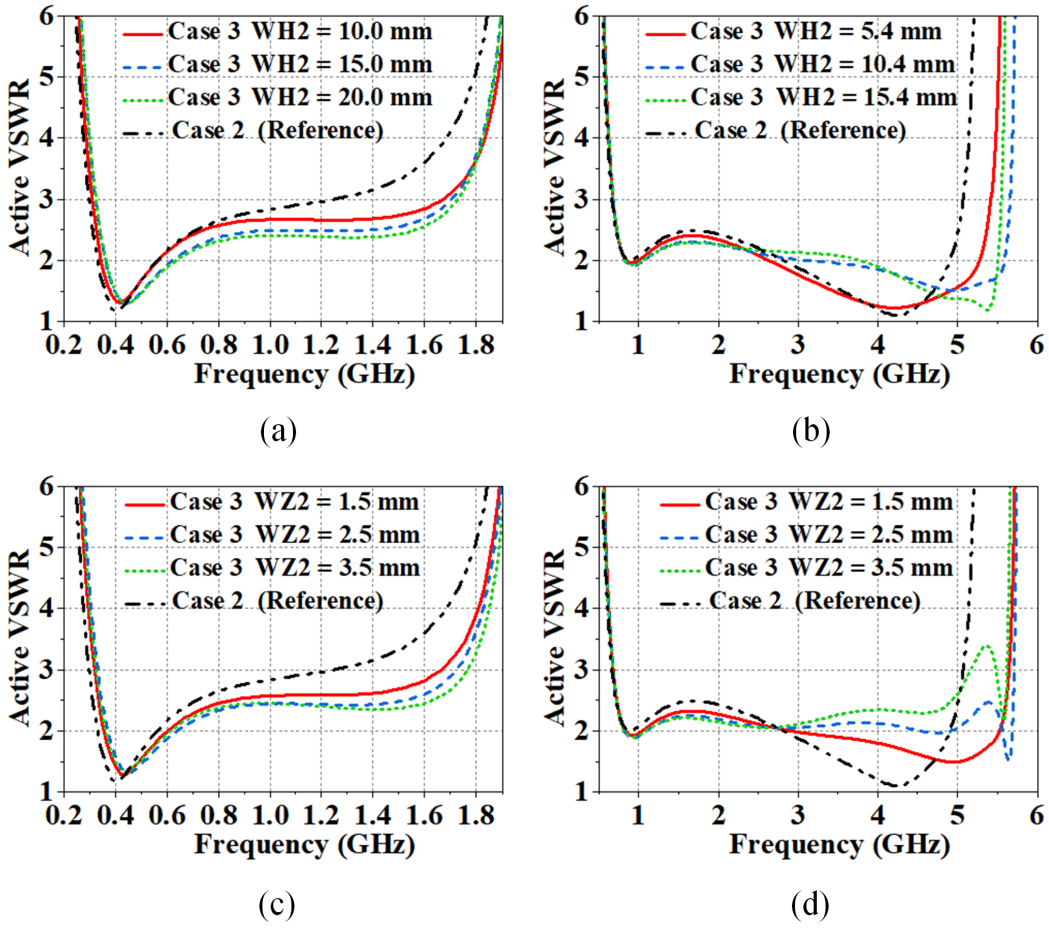

Figure 5.9: Parametric analysis of second-level CLLs in case 3: (a)–(b) effect of WH2 and (c)–(d) effect of WZ2.

Finally, placing dual-level CLLs on both sides of Substrate-1 (case 4) offered additional mitigation of the high impedance variation present in case 3. The final dimensions of the DLDS-CLLs resulted from an overall optimization that balanced performance in both reconfigurable states. Figures 5.10(a) and 5.10(b) compare the input impedance loci when the beam is scanned up to ±45° in the E-/H-planes. Case 4 exhibits significantly less variation compared to case 1, improving matching throughout scan. The fully optimized geometries of the DLDS-CLLs are indicated in Figure 5.6.

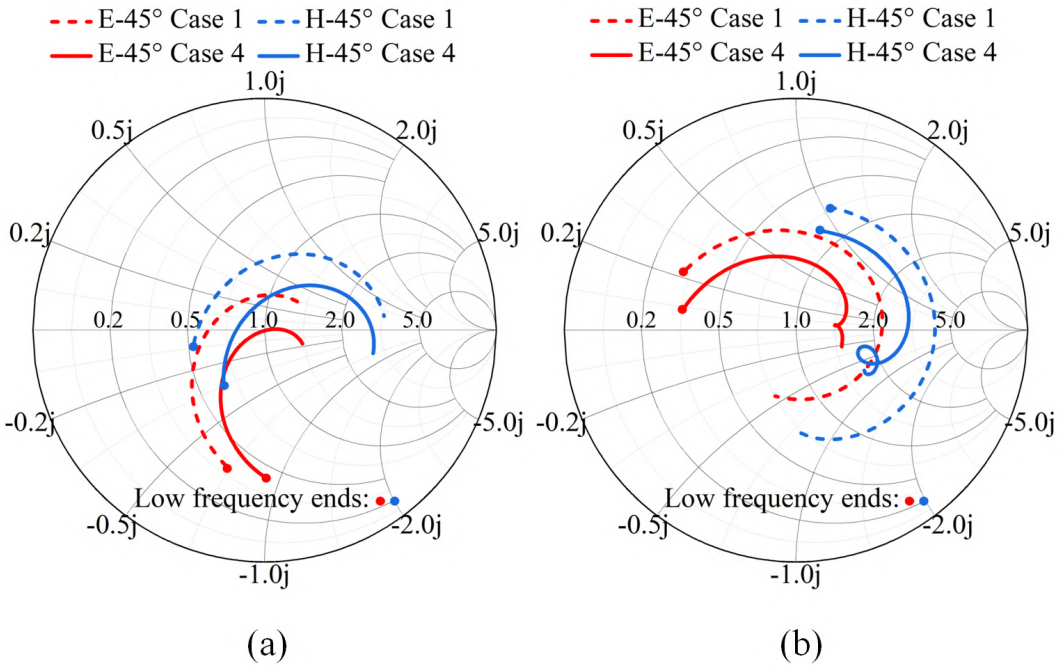

Figure 5.10: Input impedance under 45° E-/H-plane scanning for (a) 0.42–1.0 GHz (LS) and (b) 1.0–5.0 GHz (HS) in the no-WAIM vs. final WAIM case.

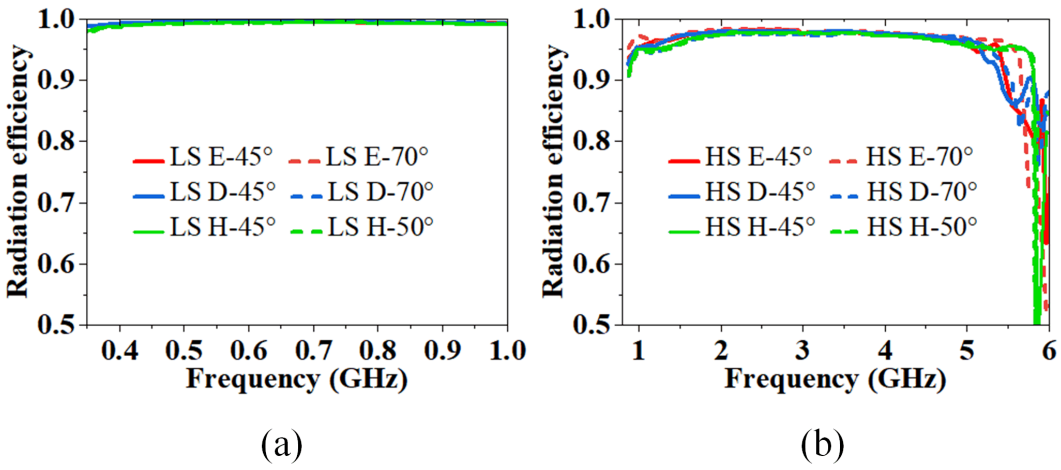

Figure 5.11: Simulated radiation efficiency for various scan angles in the (a) LS and (b) HS.

Figure 5.11 shows the radiation efficiency of the array's unit cell across several scan angles: E-/D-/H-planes at 0°, 45°, and 70°. In the LS, the efficiency stays above 98.6%.

In the HS, it exceeds 95.0% for most of the band, dropping only at its high-frequency edge, particularly for oblique angles such as E-45°, D-45°, and D-70°. Even under these conditions, it remains above 86.2%.

5.2.3 Dipole Arms with Coupling Pads

Figure 5.12 illustrates the dipole arms and their sandwich-like capacitive coupling pads, which offset the inductive reactance at lower frequencies introduced by the GP [89].

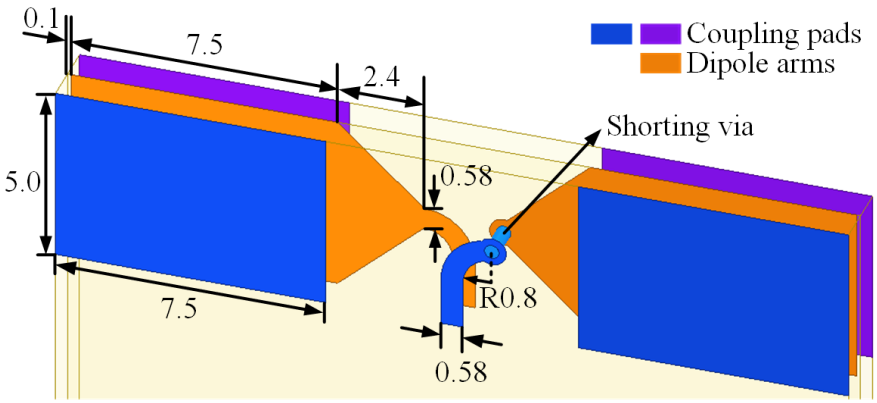

Figure 5.12: Dipole arms and coupling pads (in millimeters).

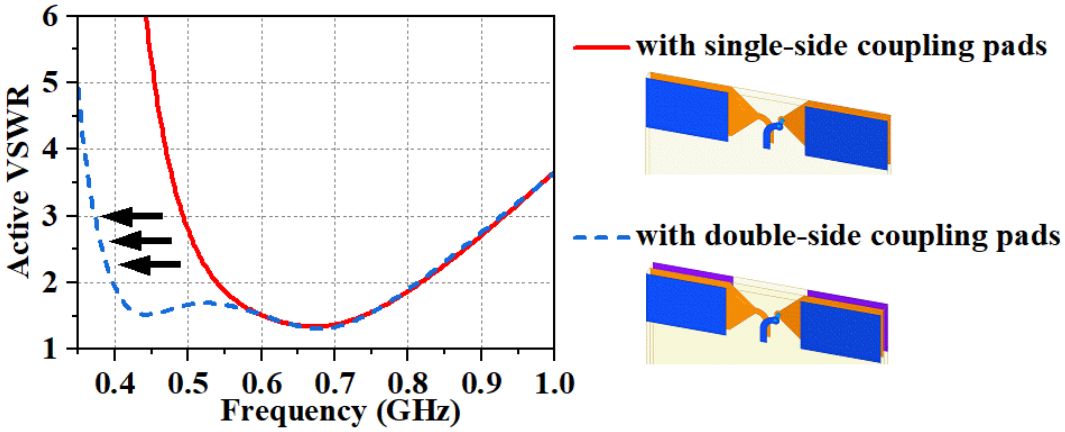

Figure 5.13: Influence of single- vs. double-sided coupling pads on LS VSWR at broadside.

Figure 5.13 compares the broadside VSWR for the LS of the proposed frequency-

reconfigurable TCDA (FR-TCDA) when employing single-side and double-side coupling pads. It is seen that the double-side case notably extends the lower edge of the LS bandwidth, confirming its effectiveness in improving low-frequency matching.

5.2.4 Feeding Scheme

A tapered balun approach is employed here, leveraging Klopfenstein tapers [76] to achieve multi-octave coverage with high impedance transformation ratios and minimal insertion loss [55, 63, 75, 77]. As shown in Figure 5.14(a), the designed balun transitions from a 50 Ω unbalanced "port 1" to a 150 Ω balanced "port 2". Figure 5.14(b) depicts the balun's S-parameters for different taper lengths, demonstrating that increasing the taper length improves the reflection coefficient at lower frequencies. The final optimized length is 115 mm, ensuring $|S_{11}| < -15$ dB and $|S_{21}| < 0.4$ dB across the passband.

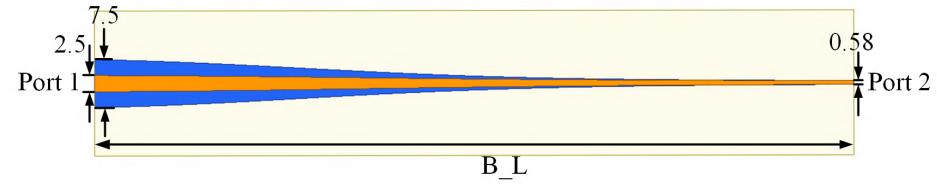

(a)

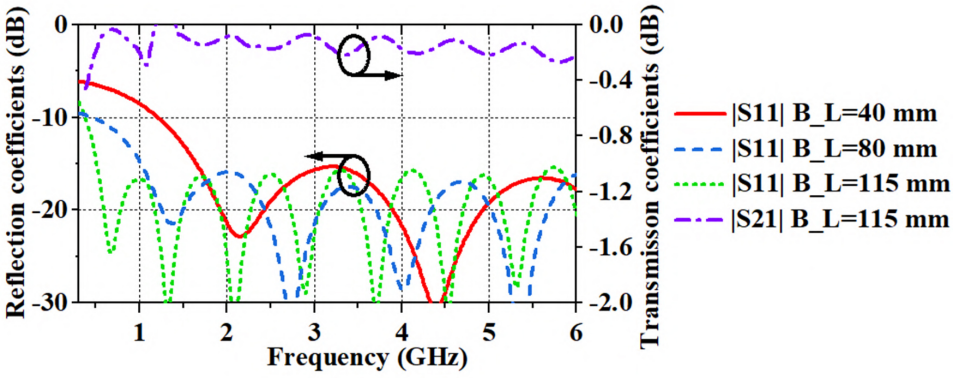

(b)

Figure 5.14: Klopfenstein tapered balun: (a) geometry (mm). (b) S-parameters for 50–150 Ω transformation at various lengths.

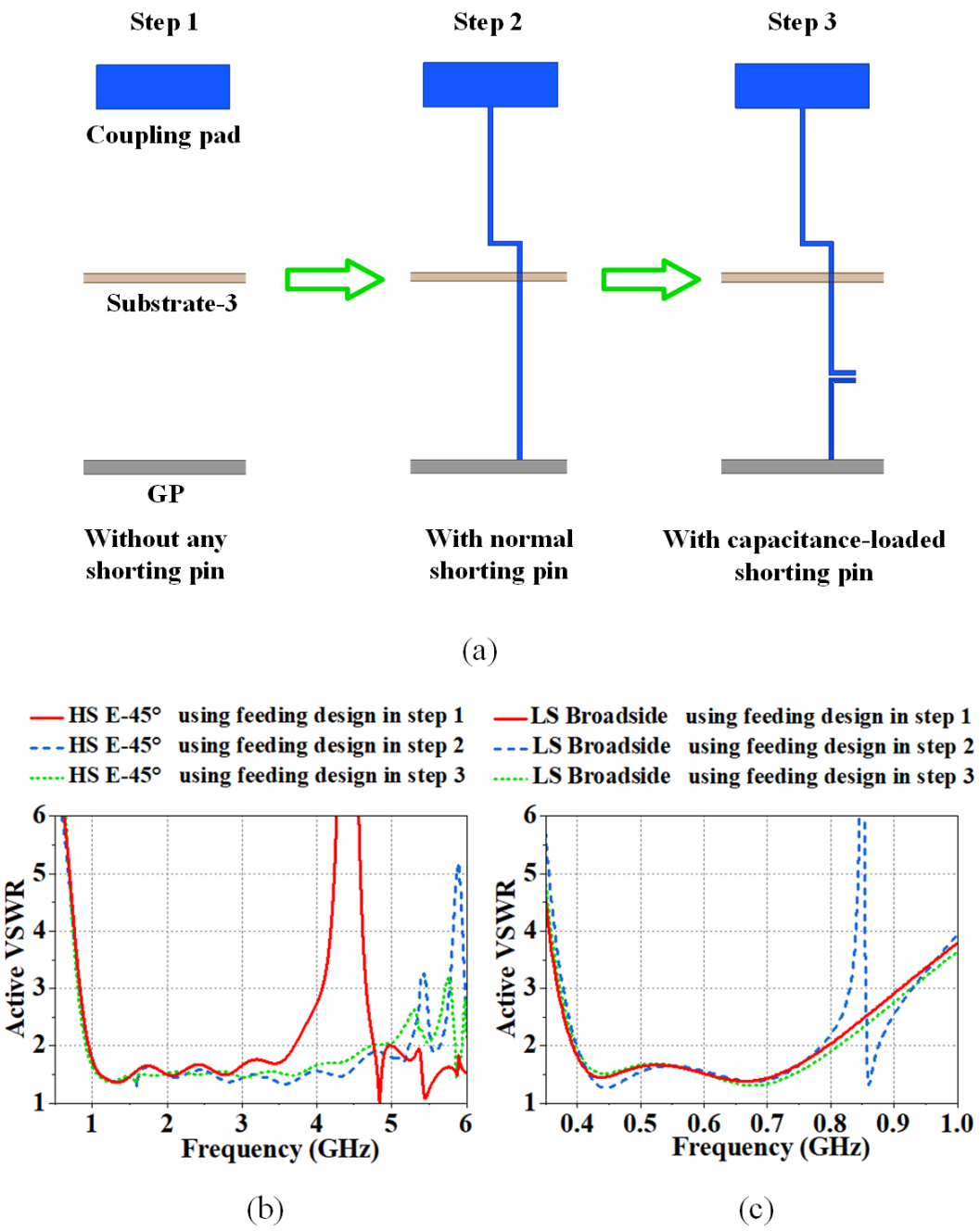

Figure 5.15: (a) Evolution of the capacitance-loaded shorting pin. (b)–(c) VSWR performance at E-45° (HS) and broadside (LS).

Although the baluns themselves function effectively, the dense array environment can introduce undesirable common-mode currents on the baluns and dipole arms [67, 68], leading to common-mode resonances that restrict the operating bandwidth. Previously

reported TCDAs with bandwidths greater than 10:1 using tapered baluns often utilized highly lossy materials and did not face the challenge of common-mode resonances. However, this came at the expense of reduced efficiency.

In contrast, this design employs customized capacitance-loaded shorting pins to suppress these common-mode resonances without resorting to excessive losses. Figures 5.15(a) and (b) illustrate the shorting-pin design steps. Initially, integrating the balun into the unit cell introduced a common-mode resonance at 4.3 GHz in the HS when the beam scanned up to 45°in the E-plane, as shown by the red solid line in Figures 5.15(b). Normal shorting pins were added to suppress this resonance, but they caused a new resonance at 0.84 GHz in the LS, as depicted by the blue dashed line in Figures 5.15(b). To address this issue, a capacitance was added to the shorting pin, as shown in step 3 of Figures 5.15(a). This adjustment eliminated the LS resonance while preventing the HS resonance from reappearing, as indicated by the green dotted lines in both Figures 5.15(b) and (c).

Figure 5.16 clarifies the mechanism for tuning out the LS resonance. As illustrated in Figure 5.16(a), a resonance loop exists in each unit cell due to the GP and the resulting image currents. This loop causes an unwanted resonance in the LS, with its frequency determined by the loop path length and the inter-element capacitance related to the coupling pads. Because the coupling pad dimensions were determined prior to integrating the feeding parts, introducing a gap capacitance in the shorting pin below the reconfigurable layer (Substrate-3) was necessary to break this unwanted loop at 0.84 GHz, as shown in Figure 5.16(b). Placing the gap capacitance below Substrate-3 ensures minimal interference with the reconfigurable layer's role in suppressing the HS common-mode resonance. Through systematic optimization, this final feed network efficiently covers both reconfigurable bands without any detrimental resonances.

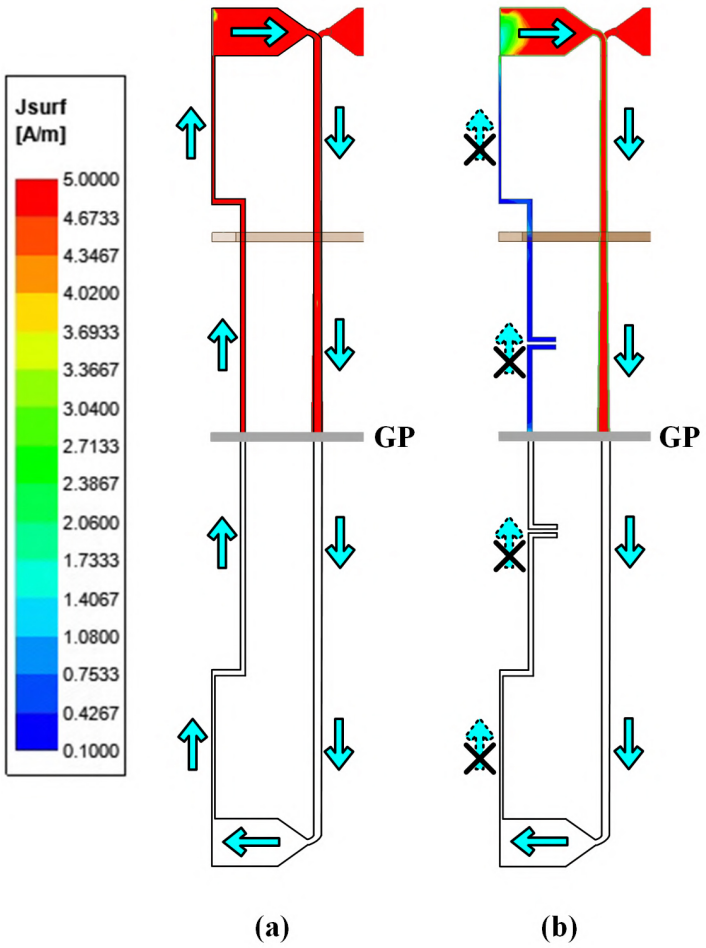

Figure 5.16: Current loop at 0.84 GHz in the LS (blue arrows) (a) with normal pin and (b) with capacitance-loaded pin.

5.3 Experimental Results

5.3.1 Fabrication and Assembly

Figure 5.17 presents the fabricated 14×14 element array. To assemble the array, Substrate-2 was first secured onto Substrate-1 by using dielectric screws. Substrate-1 was then vertically inserted into the matching slots on Substrate-3 so as to ensure precise alignment and stable positioning. In order to improve the overall mechanical stability of the array, polymethacrylate (PMI) rigid foams with a relative permittivity of

ε_r = 1.03–1.08 were placed between Substrate-3 and the GP, and also between the GP and the supporting plane. These foam inserts not only help maintain the structure's rigidity but also introduce minimal electrical impact, owing to their low dielectric constant.

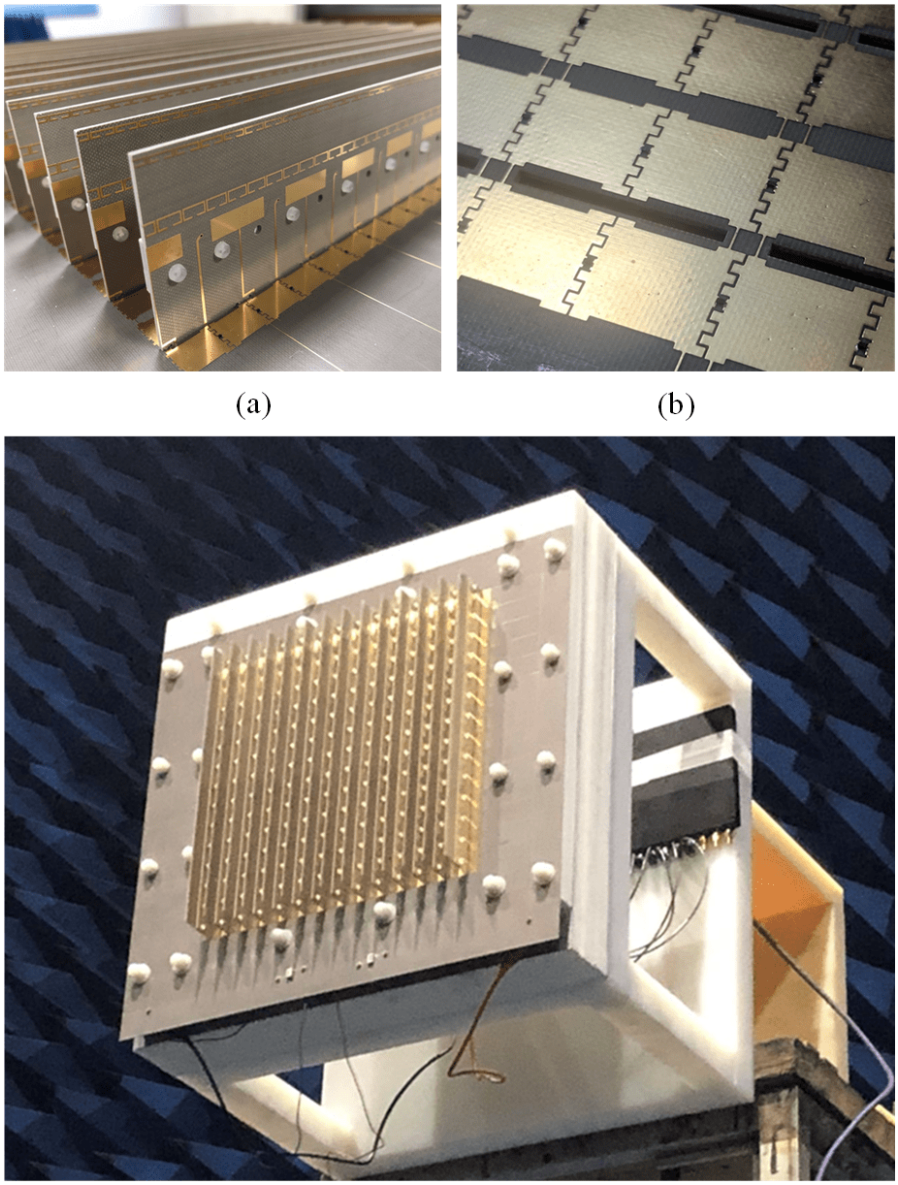

Figure 5.17: Prototype photos: (a) Array elements. (b) Reconfigurable layer. (c) Measurement setup in the chamber.

All active components on the reconfigurable layer were mounted using surface-mount

technology (SMT), enabling compact and reliable interconnections. The scattering parameters (S-parameters) of the array were measured with a Rohde & Schwarz ZVB20 Vector Network Analyzer, allowing accurate characterization of the array's input response over the full operational bandwidth. Moreover, the unit-excitation active element pattern (UEAEP) [92] of each element was measured in a far-field test environment, which comprised a Keysight (Agilent) N5183A MXG microwave analog signal generator and an N5264B PNA-X receiver. This measurement system facilitated precise beam characterization, providing insight into each element's fundamental radiation properties.

5.3.2 Measurement and Simulation Results

Figures 5.18(a)–(b) illustrate the measurement setup for evaluating the prototype array in the E-/H-planes and D-plane, respectively. In these diagrams, each cell represents a single array element. For the E-plane and H-plane measurements, a common 10×10 active-element aperture (shown in orange) was employed, while an 8×9 aperture (shown in cyan) was utilized for the D-plane measurements. The remaining (uncolored) elements functioned as passive elements intended to mitigate truncation effects that arise from finite array dimensions.

The active VSWR of the central element at coordinates $(7,7)$ was extracted by analyzing its measured reflection and transmission coefficients relative to every other element. During this procedure, all other ports were terminated with $50\,\Omega$ loads to ensure a realistic array environment. The following expression, taken from [40, 92], was employed to obtain the active reflection coefficient at a given scan angle (θ_0, ϕ_0):

$$\Gamma_{mn}\left(\theta_0,\phi_0\right) \approx \sum_{p=1}^{M}\sum_{q=1}^{N} s_{mn,pq} \exp\Big\{-j\left[(p-m)k\,d_x \sin\theta_0\cos\phi_0 + (q-n)k\,d_y \sin\theta_0 \sin\phi_0\right]\Big\}, \tag{5.1}$$

where $s_{mn,pq}$ is the transmission coefficient between elements mn and pq, M and

N are the total number of elements in the x- and y-directions, d_x and d_y are the inter-element spacings, and k is the free-space wavenumber.

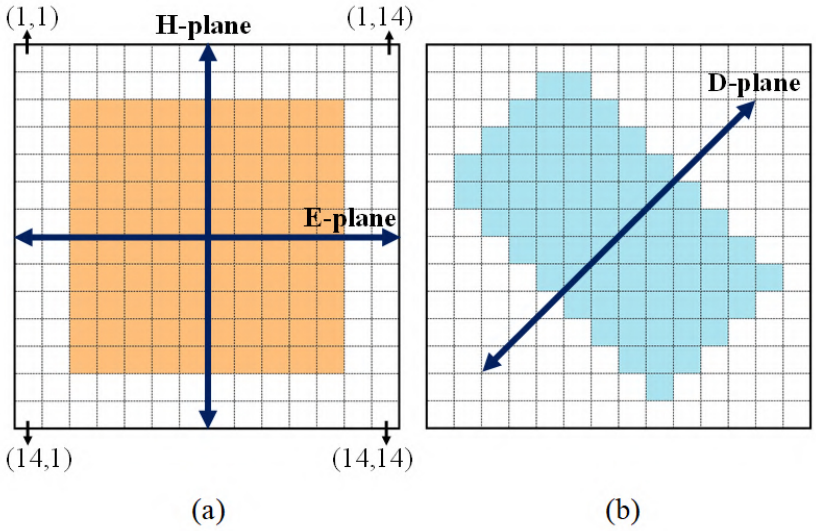

Figure 5.18: Active apertures used for pattern measurements. (a) E-/H-planes. (b) D-plane.

Figure 5.19 compares the simulated and measured active VSWRs in both the LS and HS. Under broadside conditions, the simulated VSWR curves show a combined total 15.8:1 bandwidth across 0.37–5.85 GHz, with a VSWR below 3. Specifically, the LS covers 0.37–0.93 GHz (2.51:1), whereas the HS spans 0.85–5.85 GHz (6.88:1). In terms of beam scanning, these two contiguous states jointly maintain a VSWR below 3 over a 13.7:1 bandwidth ranging from 0.42–5.77 GHz (LS: 0.42–0.93 GHz, HS: 0.90–5.77 GHz) for scan angles up to ±70° in the E-plane, ±70° in the D-plane, and ±50° in the H-plane. Notably, although most measured VSWR values remain below 3, a few narrow frequency regions approach 3.5. Moreover, in the LS, the measured responses drift marginally toward higher frequencies compared to the simulations. These slight deviations are attributed to the practical differences between the idealized infinite-array model in simulation and the actual finite-array implementation, as well as typical tolerances in manufacturing and assembly processes.

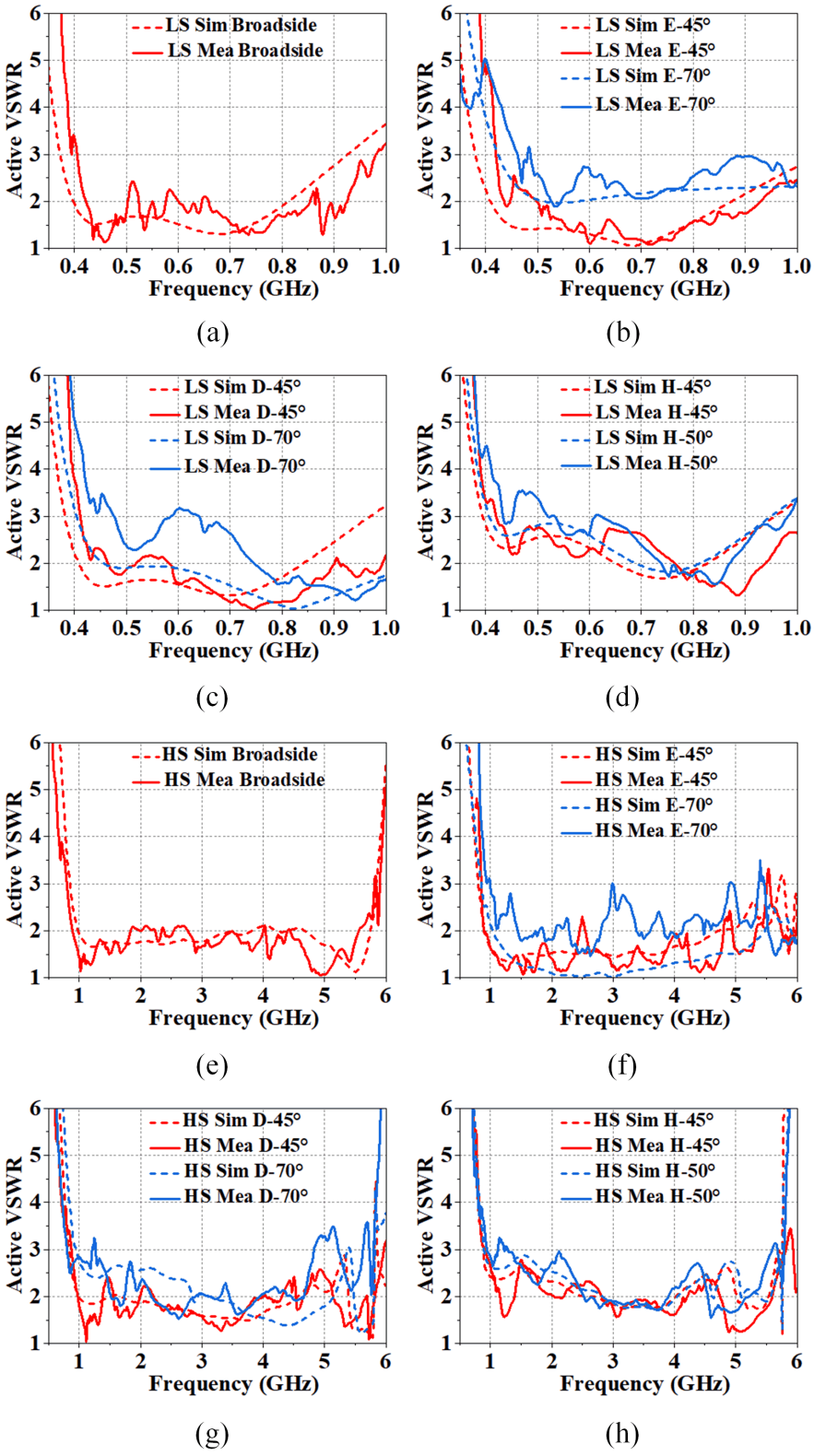

Figure 5.19: Simulated and measured active VSWR for broadside and various scans in the E-/D-/H-planes: (a)–(d) LS and (e)–(h) HS.

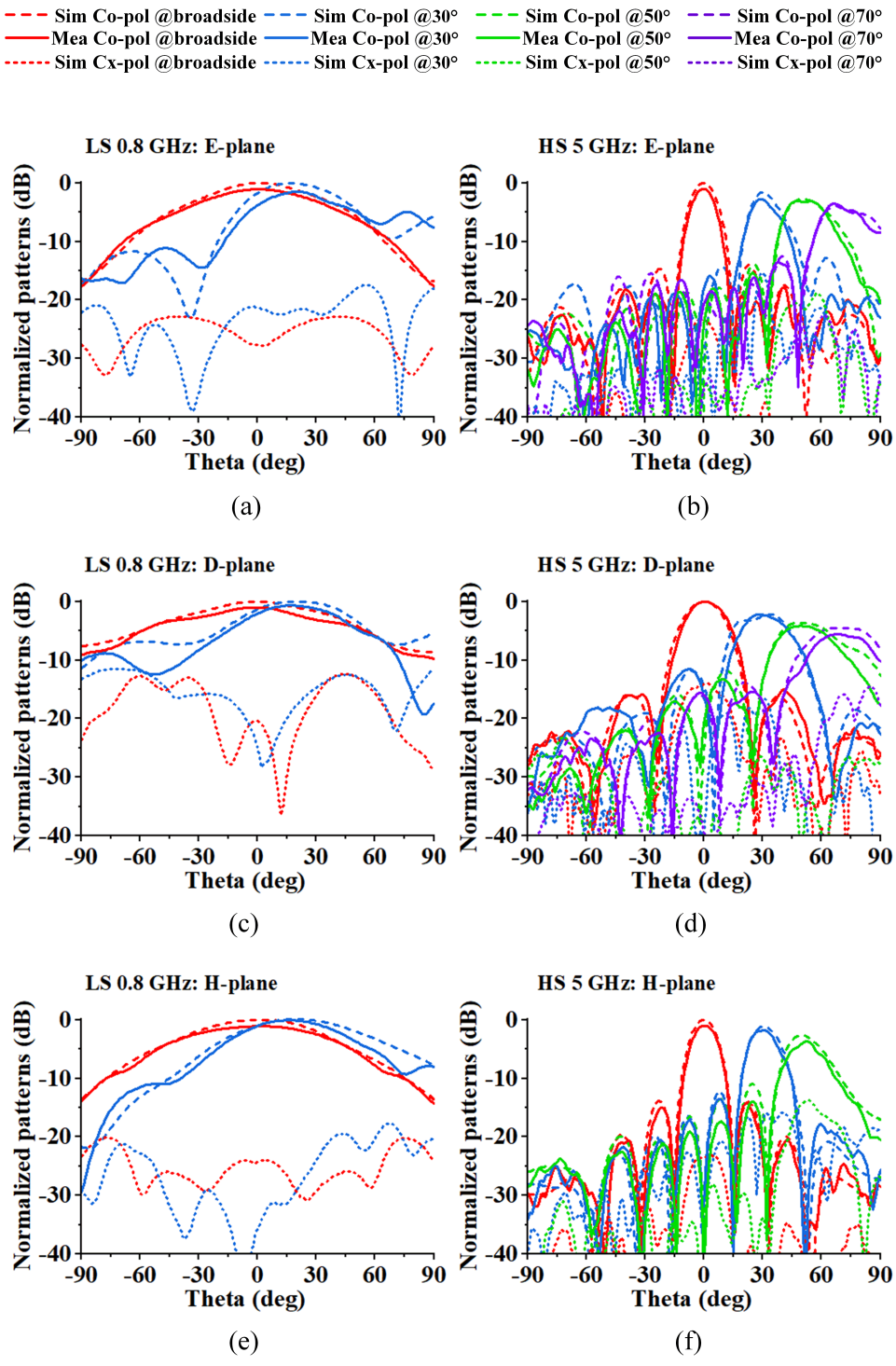

Figure 5.20: Simulated and measured scan patterns at (a),(c),(e) 0.8 GHz and (b),(d),(f) 5.0 GHz in the E-/D-/H-planes.

Figure 5.20 shows the simulated and measured co-polarization (Co-pol) and cross-

polarization (Cx-pol) radiation patterns in the E-/D-/H-planes at 0.8 GHz (LS) and 5.0 GHz (HS). In both frequency bands, the beam-scanned patterns exhibit a high degree of consistency between simulation and experiment. At 0.8 GHz, the maximum scan angle is restricted by the finite aperture size (only 0.587 wavelengths considering 0.8 GHz), limiting the achievable angular range. Sidelobe levels remain below −10 dB without any dedicated amplitude tapering. Cross-polarization levels are maintained below −15 dB over most scan angles, reaching a slightly higher value of −10.37 dB when scanning to 70° in the D-plane at 5.0 GHz. The D-plane beam is marginally wider than its E- or H-plane counterparts, primarily due to the reduced number of active elements along that direction.

Figure 5.21 further illustrates the close correlation between simulated and measured realized gains throughout the operating band. In particular, at lower frequencies within the LS (and near the low end of the HS), the measured gain slightly exceeds the nominal array aperture gain. This effect arises from the effectively enlarged aperture at lower frequencies, where the peripheral elements and the GP region augment the radiation through coupling mechanisms.

(a) (b)

Figure 5.21: Simulated and measured broadside gains in (a) LS and (b) HS.

5.3.3 Performance Comparison

Table 5.1 provides a side-by-side comparison of this array with other published designs, organized in ascending order of reported bandwidth. The first four entries (shaded) detail TCDAs confined to less than 10:1 bandwidth without extra bandwidth-expanding layers, while the fifth entry is a UWB Vivaldi array. The remaining references describe TCDAs that integrate various techniques to surpass the 10:1 bandwidth limit.

Table 5.1: Comparisons with Published UWB Beam-scanning Arrays

Ref.	Working band (GHz)/ Relative bandwidth	Maximum scanning angle			Minimum total efficiency (%)	Minimum radiation efficiency (%)	Extra bandwidth expanding structure	WAIM design	Profile
		E-plane	D-plane	H-plane					
[93]	3.13-11.63 / 3.7:1 (i)	75°, VSWR < 3.0	N.G.	60°, VSWR < 3.0	83.0	*98.5	None	FSS	$0.100\lambda_L$
[94]	0.69-2.88 / 4.1:1 (i)	45°, VSWR < 3.4	45°, VSWR < 3.4	45°, VSWR < 3.4	68.0	*97.8	None	Etched slots	$0.147\lambda_L$
[63]	0.8-4.38 / 5.5:1 (i)	70°, VSWR < 3.15	N.G.	55°, VSWR < 3.15	78.0	*89.1	None	Meta-surface	$0.088\lambda_L$
[90]	2.0-18.0 / 9.0:1 (i)	60°, VSWR < 4.0	60°, VSWR < 4.0	30°, VSWR < 4.0	70.0	*95.0	None	FSS	$0.102\lambda_L$
[42]	1.2-12.0 / 10:1 (i)	60°, VSWR < 3.25	N.G.	60°, VSWR < 3.25	N.G.	N.G.	None	None	$0.295\lambda_L$
[72]	0.2-2.0 / 10:1 (i)	60°, VSWR < 3.4	N.G.	60°, VSWR < 3.4	*18.9	45.0	Ferrite grids	Meta-surface	$0.087\lambda_L$
[56]	0.091-1.901 / 20.9:1 (i)	30°, VSWR < 2.5	30°, VSWR < 3.0	30°, VSWR < 3.5	*67.0	92.0	Polarization converting GP	None	$0.067\lambda_L$
[53]	0.28-5.91 / 21:1 (i)	N.G.	N.G.	N.G.	*48.0	73.0	Resistive FSS	Dielectric superstrate	$0.055\lambda_L$
[55]	0.13-6.0 / 46:1 (i)	60°, VSWR < 4.0	N.G.	60°, VSWR < 6.5	30.0	*41.1	Resistive FSS	FSS	$0.074\lambda_L$
This Work	0.42-5.77 / 13.7:1 (co2)	70°, VSWR < 3.0	70°, VSWR < 3.0	50°, VSWR < 3.0	70.0	95.0	Reconfigurable layer	DLDS-CLLs	$0.085\lambda_L$† $0.191\lambda_L$‡

N.G. represents Not Given.

(i) indicates instantaneous bandwidth; (co2) indicates combined overall bandwidth of its two contiguous operating bands.

The minimum radiation efficiency (total efficiency) values are calculated from the simulated total efficiency (radiation efficiency) and VSWR values obtained for the infinite array when its beam points in the broadside direction.

λ_L represents the wavelength of the lowest frequency in each work.

The developed array has two profiles of significance: $0.085\lambda_L$† is the height from its top to its GP; $0.191\lambda_L$‡ is the height from its top to its supporting plane.

Compared to arrays in [53, 55, 56, 72] that exceed 10:1 by employing additional lossy or polarization-converting structures, the design presented here achieves higher efficiency by avoiding large resistive losses. Although the bandwidth in [56] extends to 20.9:1 through polarization conversion, that method significantly compromises cross-

polarization levels and thus restricts usage to polarization-insensitive scenarios. In contrast, our array maintains efficiency comparable to TCDAs with narrower bandwidths (e.g., [63, 90, 93, 94]) that do not rely on lossy materials.

Beam-scanning capability is another critical metric. Compared to advanced arrays that apply bandwidth-expanding methods [53, 55, 56, 72] or the UWB Vivaldi in [42], the proposed array exhibits broader scanning angles and more favorable impedance matching at large scan angles. It supports scanning up to $\pm 70^\circ$ in both the E- and D-planes and $\pm 50^\circ$ in the H-plane, with VSWR below 3, exceeding or matching the best reported scanning ranges in the literature. Even when evaluated against arrays lacking extra bandwidth expansion, the proposed design achieves scanning angles and impedance performance that surpass or closely approximate those in [63, 90, 93, 94].

Although the full structure is $0.191\,\lambda_L$ in profile (owing to the extended balun), the height from the array's top to the GP is only $0.085\,\lambda_L$, which is similar or smaller than that of several TCDAs reported in [53, 55, 56, 63, 72, 90, 93, 94], and remains below that of the Vivaldi array in [42]. Additional meandering or other feeding-line modifications [63, 95] could shorten the balun further, though that aspect was not the main focus of this study.

Moreover, rather than providing one instantaneous ultrawide band, the proposed array furnishes two contiguous wide bands. Each state achieves high radiation efficiency. Such a design is well-suited for multi-function systems performing, for instance, foliage penetration (FOPEN) imaging in the lower band, or air-traffic control, weather monitoring, and multi-band satellite/mobile communications in the higher band [96, 97]. These extended contiguous bands also accommodate wider-spectrum sensing applications [98].

5.4 Conclusion

This chapter presents an innovative UWB frequency-reconfigurable tightly-coupled dipole array (FR-TCDA) that offers high radiation efficiency and a wide beam-scanning capability. In contrast to previous TCDAs that incorporate highly lossy media to achieve bandwidth extension, the proposed array leverages a reconfigurable layer to control the GP reflection phase across two states, each maintaining VSWR < 3 and efficiency exceeding 95%. It spans 0.37–0.93 GHz when the reconfigurable layer is in the off-state and 0.85–5.85 GHz when it is in the on-state, resulting in a total bandwidth of 15.8:1 at broadside. By employing a custom DLDS-CLLs-based WAIM design and a specialized feeding approach (Klopfenstein balun with a capacitance-loaded shorting pin), the array supports scanning angles up to $\{\pm 70^\circ, \pm 70^\circ, \pm 50^\circ\}$ in the E-/D-/H-planes, maintaining a combined bandwidth of 13.7:1 between 0.42–5.77 GHz with its two states. A 14×14 prototype was constructed and tested, confirming the simulated performance. This work thus offers a promising solution for multi-octave UWB applications requiring both high efficiency and broad scanning coverage.

CHAPTER 6

CONCLUSION AND FUTURE WORK

6.1 Summary of Contributions

This dissertation proposes innovative solutions for multi-band and UWB antenna arrays, addressing critical challenges in modern wireless communication systems. The research progresses from cross-band interference mitigation in multi-band arrays to UWB antenna array performance enhancement, with each chapter building on the previous work. The key contributions are summarized below.

6.1.1 Multi-Band Shared-Aperture Antenna Array Based on Embedded Scheme (Chapter 3)

- **Wideband cross-band scattering suppression:** Unique helical filters are introduced to effectively mitigate wideband scattering, achieving an impressive de-scattering bandwidth of 66.7% (1.36–2.72 GHz).
- **Enhanced in-band isolation:** The insertion of the helical filters extends current

paths and enables a miniaturized LB aperture, facilitating enhanced in-band isolation with fixed element spacing.

- **Improved LB impedance matching performance:** The integration of innovative LC-circuit-load LB baluns effectively improved impedance matching performance in the LB (0.8–0.96 GHz).

6.1.2 Multi-Band Shared-Aperture Antenna Array Based on a New Buffering Scheme (Chapter 4)

- **Exceptionally low-profile configuration:** Enabled by the TCBL, the LB antenna achieves a profile of $0.087\lambda_L$, significantly reducing array height compared to traditional shared-aperture array solutions.

- **Enhanced LB and HB impedance matching performance:** Unlike traditional methods that degrade impedance matching, the TCBL compensates the inductance in the LB and adds a new resonance in the HB, enabling wideband operation of 32.7% (0.69–0.96 GHz) in the LB and 59.0% (1.47–2.7 GHz) in the HB.

- **Inherently suppressed cross-band interference:** The low-profile LB design reduces blockage effects on nearby HB elements, alleviating cross-band scattering. Additionally, the TCBL acts as an "electromagnetic buffer," trapping coupled energy and blocking its transfer to cross-band ports, effectively suppressing cross-band coupling.

6.1.3 UWB Tightly Coupled Dipole Array (Chapter 5)

- **UWB operational bandwidth with adaptive reconfigurability:** The array achieves a remarkable 15.8:1 bandwidth (0.37–5.85 GHz) through two reconfigurable states, covering multiple communication bands with a single array aperture.

- **High radiation efficiency:** The design maintains an efficiency of over 95%, ensuring minimal power loss.
- **Wide-angle beam scanning:** The innovative DLDS-CLLs enable the array to support beam scanning up to $\{\pm 70°, \pm 70°, \pm 50°\}$ in the {E-, D-, H-}planes with VSWR < 3 over both states, demonstrating enhanced scanning performance.
- **Effective UWB feeding with bad resonances tuning:** The design incorporates a specialized tapered balun integrated with a capacitance-loaded shorting pin, enabling effective feeding without undesired resonances.

6.1.4 Key Observations and Insights

The research presented in this dissertation highlights the progression from cross-band interference mitigation in multi-band arrays to UWB performance enhancement. The three chapters are interconnected, with each building on the previous work to address increasingly complex challenges:

- **Chapter 3** focused on cross-band interference mitigation in existing multi-band array schemes, introducing helical filters and LC-loaded baluns to achieve suppression of cross-band scattering and wideband operation. This work laid the foundation for the development of more advanced array designs.
- **Chapter 4** introduced a new buffering scheme for multi-band antenna arrays that inherently suppressed cross-band interference without relying on complex filtering structures. The TCBL offers three key advantages: reducing the array's profile, enhancing dual-band impedance matching performance, and suppressing cross-band interference, demonstrating a significant improvement over traditional multi-band array designs.

- **Chapter 5** advanced the research by addressing UWB challenges, specifically focusing on bandwidth extension with high-radiation efficiency and wide-angle beam scanning. The FR-TCDA achieved unprecedented bandwidth and efficiency, leveraging the principles of coupling, impedance matching, and resonance tuning techniques.

6.2 Future Work

While this dissertation has provided substantial contributions, several avenues remain open for further research and exploration:

- **Advanced Synthesis Methods:** Future research can leverage AI-assisted optimization techniques to expedite the design process, particularly for large-scale arrays where balancing bandwidth, isolation, profile, and cost is critical. Additionally, multi-objective optimization algorithms may be developed to simultaneously enhance metrics such as radiation efficiency, beam-scanning range, and cross-band isolation.

- **Structural and Environmental Considerations:** Investigating advanced materials with improved dielectric and conductive properties could enhance both electromagnetic performance and thermal stability. Furthermore, ensuring environmental robustness under varying conditions such as temperature fluctuations, humidity, and mechanical stress is crucial for long-term reliability.

- **Reconfigurable and Adaptive Technologies:** Future antenna systems could benefit from polarization-reconfigurable designs to enhance adaptability in dynamically changing communication environments. Similarly, real-time beam control and adaptive beamforming could significantly improve system-level performance, particularly for high-speed mobile and satellite applications.

- **Industry Applications and Large-Scale Deployment:** Research should also focus on scalability and cost-effective manufacturing, including 3D printing and flexible circuit technologies, to enable mass production. Additionally, the proposed antenna solutions can be further optimized for 6G networks, supporting URLLC and massive multiple-input and multiple-output (MIMO) applications.

6.3 Final Remarks

This dissertation has introduced and validated innovative multi-band and UWB antenna array solutions to address key challenges such as bandwidth limitations, cross-band interference, and beam-scanning constraints. The findings contribute to:

- **Design advancements:** The proposed methods offer new approaches for designing compact, broadband, and high-efficiency antenna arrays.
- **Practical engineering solutions:** The research provides scalable and manufacturable antenna designs that can be integrated into modern wireless infrastructure.
- **Future research directions:** The insights gained from this work serve as a foundation for further exploration of adaptive, high-performance, and intelligent antenna technologies.

The proposed solutions offer broad applicability across modern wireless infrastructure, ranging from base stations to next-generation antenna array systems that demand robust performance under compact spatial constraints. By leveraging innovative filtering, coupling, and resonance-tuning techniques, this research has opened new paths for designing multi-band/UWB platforms with high data rates, enhanced isolation, extended signal coverage, and compact form factors. These innovations are expected to contribute

to the ongoing refinement of array design methodologies, facilitating the realization of high-performance antenna systems for future wireless communication applications.

BIBLIOGRAPHY

[1] H.-H. Sun, C. Ding, H. Zhu, B. Jones, and Y. J. Guo, "Suppression of Cross-Band Scattering in Multiband Antenna Arrays," *IEEE Transactions on Antennas and Propagation*, vol. 67, pp. 2379–2389, Apr. 2019.

[2] Y. J. Guo, *Advanced Antenna Array Engineering for 6G and beyond Wireless Communications*.
Hoboken, New Jersey: Wiley-IEEE Press, John Wiley & Sons, Inc., 2022.

[3] H.-H. Sun, H. Zhu, C. Ding, B. Jones, and Y. J. Guo, "Scattering Suppression in a 4G and 5G Base Station Antenna Array Using Spiral Chokes," *IEEE Antennas and Wireless Propagation Letters*, vol. 19, pp. 1818–1822, Oct. 2020.

[4] H.-H. Sun, B. Jones, Y. J. Guo, and Y. H. Lee, "Suppression of Cross-Band Scattering in Interleaved Dual-Band Cellular Base-Station Antenna Arrays," *IEEE access : practical innovations, open solutions*, vol. 8, pp. 222486–222495, 2020.

[5] W. Niu, B. Sun, G. Zhou, and Z. Lan, "Dual-Band Aperture Shared Antenna Array With Decreased Radiation Pattern Distortion," *IEEE Transactions on Antennas and Propagation*, vol. 70, pp. 6048–6053, July 2022.

[6] Y.-L. Chang and Q.-X. Chu, "Suppression of Cross-Band Coupling Interference in Tri-Band Shared-Aperture Base Station Antenna," *IEEE Transactions on Antennas and Propagation*, vol. 70, pp. 4200–4214, June 2022.

[7] Y.-S. Wu, Q.-X. Chu, and H.-Y. Huang, "Electromagnetic Transparent Antenna With Slot-Loaded Patch Dipoles in Dual-Band Array," *IEEE Transactions on Antennas and Propagation*, vol. 70, pp. 7989–7998, Sept. 2022.

[8] Q.-X. Chu, Y.-S. Wu, and Y.-L. Chang, "A Novel Electromagnetic Transparent Antenna in Dual-Band Shared-Aperture Array," *IEEE Transactions on Antennas and Propagation*, vol. 70, pp. 9894–9899, Oct. 2022.

[9] Y.-L. Chang and Q.-X. Chu, "Broadband Dual-Polarized Electromagnetic Transparent Antenna for Cross-Band Scattering Suppression," *IEEE Antennas and Wireless Propagation Letters*, vol. 21, pp. 1452–1456, July 2022.

[10] F. Jia, Z. Zheng, Q. Wang, P. Liu, S. Liao, W. Che, and Q. Xue, "A New Multi-Band Multi-Array Antenna Configuration With Scattering Suppression for Radiation Pattern Distortion Mitigation of Base Station," *IEEE Transactions on Antennas and Propagation*, vol. 70, pp. 6006–6011, July 2022.

[11] Y. He, W. Huang, Z. He, L. Zhang, X. Gao, and Z. Zeng, "A Novel Cross-Band Decoupled Shared-Aperture Base Station Antenna Array Unit for 5G Mobile Communications," *IEEE Open Journal of Antennas and Propagation*, vol. 3, pp. 583–593, 2022.

[12] R. Wu, J.-H. Lin, F.-C. Chen, and L. H. Ye, "Dual-Broadband Aperture-Shared Base Station Antenna Array Using Double Decoupling Techniques," *IEEE Antennas and Wireless Propagation Letters*, pp. 1–5, 2024.

[13] S. -Y. Sun, C. Ding, W. Jiang, and Y. J. Guo, "Simultaneous Suppression of Cross-Band Scattering and Coupling Between Closely Spaced Dual-Band Dual-Polarized Antennas," *IEEE Transactions on Antennas and Propagation*, vol. 71, pp. 6423–6434, Aug. 2023.

[14] J. H. Zhai, Y. F. Cao, Q. Xue, and W. Che, "Cross-Band Decoupling Method for Dual-Band Aperture-Shared Antenna Array Using Metasurfaces," *IEEE Transactions on Antennas and Propagation*, vol. 72, pp. 2001–2006, Feb. 2024.

[15] F. Du, Y. Cao, X. Xiu, W. Che, and Q. Xue, "Compact Dual-Band Shared-Aperture Base-Station Antenna Array Using Transparent Wideband Absorbing Metasurface and Radiator-Reused Scheme," *IEEE Transactions on Antennas and Propagation*, vol. 72, pp. 2502–2512, Mar. 2024.

[16] D. He, Q. Yu, Y. Chen, and S. Yang, "Dual-Band Shared-Aperture Base Station Antenna Array With Electromagnetic Transparent Antenna Elements," *IEEE Transactions on Antennas and Propagation*, vol. 69, pp. 5596–5606, Sept. 2021.

[17] G.-N. Zhou, B.-H. Sun, Q.-Y. Liang, S.-T. Wu, Y.-H. Yang, and Y.-M. Cai, "Triband Dual-Polarized Shared-Aperture Antenna for 2G/3G/4G/5G Base Station Applications," *IEEE Transactions on Antennas and Propagation*, vol. 69, pp. 97–108, Jan. 2021.

[18] S. J. Yang, Y. Yang, and X. Y. Zhang, "Low Scattering Element-Based Aperture-Shared Array for Multiband Base Stations," *IEEE Transactions on Antennas and Propagation*, vol. 69, pp. 8315–8324, Dec. 2021.

[19] J. Tao, P. Tang, H. Yang, D. Liao, L. Jing, E.-P. Li, H. Chen, and Z. Wang, "Design of Electromagnetic Transparent Antennas Based on Drude Metasurface for High-Band Compatibility," *IEEE Transactions on Antennas and Propagation*, vol. 72, pp. 4911–4919, June 2024.

[20] Y. He, W. Tian, and L. Zhang, "A Novel Dual-Broadband Dual-Polarized Electrical Downtilt Base Station Antenna for 2G/3G Applications," *IEEE access : practical innovations, open solutions*, vol. 5, pp. 15241–15249, 2017.

[21] Y. He, Z. Pan, X. Cheng, Y. He, J. Qiao, and M. M. Tentzeris, "A Novel Dual-Band, Dual-Polarized, Miniaturized and Low-Profile Base Station Antenna," *IEEE Transactions on Antennas and Propagation*, vol. 63, pp. 5399–5408, Dec. 2015.

[22] H. Huang, Y. Liu, and S. Gong, "A Novel Dual-Broadband and Dual-Polarized Antenna for 2G/3G/LTE Base Stations," *IEEE Transactions on Antennas and Propagation*, vol. 64, pp. 4113–4118, Sept. 2016.

[23] R. Wu and Q.-X. Chu, "A Compact, Dual-Polarized Multiband Array for 2G/3G/4G Base Stations," *IEEE Transactions on Antennas and Propagation*, vol. 67, pp. 2298–2304, Apr. 2019.

[24] X.-H. Ding, J.-Y. Yang, W.-W. Yang, and J.-X. Chen, "Compact Dual-Band and Dual-Polarized Base Station Antenna With Shared-Dipole Elements," *IEEE Antennas and Wireless Propagation Letters*, vol. 22, pp. 1371–1375, June 2023.

[25] Y. Chen, J. Zhao, and S. Yang, "A Novel Stacked Antenna Configuration and its Applications in Dual-Band Shared-Aperture Base Station Antenna Array Designs," *IEEE Transactions on Antennas and Propagation*, vol. 67, pp. 7234–7241, Dec. 2019.

[26] Y. Zhu, Y. Chen, and S. Yang, "Decoupling and Low-Profile Design of Dual-Band Dual-Polarized Base Station Antennas Using Frequency-Selective Surface," *IEEE Transactions on Antennas and Propagation*, vol. 67, pp. 5272–5281, Aug. 2019.

[27] Y. Zhu, Y. Chen, and S. Yang, "Helical Torsion Coaxial Cable for Dual-Band Shared-Aperture Antenna Array Decoupling," *IEEE Transactions on Antennas and Propagation*, vol. 68, pp. 6128–6135, Aug. 2020.

[28] Y. Zhu, Y. Chen, and S. Yang, "Cross-Band Mutual Coupling Reduction in Dual-Band Base-Station Antennas With a Novel Grid Frequency Selective Surface," *IEEE Transactions on Antennas and Propagation*, vol. 69, pp. 8991–8996, Dec. 2021.

[29] R. Chao Dai, S. Sun, H. Su, and X. Y. Zhang, "Analysis and Design of Dual-Modal Filtenna for Dismountable Aperture-Shared Array," *IEEE Transactions on Antennas and Propagation*, vol. 72, pp. 4806–4817, June 2024.

[30] Y. Li and Q.-X. Chu, "Coplanar Dual-Band Base Station Antenna Array Using Concept of Cavity-Backed Antennas," *IEEE Transactions on Antennas and Propagation*, vol. 69, pp. 7343–7354, Nov. 2021.

[31] Y. Li and Q.-X. Chu, "Shared-Radiator Design of Dual-Band Coplanar Base Station Antenna Array Using Cavity-Backed Slots," *IEEE Transactions on Antennas and Propagation*, vol. 69, pp. 8985–8990, Dec. 2021.

[32] R. J. Mailloux, *Phased Array Antenna Handbook*.
Artech house, 2017.

[33] J. Dyson, "The equiangular spiral antenna," *IRE Transactions on Antennas and Propagation*, vol. 7, pp. 181–187, Apr. 1959.

[34] J. Kraus, "Helical Beam Antennas for Wide-Band Applications," *Proceedings of the IRE*, vol. 36, pp. 1236–1242, Oct. 1948.

[35] R. DuHamel and D. Isbell, "Broadband logarithmically periodic antenna structures," in *IRE International Convention Record*, vol. 5, (New York, NY, USA), pp. 119–128, Institute of Electrical and Electronics Engineers, 1957.

[36] Tan-Huat Chio and D. Schaubert, "Parameter study and design of wide-band wide-scan dual-polarized tapered slot antenna arrays," *IEEE Transactions on Antennas and Propagation*, vol. 48, pp. 879–886, June 2000.

[37] P. Gibson, "The vivaldi aerial," in *1979 9th European Microwave Conference*, (Brighton, UK), pp. 101–105, IEEE, Sept. 1979.

[38] Joon Shin and D. Schaubert, "A parameter study of stripline-fed vivaldi notch-antenna arrays," *IEEE Transactions on Antennas and Propagation*, vol. 47, pp. 879–886, May 1999.

[39] D. Schaubert, S. Kasturi, A. Boryssenko, and W. Elsallal, "Vivaldi antenna arrays for wide bandwidth and electronic scanning," in *2nd European Conference on Antennas and Propagation (EuCAP 2007)*, (Edinburgh, UK), pp. 211–211, Institution of Engineering and Technology, 2007.

[40] M. N. Vouvakis, D. H. Schaubert, and F. B. Gross, "Vivaldi antenna arrays," in *Frontiers in Antennas: Next Generation Design & Engineering*, McGraw-Hill New York, NY, USA, 2011.

[41] R. Kindt and D. Taylor, "Polarization correction in dual-polarized phased arrays of flared notches," in *2011 IEEE International Symposium on Antennas and Propagation (APSURSI)*, pp. 1961–1964, 2011-07-03/2011-07-08.

[42] J. T. Logan, R. W. Kindt, and M. N. Vouvakis, "A 1.2–12 GHz Sliced Notch Antenna Array," *IEEE Transactions on Antennas and Propagation*, vol. 66, pp. 1818–1826, Apr. 2018.

[43] J. T. Logan, R. W. Kindt, and M. N. Vouvakis, "Low Cross-Polarization Vivaldi Arrays," *IEEE Transactions on Antennas and Propagation*, vol. 66, pp. 1827–1837, Apr. 2018.

[44] H. Wheeler, "The Radiation Resistance of an Antenna in an Infinite Array or Waveguide," *Proceedings of the IRE*, vol. 36, pp. 478–487, Apr. 1948.

[45] H. Wheeler, "Simple relations derived fom a phased-array antenna made of an infinite current sheet," *IEEE Transactions on Antennas and Propagation*, vol. 13, pp. 506–514, July 1965.

[46] B. Munk, R. Taylor, T. Durharn, W. Croswell, B. Pigon, R. Boozer, S. Brown, M. Jones, J. Pryor, S. Ortiz, J. Rawnick, K. Krebs, M. Vanstrum, G. Gothard, and D. Wiebelt, "A low-profile broadband phased array antenna," in *IEEE Antennas and Propagation Society International Symposium. Digest. Held in Conjunction with: USNC/CNC/URSI North American Radio Sci. Meeting (Cat. No.03CH37450)*, vol. 2, pp. 448–451 vol.2, June 2003.

[47] B. A. Munk, "Broadband Wire Arrays," in *Finite Antenna Arrays and FSS*, pp. 181–213, Hoboken, NJ, USA: John Wiley & Sons, Inc., Jan. 2005.

[48] R. C. Hansen, *Phased Array Antennas*.
John Wiley & Sons, Nov. 2009.

[49] M. Jones and J. Rawnick, "A new approach to broadband array design using tightly coupled elements," in *MILCOM 2007-IEEE Military Communications Conference*, pp. 1–7, IEEE, 2007.

[50] J. Doane, K. Sertel, and J. Volakis, "Bandwidth limits for lossless planar arrays over ground plane," *Electronics Letters*, vol. 48, no. 10, p. 540, 2012.

[51] I. Tzanidis, K. Sertel, and J. L. Volakis, "Interwoven spiral array (ISPA) with a 10: 1 bandwidth on a ground plane," *IEEE Antennas and Wireless Propagation Letters*, vol. 10, pp. 115–118, 2010.

[52] J. L. Volakis and K. Sertel, "Narrowband and wideband metamaterial antennas based on degenerate band edge and magnetic photonic crystals," *Proceedings of the IEEE*, vol. 99, no. 10, pp. 1732–1745, 2011.

[53] W. F. Moulder, K. Sertel, and J. L. Volakis, "Superstrate-Enhanced Ultrawideband Tightly Coupled Array With Resistive FSS," *IEEE Transactions on Antennas and Propagation*, vol. 60, pp. 4166–4172, Sept. 2012.

[54] W. F. Moulder, K. Sertel, and J. L. Volakis, "Ultrawideband Superstrate-Enhanced Substrate-Loaded Array With Integrated Feed," *IEEE Transactions on Antennas and Propagation*, vol. 61, pp. 5802–5807, Nov. 2013.

[55] A. D. Johnson, J. Zhong, S. B. Venkatakrishnan, E. A. Alwan, and J. L. Volakis, "Phased Array With Low-Angle Scanning and 46:1 Bandwidth," *IEEE Transactions on Antennas and Propagation*, vol. 68, pp. 7833–7841, Dec. 2020.

[56] S. Kim and S. Nam, "Characteristics of TCDA With Polarization Converting Ground Plane," *IEEE Transactions on Antennas and Propagation*, vol. 69, pp. 2359–2364, Apr. 2021.

[57] P.-S. Kildal, *Foundations of Antenna Engineering: A Unified Approach for Line-of-Sight and Multipath*.
Artech House, June 2015.

[58] E. Magill and H. Wheeler, "Wide-angle impedance matching of a planar array antenna by a dielectric sheet," *IEEE Transactions on Antennas and Propagation*, vol. 14, no. 1, pp. 49–53, 1966.

[59] S. S. Holland, D. H. Schaubert, and M. N. Vouvakis, "A 7–21 GHz Dual-Polarized Planar Ultrawideband Modular Antenna (PUMA) Array," *IEEE Transactions on Antennas and Propagation*, vol. 60, pp. 4589–4600, Oct. 2012.

[60] J. T. Logan, R. W. Kindt, M. Y. Lee, and M. N. Vouvakis, "A New Class of Planar Ultrawideband Modular Antenna Arrays With Improved Bandwidth," *IEEE Transactions on Antennas and Propagation*, vol. 66, pp. 692–701, Feb. 2018.

[61] E. Yetisir, N. Ghalichechian, and J. L. Volakis, "Ultrawideband Array With 70° Scanning Using FSS Superstrate," *IEEE Transactions on Antennas and Propagation*, vol. 64, pp. 4256–4265, Oct. 2016.

[62] A. O. Bah, P.-Y. Qin, R. W. Ziolkowski, Q. Cheng, and Y. J. Guo, "Realization of an Ultra-thin Metasurface to Facilitate Wide Bandwidth, Wide Angle Beam Scanning," *Scientific Reports*, vol. 8, p. 4761, Mar. 2018.

[63] A. O. Bah, P.-Y. Qin, R. W. Ziolkowski, Y. J. Guo, and T. S. Bird, "A Wideband Low-Profile Tightly Coupled Antenna Array With a Very High Figure of Merit," *IEEE Transactions on Antennas and Propagation*, vol. 67, pp. 2332–2343, Apr. 2019.

[64] B. Wang, S. Yang, Y. Chen, S. Qu, and J. Hu, "Low Cross-Polarization Ultrawideband Tightly Coupled Balanced Antipodal Dipole Array," *IEEE Transactions on Antennas and Propagation*, vol. 68, pp. 4479–4488, June 2020.

[65] Z. Jiang, S. Xiao, and B.-Z. Wang, "A Low-Cost Light-Weight Ultrawideband Wide-Angle Scanning Tightly Coupled Dipole Array Loaded With Multilayer Metallic Strips," *IEEE Access*, vol. 9, pp. 24975–24983, 2021.

[66] H. Zhang, S. Yang, S. Xiao, Y. Chen, and S. Qu, "Low-Profile, Lightweight, Ultra-Wideband Tightly Coupled Dipole Arrays Loaded With Split Rings," *IEEE Transactions on Antennas and Propagation*, vol. 67, pp. 4257–4262, June 2019.

[67] D. Cavallo, A. Neto, and G. Gerini, "PCB Slot Based Transformers to Avoid Common-Mode Resonances in Connected Arrays of Dipoles," *IEEE Transactions on Antennas and Propagation*, vol. 58, pp. 2767–2771, Aug. 2010.

[68] J. Gilmore and D. B. Davidson, "Suppressing Undesired Common-Mode Resonances in Connected Antenna Arrays," *IEEE Transactions on Antennas and Propagation*, vol. 63, pp. 5245–5250, Nov. 2015.

[69] S. S. Holland and M. N. Vouvakis, "The Planar Ultrawideband Modular Antenna (PUMA) Array," *IEEE Transactions on Antennas and Propagation*, vol. 60, pp. 130–140, Jan. 2012.

[70] D.-M. Sun, Z.-C. Hao, C.-Y. Ding, R.-J. Liu, Z.-J. Guo, and H.-Y. Yin, "A Low-Profile Ultra-Wideband and Wide-Scanning Phased Array for UHF Applications," *IEEE Transactions on Antennas and Propagation*, vol. 71, pp. 473–486, Jan. 2023.

[71] D. Cavallo, A. Neto, and G. Gerini, "Common-mode resonances in ultra wide band connected arrays of dipoles: Measurements from the demonstrator and exit strategy," in *2009 International Conference on Electromagnetics in Advanced Applications*, (Torino, Italy), pp. 435–438, IEEE, Sept. 2009.

[72] B. Wang, S. Yang, Z. Zhang, Y. Chen, S. Qu, and J. Hu, "A Ferrite-Loaded Ultralow Profile Ultrawideband Tightly Coupled Dipole Array," *IEEE Transactions on Antennas and Propagation*, vol. 70, pp. 1965–1975, Mar. 2022.

[73] B. Schiek and J. Kohler, "An improved microstrip-to-microslot transition," *IEEE Transactions on Microwave Theory and Techniques*, vol. 24, no. 4, pp. 231–233, 1976.

[74] J. P. Doane, K. Sertel, and J. L. Volakis, "A Wideband, Wide Scanning Tightly Coupled Dipole Array With Integrated Balun (TCDA-IB)," *IEEE Transactions on Antennas and Propagation*, vol. 61, pp. 4538–4548, Sept. 2013.

[75] A. O. Bah, Pei-Yuan Qin, and Y. J. Guo, "An extremely wideband tapered balun for application in tightly coupled arrays," in *2016 IEEE-APS Topical Conference*

on Antennas and Propagation in Wireless Communications (APWC), (Cairns, Australia), pp. 162–165, IEEE, Sept. 2016.

[76] R. Klopfenstein, "A Transmission Line Taper of Improved Design," *Proceedings of the IRE*, vol. 44, pp. 31–35, Jan. 1956.

[77] M. Carvalho, A. D. Johnson, E. A. Alwan, and J. L. Volakis, "Semi-Resistive Approach for Tightly Coupled Dipole Array Bandwidth Enhancement," *IEEE Open Journal of Antennas and Propagation*, vol. 2, pp. 110–117, 2021.

[78] Q. Zhang and Y. Gao, "A Compact Broadband Dual-Polarized Antenna Array for Base Stations," *IEEE Antennas and Wireless Propagation Letters*, vol. 17, pp. 1073–1076, June 2018.

[79] L. Wu, R. Li, Y. Qin, and Y. Cui, "Bandwidth-Enhanced Broadband Dual-Polarized Antennas for 2G/3G/4G and IMT Services," *IEEE Antennas and Wireless Propagation Letters*, vol. 17, pp. 1702–1706, Sept. 2018.

[80] L. H. Ye, X. Y. Zhang, Y. Gao, and Q. Xue, "Wideband Dual-Polarized Four-Folded-Dipole Antenna Array With Stable Radiation Pattern for Base-Station Applications," *IEEE Transactions on Antennas and Propagation*, vol. 68, pp. 4428–4436, June 2020.

[81] Y. Qin, R. Li, Q. Xue, X. Zhang, and Y. Cui, "Aperture-Shared Dual-Band Antennas With Partially Reflecting Surfaces for Base-Station Applications," *IEEE Transactions on Antennas and Propagation*, vol. 70, pp. 3195–3207, May 2022.

[82] L. Y. Nie, X. Q. Lin, Y. J. Chen, J. Zhang, B. Wang, Z. Q. Yang, and Y. Fan, "A Low-Profile Coplanar Dual-Polarized and Dual-Band Base Station Antenna Array," *IEEE Transactions on Antennas and Propagation*, vol. 66, pp. 6921–6929, Dec. 2018.

[83] Y. He, C. Ding, C. Chang, G. Wei, and Y. J. Guo, "A Bowl-Shaped Filtering Antenna With Wideband Cross-Band Scattering Mitigation for Dual-Band Base Stations," *IEEE Transactions on Antennas and Propagation*, vol. 72, pp. 6723–6728, Aug. 2024.

[84] W. Fan, A. Lu, L. Wai, and B. Lok, "Mixed-mode S-parameter characterization of differential structures," in *Proceedings of the 5th Electronics Packaging Technology Conference (EPTC 2003)*, (Singapore), pp. 533–537, IEEE, 2003.

[85] C. Ding, H. Sun, R. W. Ziolkowski, and Y. J. Guo, "Simplified Tightly-Coupled Cross-Dipole Arrangement for Base Station Applications," *IEEE access : practical innovations, open solutions*, vol. 5, pp. 27491–27503, 2017.

[86] Y. F. Cao, X. Y. Zhang, and Q. Xue, "Compact Shared-Aperture Dual-Band Dual-Polarized Array Using Filtering Slot Antenna and Dual-Function Metasurface," *IEEE Transactions on Antennas and Propagation*, vol. 70, pp. 1120–1131, Feb. 2022.

[87] C. A. Balanis, *Modern Antenna Handbook*.
John Wiley & Sons, Sept. 2011.

[88] R. J. Mailloux, *Phased Array Antenna Handbook*.
Artech House Antennas and Propagation Library, Norwood, Massachusetts: Artech House, third edition. ed., 2018.

[89] B. A. Munk, *Finite Antenna Arrays and FSS*.
John Wiley & Sons, July 2003.

[90] J. Zhong, A. Johnson, E. A. Alwan, and J. L. Volakis, "Dual-Linear Polarized Phased Array With 9:1 Bandwidth and 60° Scanning Off Broadside," *IEEE Transactions on Antennas and Propagation*, vol. 67, pp. 1996–2001, Mar. 2019.

[91] C.-H. Hu, B.-Z. Wang, G.-F. Gao, R. Wang, S.-Q. Xiao, and X. Ding, "Conjugate Impedance Matching Method for Wideband and Wide-Angle Impedance Matching Layer With 70° Scanning in the H-Plane," *IEEE Antennas and Wireless Propagation Letters*, vol. 20, pp. 63–67, Jan. 2021.

[92] D. Kelley and W. Stutzman, "Array antenna pattern modeling methods that include mutual coupling effects," *IEEE Transactions on Antennas and Propagation*, vol. 41, pp. 1625–1632, Dec. 1993.

[93] Z. Jiang, S. Xiao, Z. Yao, and B.-Z. Wang, "A Planar Ultrawideband Wide-Angle Scanning Array Loaded With Polarization-Sensitive Frequency-Selective Surface Structure," *IEEE Transactions on Antennas and Propagation*, vol. 68, pp. 7348–7357, Nov. 2020.

[94] D.-M. Sun, Z.-C. Hao, W.-Y. Liu, and C.-Y. Ding, "An Ultrawideband Dual-Polarized Phased Array Antenna for Sub-3–GHz 5G Applications With a High Polarization Isolation," *IEEE Transactions on Antennas and Propagation*, vol. 71, pp. 4055–4065, May 2023.

[95] M. Carvalho and J. L. Volakis, "Deployable Rigid-Flexible Tightly Coupled Dipole Array (RF-TCDA)," *IEEE Open Journal of Antennas and Propagation*, vol. 2, pp. 1184–1193, 2021.

[96] F. Liu, L. Zheng, Y. Cui, C. Masouros, A. P. Petropulu, H. Griffiths, and Y. C. Eldar, "Seventy Years of Radar and Communications: The road from separation to integration," *IEEE Signal Processing Magazine*, vol. 40, pp. 106–121, July 2023.

[97] J. T. Logan, W. M. Dorsey, and J. A. Valenzi, "Modular All-Metal Ultrawideband Cylindrical Array for Multifunction Operation," *IEEE Transactions on Antennas and Propagation*, vol. 70, pp. 9175–9183, Oct. 2022.

[98] Z. Zhang, W. Zhang, S. Zeadally, Y. Wang, and Y. Liu, "Cognitive radio spectrum sensing framework based on multi-agent arc hitecture for 5G networks," *IEEE Wireless Communications*, vol. 22, pp. 34–39, Dec. 2015.